Atmospheric and Ocean Dynamics of Water Worlds

Thesis by
Ana H. Lobo

In Partial Fulfillment of the Requirements for the
Degree of
Doctor of Philosophy

CALIFORNIA INSTITUTE OF TECHNOLOGY
Pasadena, California

2022
Defended July 16, 2021

Ana H. Lobo
ORCID: 0000-0003-3862-1817

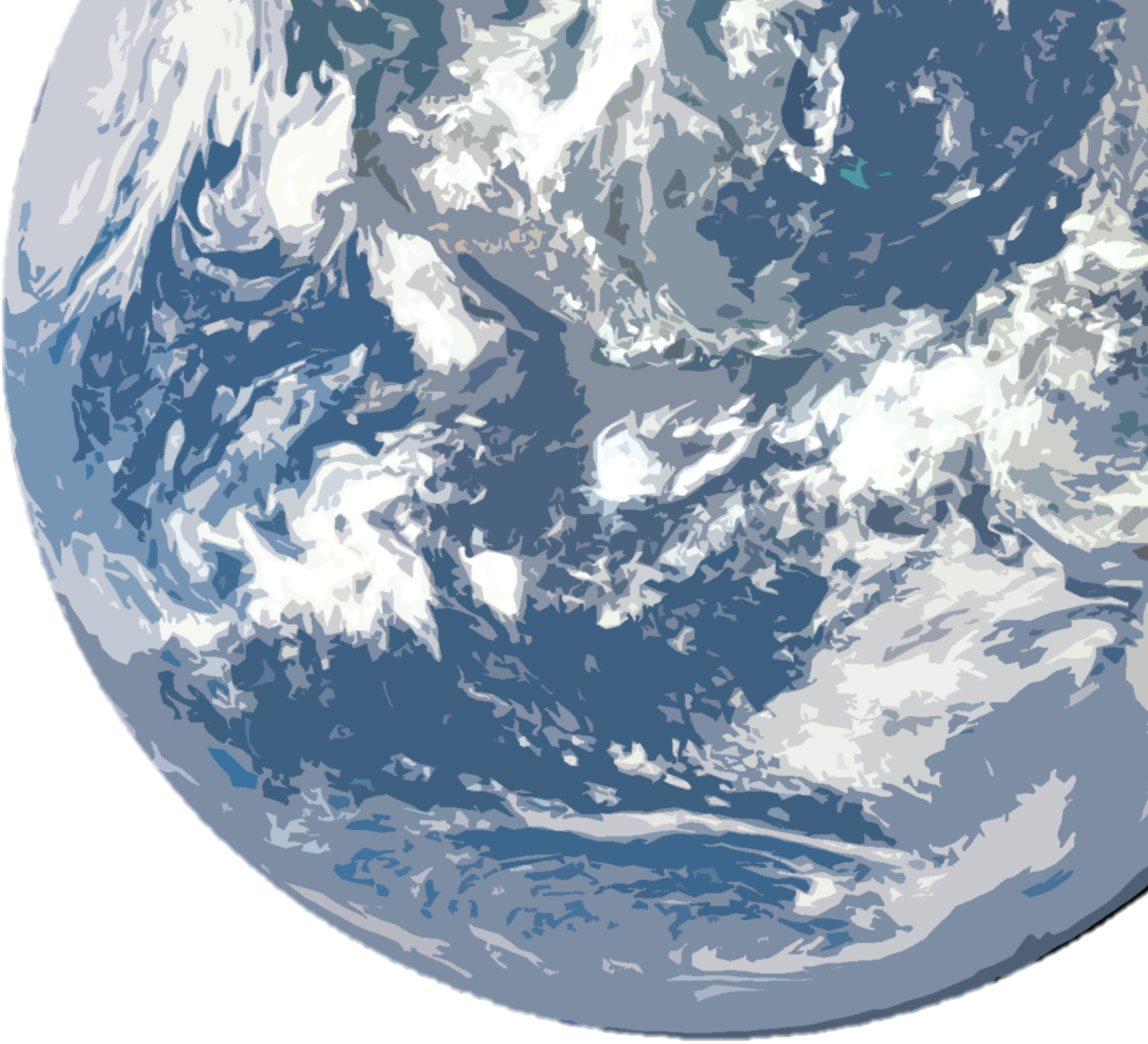

Atmospheric and Ocean Dynamics of Water Worlds

ABSTRACT

This dissertation explores the fundamental dynamics that control atmospheric and ocean circulation on water worlds. These planets are defined by the presence of liquid water, which is a minimum requirement for life as we know it, making them compelling targets in the search for extraterrestrial life. This work begins by examining the atmospheric features and surface climates of Earth-like planets with surface liquid water (Chapters I-III). These atmospheres are driven by top-of-atmosphere radiative imbalance. To further our understanding of planetary climate and of the atmosphere's dynamical controls, particularly with regards to seasonal behavior, we examine the circulation, energy budget, and hydrological cycle responses to changes in shortwave and longwave radiative forcings.

Changes in planetary obliquity result in a redistribution of shortwave radiation, such that high obliquity planets receive significantly more energy at the poles. This work shows that increased obliquity results in stronger and broader seasonally reversing cross-equatorial Hadley cells. Embedded in the ascending branches of these cells is a wider and poleward-shifted ITCZ, which does not coincide with maxima in near-surface temperature and remains dynamically constrained to the midlatitudes (Chapter II). Significant polar precipitation can occur due to an increase in polar atmospheric moisture storage and rapid cooling at the end of summer. The planetary energy budget shows that on planets with a low surface heat capacity, increased polar latent heat release can compensate for radiative cooling in early winter (Chapter III). The conversion of latent to sensible heat weakens meridional temperature gradients, hindering the formation of baroclinic eddies, the Ferrel cell, and storm tracks, effectively delaying the onset of polar winter. High obliquity simulations highlight these effects, but they also occur over a broad range of planetary configurations. Small variations in longwave optical depth can enhance these effects, resulting in significant changes in baroclinic eddy activity even at low obliquity.

This dissertation also explores icy worlds (Chapters IV-V), a type of water world where a liquid water ocean exists beneath a substantial icy shell. Within the solar system, icy worlds are redefining the way we perceive the habitable zone. These ice-covered oceans, formed beyond the ice line, can house liquid water reservoirs larger than Earth's and provide many of the necessary ingredients for life. In this work, we build on the residual circulation theory for Earth's Southern Ocean circulation (Chapter IV) to develop a novel understanding of the ocean circulation on icy worlds. Focusing on Enceladus (Chapter V), the best characterized and potentially most accessible ocean in the solar system, we show that density forcings at the ocean-ice interface can help support a stratified ocean with an overturning circulation. Spatially separated regions of ice formation and melt can induce a horizontal stratification and a freshwater lens in the polar regions, suggesting that measurements from Enceladus' plumes may underestimate the global ocean's salinity. Assuming the ice shell is in steady state, we can relate the meridional ice thickness gradients to a buoyancy flux. Thus, as ice shell measurements improve, this model would allow us to obtain further insight into the ocean circulation, nutrient distribution, and heat transport within the ocean.

PUBLISHED CONTENT

This thesis contains results that were previously published in:

A. H. Lobo, A. F. Thompson, S. D. Vance, and S. Tharimena. A pole-to-equator ocean overturning circulation on Enceladus. *Nature Geoscience*, 14:185–189, 2021. doi: 10.1038/s41561-021-00706-3.

A. H. Lobo and S. Bordoni. Atmospheric dynamics in high obliquity planets. *Icarus*, 2020. doi: 10.1016/j.icarus.2019.113592.

A.H.L participated in all aspects of the work listed above, including conception, execution, and writing of the manuscripts.

TABLE OF CONTENTS

INTRODUCTION

This thesis explores the dynamic and thermodynamic controls that shape the global atmospheric and ocean circulations on Earth and on other water worlds. This work seeks to leverage the existing understanding of Earth's climate system and terrestrial climate modeling tools to advance our understanding of fundamental planetary climate properties, while also using planetary case studies to explore aspects of Earth's atmospheric circulation that remain poorly understood. The planetary scenarios included here focus on water worlds because life, as we know it, has three key requirements: liquid water, an energy source, and the right chemical building blocks to form organic molecules. Of these requirements, water may be the easiest to search for and is likely to be the first observable indication a planet could be habitable. Water worlds, which are defined by the presence of water, are therefore a broad grouping of the most compelling targets in the search for extraterrestrial life, both within and beyond the solar system.

What are Water Worlds?

As a category, water worlds encompass a wide range of planet types, from Earth-like exoplanets to icy worlds. The nomenclature for these planet types is still evolving and many of the more commonly used terms have imprecise definitions. For the sake of clarity, the following definitions will be used here:

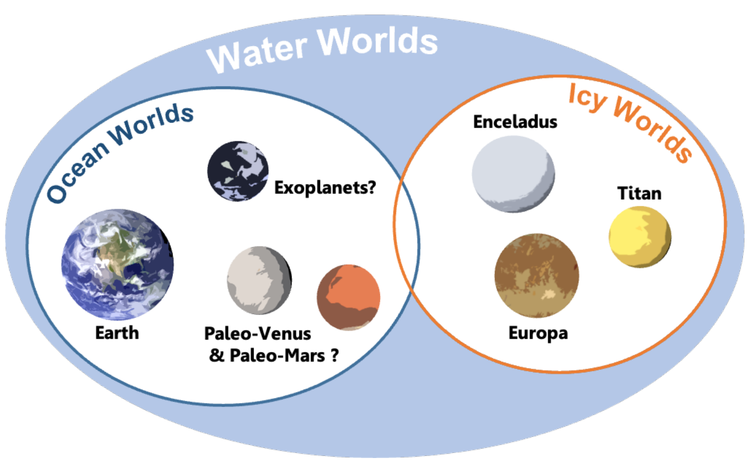

i. Any planet with abundant water (H_2O in any form) is considered a *water world.*

ii. *Icy worlds* are water worlds with global-scale oceans entirely encased by ice shells. These bodies are common in the outer reaches of the solar system.

iii. Rocky planets with global-scale surface liquid water will be referred to as *ocean worlds*.

iv. Rocky planets with significant atmospheric water vapor, but with limited surface water, will be described as *land planets*. The latter could potentially have liquid water in the form of regional oceans, lakes, and soil moisture.

Earth is often referred to as an ocean world, which is reasonable given that oceans cover the majority of the planetary surface. But the significant influence of continents and their topography on the surface climate should serve as a reminder that intermediate (or mixed) regimes are entirely possible. In other words, these classifications should be thought of as labels on scale, and not rigid classification bins.

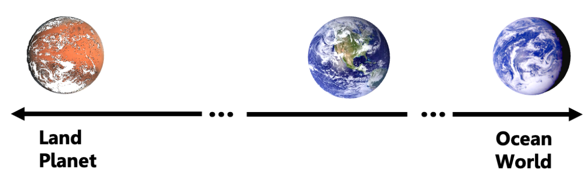

Each type of water world presents exciting prospects in terms of habitability, as well as unique observational challenges. For example, icy worlds are abundant within our solar system and offer the possibility of habitable worlds that we could visit and explore in detail in the coming decades. However, reaching these oceans, encased in tens of kilometers of ice, will be a challenge. Orbiter missions (e.g. JUICE, Europa Clipper) and future landers (e.g. Dragonfly) will help us better constrain ocean properties, and hopefully, technological advancements in the coming years will make it possible to plan robotic missions that reach beneath the ice shells. For exoplanet observational studies, ocean worlds and land planets are more appealing targets than icy worlds because they offer a greater likelihood of detectable habitability, with potentially observable liquid water, water vapor, and perhaps even observable biosignatures. While Earth-sized planets in their star's habitable zones are still difficult to detect, the upcoming James Webb Space Telescope and possible future missions such as LUVOIR and HabEx, will expand our ability to explore these water worlds.

Ocean worlds are often discussed exclusively in terms of exoplanet studies because Earth is the only ocean world within the solar system. However, it is possible that other solar system ocean worlds may have existed in the past. Venus, Mars, and Earth share a similar early history, having formed in roughly the same protoplanetary neighborhood, from roughly the same "building blocks". All three are believed to have received abundant water from impacts, possibly as a result of asteroids being displaced by Jupiter's migration (Gomes et al., 2005), and may have sustained surface oceans during earlier eras (Way et al., 2016). For Mars in particular, there is strong geological evidence of abundant liquid surface water in the form of dendritic valley networks in the low latitudes (Hynek et al., 2010; Carr, 1995). The climate characteristics of these early water worlds are still poorly constrained. But the comparison of Earth's climate trajectory with that of its now inhospitable neighbors highlights the fragility of planetary climate and the importance of better understanding the key mechanisms that control planetary climate properties and evolution.

The thesis chapters are structured according to the following two themes:

i. Learning about Earth as a Water World

Water worlds serve as a test bed to expand our understanding of atmospheric and ocean circulations, and serve as a means to validate fundamental theories under a wider range of conditions. They also provide a broader context for understanding Earth, its climate history, and its habitability.

Earth's atmospheric circulation is driven by top-of-atmosphere radiative imbalances. Local energy surpluses are balanced by atmospheric and oceanic transport towards regions of energy deficit, with local energy storage in the atmosphere and surface playing a role on shorter timescales through changes in temperature and water vapor content. The balance between energy transport and energy storage impacts how the surface climate responds to the seasonal insolation cycle, directly affecting the intensity of seasonal temperature fluctuations, the timing of seasonal transitions, and the distribution of precipitation (Neelin, 2007; Donohoe et al., 2014; Lobo and Bordoni, 2020). Determining the controls on the climate system's ability to redistribute energy is essential to understanding seasonal climate.

Disentangling competing boundary layer, dynamic and thermodynamic controls on Earth's atmospheric circulation, and its energy transport, has been a pervasive challenge over the past few decades. But simulations of Earth-like planets offer an opportunity to do just that. For example, examining the atmospheric seasonal response to increased obliquity shows that the intertropical convergence zone (ITCZ) location and the associated peak in precipitation do not always coincide with maxima in near-surface temperature and instead remain dynamically constrained to the midlatitudes even when the insolation maxima shifts to the pole (Chapter II). Meanwhile, a study of extratropical behavior (Chapter III) shows that atmospheric moisture, both through storage effects and latent heat release upon condensation, can indirectly delay or even prevent baroclinic eddy activity, hindering the formation of storm tracks and the winter Ferrel cell.

ii. Are there Habitable Oceans in the Solar System?

Ice-covered oceans in planetary bodies within the solar system can house liquid water reservoirs larger than Earth's and provide many of the necessary ingredients for life. However, we still have a limited understanding of the oceans' composition and dynamical properties. These oceans are, at first glance, almost entirely unlike Earth's. Earth's oceans cover the majority of the planet's surface and are warmed from above by solar radiation. They also interact with the atmosphere, such that their currents are partially driven by wind, as well as buoyancy forcings resulting from heat exchanges with the atmosphere, precipitation, evaporation, and ice formation processes. Meanwhile, icy worlds such as Enceladus, have global oceans that are predicted to be much deeper (Beuthe et al., 2016) and entirely encased by an ice shell. Enceladus's ocean is believed to be warmed predominantly by tidal heating (Choblet et al., 2017) and cooled at the ocean-ice interface. However, icy world oceans share a key aspect with Earth's oceans, which is their substantial salinity.

Variations in salinity can drive the ocean circulation on icy worlds, much as they do in Earth's Southern Ocean (Abernathey et al., 2016). This form of surface buoyancy forcing may be particularly relevant for Enceladus, Saturn's small bright moon known for its plumes, which vent water in the south polar region. Gravitational measurements and heat calculations from Cassini indicate that Enceladus' ice shell is thinner at the poles than at the equator. To sustain the ice shell thickness gradients at steady state, regions of thicker ice would be regions of ice formation. As salty water freezes, it releases salts, making the surrounding water less buoyant. Conversely, in regions where the ice is thinner, melting is expected to occur, resulting in the release of low salinity water that increases the buoyancy of the surrounding ocean. Thus, the pole-to-equator ice shell thickness gradient on Enceladus would suggest the presence of a strong surface buoyancy forcing that could drive meridional ocean currents (Lobo et al., 2021). While this thesis focuses on the role of buoyancy forcings, it is worth noting that the mean ocean salinity can also impact the circulation (Zeng and Jansen, 2021).

This thesis describes a new model developed to explore the ocean stratification and circulation of icy worlds (Chapter IV). The model is inspired by the residual circulation framework used in studies of Antarctica, and illustrates how we can use our knowledge of the ice shell to place constraints on circulation patterns, which influence the distribution of heat and nutrients. By linking ice shell properties to the ocean circulation, this study provided a new mechanism for investigating ocean structure with data from upcoming orbiter missions. With this model, we explore the ocean stratification on Enceladus (Chapter V) to show that lower density layers can exist in the poles, indicating that the polar plume measurements from *Cassini* are unlikely to be representative of global ocean tracer characteristics, and specifically underestimating ocean salinity.

References

R. P. Abernathey, I. Cerovecki, P. R. Holland, E. Newsom, M. Mazloff, and L. D. Talley. Water-mass transformation by sea ice in the upper branch of the southern ocean overturning. *Nature Geoscience*, 9:596–601, 2016. ISSN 1752-0908. doi:10.1038/ngeo2749.

M. Beuthe, A. Rivoldini, and A. Trinh. Enceladus's and Dione's floating ice shells supported by minimum stress isostasy. *Geophysical Research Letters*, 43(19):10,088–10,096, 2016. doi:10.1002/2016GL070650.

M. H. Carr. Martian drainage system and the origin of valley networks and fretted channels. *Journal of Geophysical Research*, 1995. ISSN 01480227. doi:10.1029/95JE00260.

G. Choblet, G. Tobie, C. Sotin, M. Běhounková, O. Čadek, F. Postberg, and O. Souček. Powering prolonged hydrothermal activity inside Enceladus. *Nature Astronomy*, pages 841–847, 2017. ISSN 2397-3366. doi:10.1038/s41550-017-0289-8.

A. Donohoe, D. M. Frierson, and D. S. Battisti. The effect of ocean mixed layer depth on climate in slab ocean aquaplanet experiments. *Climate Dynamics*, 43(3-4):1041–1055, 2014. ISSN 14320894. doi:10.1007/s00382-013-1843-4.

R. Gomes, H. F. Levison, K. Tsiganis, and A. Morbidelli. Origin of the cataclysmic late heavy bombardment period of the terrestrial planets. *Nature*, 435:466–469, 2005. ISSN 1476-4687. doi:10.1038/nature03676.

B. M. Hynek, M. Beach, and M. R. T. Hoke. Updated global map of Martian valley networks and implications for climate and hydrologic processes. *Journal of Geophysical Research*, 2010. ISSN 0148-0227. doi:10.1029/2009je003548.

A. H. Lobo and S. Bordoni. Atmospheric dynamics in high obliquity planets. *Icarus*, 340:113592, 2020. ISSN 10902643. doi:10.1016/j.icarus.2019.113592.

A. H. Lobo, A. F. Thompson, S. D. Vance, and S. Tharimena. A pole-to-equator ocean overturning circulation on enceladus. *Nature Geoscience*, 14: 185–189, 2021. ISSN 1752-0908. doi:10.1038/s41561-021-00706-3.

J. D. Neelin. Moist dynamics of tropical convection zones in monsoons, teleconnections and global warming. In T. Schneider; A. H. Sobel., editor, *The Global Circulation of the Atmosphere*, pages 267–301. Princeton University Press, 2007.

M. J. Way, A. D. D. Genio, N. Y. Kiang, L. E. Sohl, D. H. Grinspoon, I. Aleinov, M. Kelley, and T. Clune. Was Venus the first habitable world of our solar system? *Geophysical Research Letters*, 43:8376–8383, 8 2016. ISSN 19448007. doi:10.1002/2016GL069790.

Y. Zeng and M. F. Jansen. Ocean circulation on enceladus with a high versus low salinity ocean. *arXiv*, 2021. URL `http://arxiv.org/abs/2101.10530`.

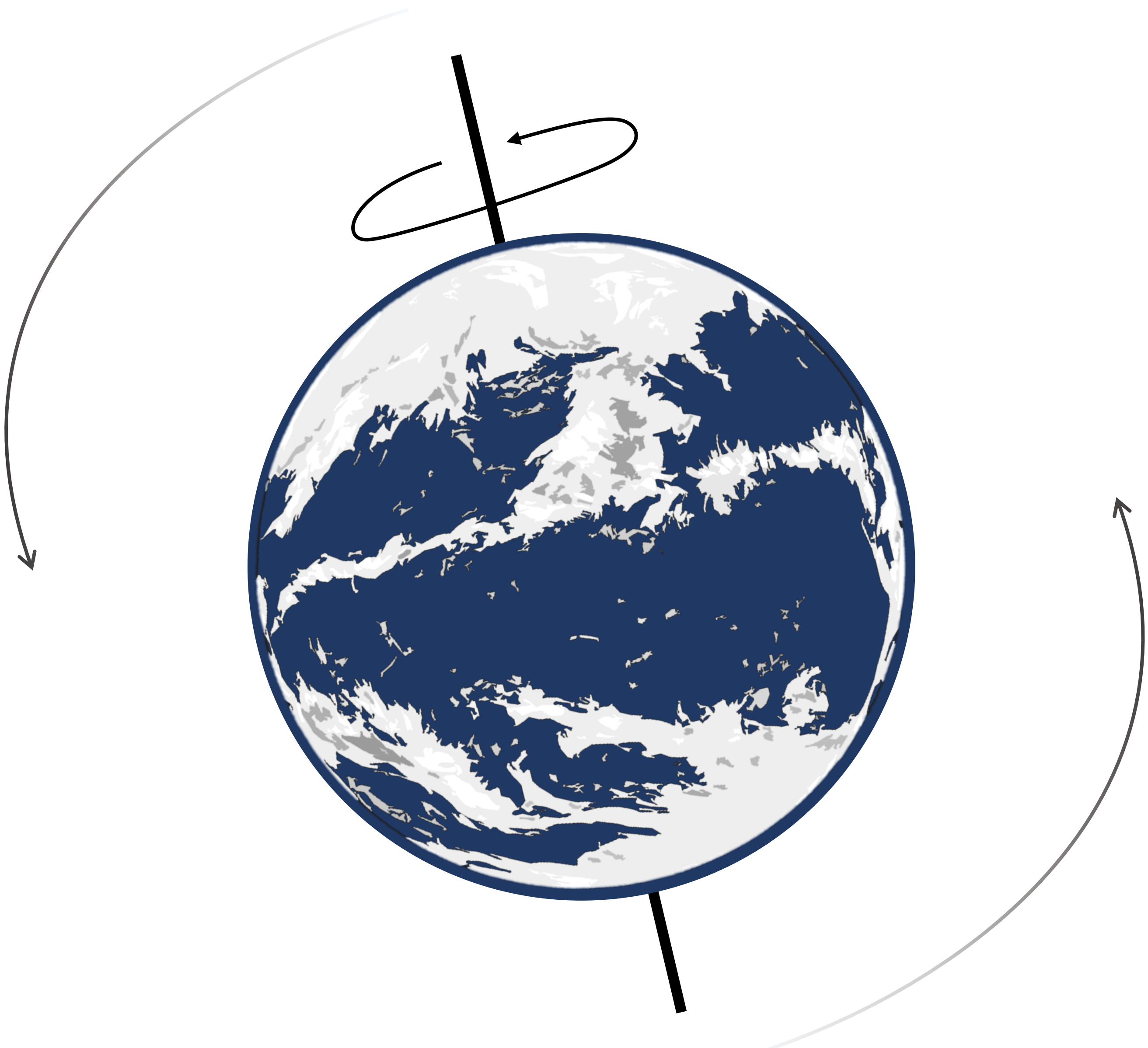

Chapter 1

SEASONAL CLIMATE OF HIGH OBLIQUITY PLANETS

The recent surge in exoplanet discoveries and the promise of improved detection limits in the near future have inspired a new wave of research in planetary climate. It is now necessary to consider a much larger range of possible orbital parameters, and surface and atmospheric conditions than what was previously seen in studies of our solar system's rocky planets. Yet, this must be done while working with a drastically smaller dataset for each planet. Models of different complexity have hence provided a fundamental tool to further our understanding of atmospheric behavior of these planets under a wide range of physical and dynamical regimes. These include studies such as Del Genio and Zhou (1996), Merlis and Schneider (2010), Faulk et al. (2017), and many others summarized in the review paper by Showman et al. (2013). Idealized models have proven particularly useful because they allow for investigations of the fundamental mechanisms controlling climate without requiring specific knowledge about the atmospheric composition and chemistry.

Earth is, of course, the most extensively studied terrestrial planet and we would benefit from extrapolating what we know about our planet to those newly discovered. However, we still struggle to disentangle the impact of dynamical, thermodynamic, and boundary layer processes on Earth's large-scale atmospheric circulation. For example, predicting how the Hadley cell responds, in terms of its strength and extent, to changes in radiative forcing and planetary parameters is still an active area of research, despite being a first order problem for characterizing the large-scale circulation of an Earth-like planet (e.g. Faulk et al., 2017; Singh, 2019; Guendelman and Kaspi, 2018). Hence, we are faced with the opportunity and the need to advance two fields concurrently. By testing competing atmospheric theories over a broader range of parameters we can both improve our understanding of the processes we encounter on Earth and better characterize different atmospheric regimes we might encounter in terrestrial planets. This is the approach taken by many of the previously mentioned papers over a broad range of parameters. Our goal is to expand on the existing body of literature through an in-depth study of the atmospheric response to varying obliquity. We focus on the seasonal response of atmospheric large-scale circulations and their relationship to the hydrological cycle.

While many have explored the atmospheric circulation and associated climate arising in response to annual-mean solar forcing – a useful starting point – the removal of seasonal cycles prevents consideration of seasonal phenomena that are of primary importance for a planet's climate and whose dynamics remain relatively poorly understood. These seasonal phenomena include the monsoons on Earth (Schneider and Bordoni, 2008), polar clouds on Titan (Turtle et al., 2009), and dust storms on Mars (Wang and Richardson, 2015). Depending on the planet's orbital parameters, seasonal cycles could be even more extreme than those we currently see on the "Earth-like" terrestrial planets in our solar system, potentially introducing nonlinearities not captured under annual-mean forcing.

In the context of seasonal cycles, exploring the impact of obliquity takes a primary relevance. As obliquity increases beyond 54°, a planet receives more energy at the poles than at the equator on the annual average, opposite to what is seen on planets with smaller obliquities, such as Earth. Also, high obliquity planets have extreme seasonal cycles, which raises the question of how the atmospheric circulation might mitigate these variations and to what extent it could render such planets habitable. Thus, understanding how obliquity influences the climate of a planet is not only a useful theoretical exercise, but is also relevant to ongoing efforts to understand Martian paleoclimate and better characterize the climate of other planets in our own solar system.

To address these questions, we conduct experiments with an idealized atmospheric general circulation model in aquaplanet configuration to explore how obliquity affects the climate of an Earth-like planet. Obliquity is varied over a broad range of values, namely from 10° to 85°. The model makes use of a slab ocean, rather than a fully interactive ocean, which does not allow for consideration of the role of ocean dynamics in the simulated climate. There is no doubt that an ocean would have a significant impact on climates of high obliquity planets, if one existed. The ocean heat uptake, through seasonal storage and transport by oceanic currents, would prevent more extreme seasonal temperature changes, serving as a heat source during winter and sink during summer (Ferreira et al., 2014). In its absence, it is left to atmospheric motions to possibly mitigate imbalances implied by the solar insolation. We are interested in exploring these atmospheric features and their dynamics in these extreme climates.

1.1 Aquaplanet Model

We utilize a 3D idealized primitive equation General Circulation Model (GCM) of an ideal-gas atmosphere, built on the Flexible Modeling System (FMS) developed by the Geophysical Fluid Dynamics Laboratory (GFDL) (Frierson et al., 2007; O'Gorman and Schneider, 2008). It is idealized in terms of the represented physics and in terms of the lower boundary, which is a completely uniform slab ocean of constant depth (aquaplanet).

The GCM is a moist model, in that it contains idealized representation of the effect of latent heat release of condensing water vapor on the dynamics through a grid-scale condensation scheme and a quasi-equilibrium convection scheme (Frierson et al., 2007; O'Gorman and Schneider, 2008). The set-up is similar to that in Bordoni and Schneider (2008), with T42 horizontal resolution and 30 levels in the vertical. While somewhat coarse, the horizontal resolution is more than adequate to resolve the large-scale circulation features, such as the Hadley cell and baroclinic eddies, we are interested in. Radiation is represented through a two-stream gray radiation scheme with prescribed longwave optical depth. In this study, the optical depth (τ) is only a function of pressure, comprising a well mixed CO_2-like absorber and a bottom-heavy "water vapor" absorber:

$$\tau(p) = \tau_o \left[f \left(\frac{p}{p_0} \right) + (1 - f) \left(\frac{p}{p_0} \right)^4 \right] \tag{1.1}$$

where $\tau_o = 4.57$ and $f = 0.2$. Note that keeping τ fixed and independent of water vapor concentration precludes any water vapor feedback. We also run a variant of the control set-up, in which τ depends on the local water vapor concentration (thus providing a simple representation of the water vapor feedback, Merlis and Schneider, 2010). These will hereby be referred to as the $\tau_{control}$ and τ_{wv} experiments.

We run the model in aquaplanet configuration, where the lower boundary is entirely covered with water (a slab ocean with constant depth). The sea surface temperature evolves according to a surface energy budget, which includes radiative fluxes and turbulent surface fluxes of latent and sensible heat. We only conduct experiments with a mixed layer depth of 1 m, which is equivalent to a surface heat capacity of $C_s = 4.13 \times 10^6$ J/m^2/K. Following Cronin and Emanuel (2013), a simple thermal inertia timescale for this lower boundary can be computed as $\tau = C/\lambda$, where λ is a feedback parameter given by a linearized coefficient of combined sensible, latent, and longwave heat flux (c.f. Barsugli and Battisti, 1998). For $\lambda = 40$ W m^{-2} K^{-1}, as typical for the tropics (Gill, 1982), a 1 m ocean mixed layer depth has a thermal inertia timescale of $\sim$1 day. While the shallow mixed layer depth used here is not representative of ocean-covered surfaces on Earth (with typical ocean mixed layer depths of 50 m, which would imply an inertial timescale of 2 months) and results in more extreme seasonal variations than what is seen in the annual mean (e.g., Bordoni and Schneider, 2008; Merlis et al., 2013; Faulk et al., 2017), it helps exaggerate the response of the seasonal cycle to obliquity changes and, hence, isolate mechanisms behind these changes.

Parameter	**Control Value**
Radius	6371 km
Rotation Rate	7.292x10^{-5} s^{-1}
Gravity	9.80 m/s^2
Eccentricity	0
Solar Constant	1360 W/m^2
Mixed Layer Depth	1 m
Specific Heat Capacity of Lower Boundary	$\sim$ 3989.245 J/kg/K
τ_o for $\tau_{control}$	4.57
τ_o for τ_{wv}	1.39
Ref. Moisture Profile	70%
Convective Relaxation Time Scale	7200.0 s
Latent Heat of Vaporization (L_v)	2.5x10^6 J/kg
Specific Heat Capacity (c_p) of Air at Constant Pressure	1004.64 J/kg/K

Table 1.1: Summary of key model parameters used in all simulations.

The model is forced with a seasonal cycle of insolation of 360 days, with all other orbital parameters kept at Earth's values (see Table 1.1) and obliquity varied systematically with values of 10, 23.5, 40, 54, 70, and 85°. All simulations are spun up from an isothermal state at rest and run for 20 years. Results are averaged over the last 15 simulated years. All statistics (including eddy fluxes) are computed from 6-hourly outputs and averaged at pentad (5 day) temporal resolution. While parameters of interest for all simulations are shown in selected figures, most of the following discussion will provide an in-depth comparison between the Earth-like 23.5° and the 85° obliquity end case.

1.2 Surface Climate

Changes in obliquity result in a spatial and seasonal redistribution of short-wave radiation reaching the surface: while the globally and annually averaged energy remains the same, as obliquity increases, the higher latitudes receive more insolation both during the summer solstice seasons and in the annual mean (Fig. 1.1). For Earth's obliquity (23.5°), the insolation is maximum at the equator (335 W/m^2) and decreases to 42% of this value at the poles (140 W/m^2). As obliquity is increased, the pole-to-equator insolation gradient is progressively reduced, is almost flat at 54°, and reverses for higher obliquity values. For the highest obliquity we consider here, on the annual average, the equator receives 226 W/m^2, which is about 63% of the values at the poles.

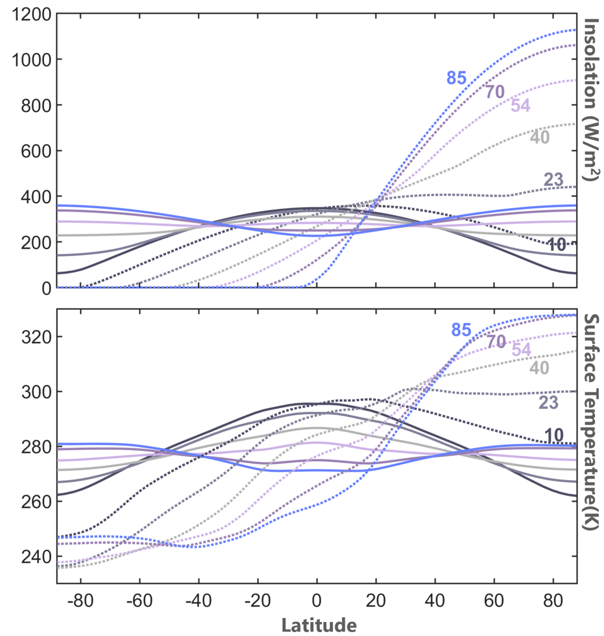

Figure 1.1: Meridional distribution of zonally averaged insolation (W/m^2, top) and near-surface (lowest model level) temperature (K, bottom) for $\tau_{control}$ simulations with all obliquity values. Solid lines represent annual-mean values, and dashed lines represent NH summer solstice values (at pentad 18).

Over the seasonal cycle, obliquities equal to or larger than 23.5° show insolation distributions with similar behavior (Fig. 1.2), with the summer poles being the loci of maximum insolation at solstice. The insolation contrast between the summer and winter hemispheres, however, sharply increases with increasing obliquity. For the highest obliquity value considered in this study (85°), at summer solstice the summer pole receives upwards of 1000 W/m^2 and more than twice as much as the Earth-like case of 23.5°. Meanwhile, the polar night in the winter hemisphere for 85° obliquity encases the entire hemisphere and leaves even the low latitudes of the summer hemisphere in relative darkness (with the equator receiving as little as 23 W/m^2) .

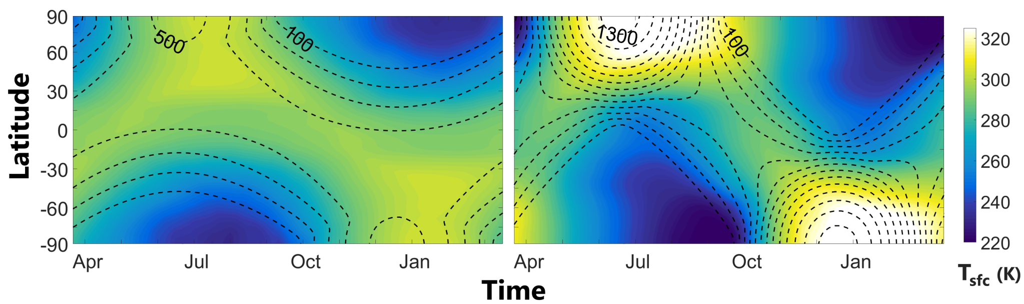

Figure 1.2: Near-surface temperatures (color contours, K) and shortwave incoming radiation (dotted lines, W/m^2) vs time for 23.5° (left) and 85° (right) obliquity with $\tau_{control}$. Radiation contours have intervals of 100 W/m^2, with the highest and lowest contours labeled.

Not surprisingly, these insolation changes with obliquity imprint on the spatial and temporal distribution of near-surface temperatures (Fig. 1.1, bottom): in the annual mean, temperatures at the equator decrease monotonically with obliquity from 295 K at 23.5° to 274 K at 85°, while polar temperatures increase from 268 K at 23.5° to 281 K at 85°. At summer solstices (Fig. 1.1, bottom), the summer pole becomes increasingly warmer, reaching 326 K at 85°, over 20 K warmer than the corresponding temperature at 23.5°.

The entire evolution of insolation and near-surface temperatures throughout the year is shown in Fig. 1.2. Note how despite the very small thermal inertia of the lower boundary, near-surface temperatures lag insolation by about one month because of atmospheric thermal and dynamical inertia (e.g., Wei and Bordoni, 2018).

1.3 Atmospheric Meridional Energy Transport

While the results in the previous section are not surprising, there are aspects of the temperature distribution that are less obvious. In particular, the changes in near-surface temperature gradient between the winter and summer hemispheres as obliquity increases are much smaller than might be expected in radiative equilibrium given the dramatic insolation gradients at high obliquity. This suggests that atmospheric energy transport plays a fundamental role in redistributing energy from regions of net energy input to regions of net energy deficit and in mitigating temperatures.

The meridional energy transport is given by:

$$< \overline{vh} >= \int_0^{P_s} \overline{vh}\, \frac{dp}{g} \tag{1.2}$$

where v represents the meridional flow, and h represents the moist static energy (MSE) defined as $h = c_pT + gz + L_vq$, which is comprised of dry enthalpy (c_pT, with isobaric specific heat c_p), potential energy (gz, with gravitational constant g), and latent energy (L_vq, with latent heat of vaporization L_v and specific humidity q). The bar represents a time and zonal mean. The total meridional energy transport can be further decomposed as

$$< \overline{vh} >=< \overline{v}\overline{h} > + < \overline{v'h'} > \tag{1.3}$$

with the first term on the right hand side representing the transport by the zonal mean circulation and the second term representing the contribution by large-scale eddies, which in an aquaplanet are exclusively transient eddies. These components are shown in Fig. 1.3 for both the annual mean (top) and the northern hemisphere (NH) summer solstice (bottom) for 23.5° and 85° obliquities.

The annual-mean energy transport in the 23.5° case shows features consistent with Earth's energy transport, including poleward energy transport in both hemispheres and maximum values of 2.9 PW around 30° N and S. Transport by the Hadley cell dominates in the tropics, and transport by transient eddies peaks in the extratropics, more than canceling the equatorward transport by the indirect Ferrel cells. At 85°, total energy transport is still poleward in both hemispheres, despite the reversed gradient in imposed insolation, but much weaker than in the low obliquity case, with maxima of about 1.3 PW. This transport is dominated at all latitudes by the mean transport, with eddy transport being weaker and equatorward. That the transport is poleward (that is, up the insolation gradient) in the high obliquity case suggests the existence of a strong seasonality, which dominates the annual mean. It also emphasizes the importance of resolving seasonal cycles in these more extreme planetary regimes. This is a point we return to in Chapter II.

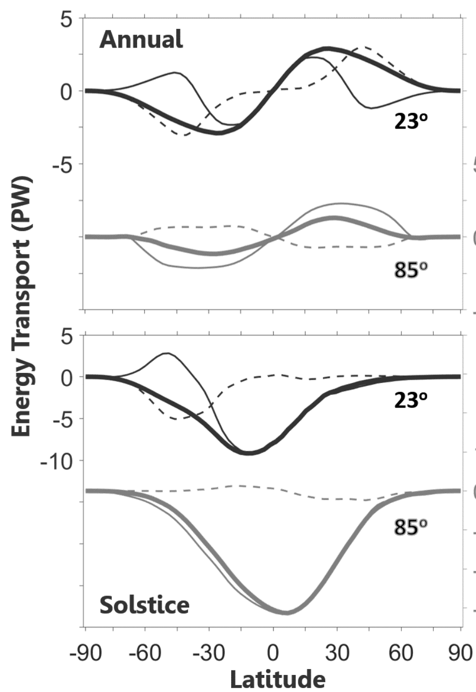

Figure 1.3: Vertically integrated MSE transport (PW) for 23.5° (black) and 85° (gray) obliquities and $\tau_{control}$. Top figure shows annual mean and bottom shows NH summer conditions. Dashed lines indicate eddy, solid mean, and bold total (eddy + mean) components.

At NH summer solstice, in the 23.5° case, the total energy transport is southward in both hemispheres, which indicates, as expected, transport from the summer (NH) into the winter (SH) hemisphere. Throughout the summer hemisphere and at lower latitudes in the winter hemisphere, the transport is dominated by the mean circulation. Eddy transport is significant only in the winter hemisphere extratropics, and it is in fact negligible in the summer hemisphere midlatitudes. At 85°, the solstice mean transport is much larger than in the lower obliquity case and entirely effected by the mean circulation. This is indicative of a solstice-mean Hadley circulation dominated by a strong cross-equatorial winter cell spanning a broad latitudinal range in both hemispheres (see ch. 2.1). Somewhat surprisingly, eddy transport at solstice is negligible even in the winter hemisphere. It is hence clear that the weak annual mean transport is the result of much stronger solstice transports, which switch sign with season and hence mostly cancel out.

In Fig. 1.4, the total, mean, and eddy transports are broken down into dry static energy ($c_pT + gz$) and latent energy (L_vq) components. For low obliquities, the dry static energy transport has the same sign as the MSE transport, because the atmosphere is stably stratified in a dry sense. The latent energy has oppositely signed transport (that is, northward in NH summer solstice), because moisture is primarily concentrated at lower levels and decreases rapidly with height. While the dry static and latent energy components largely cancel each other, the dry stratification wins out, giving rise to an overall southward transport.

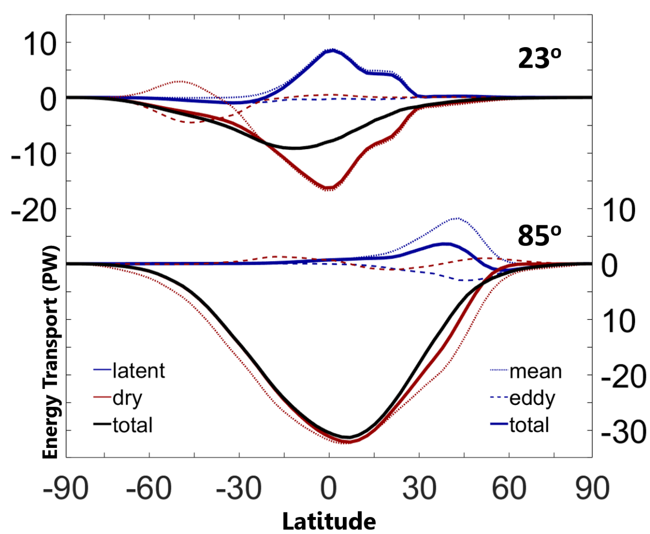

Figure 1.4: Vertically integrated MSE transport at NH summer solstice, broken down into dry component (gravitational + sensible) in red, and latent energy component in blue. Mean and eddy components are shown in dotted and dashed lines respectively, and totals are shown in bold.

Interestingly, in the high obliquity case, the transport is entirely dominated by the dry static energy component, with the latent energy being still opposite in sign but much smaller and nonnnegligible only in the ITCZ region. We find that at solstice, increasing obliquity consistently leads to a more dominant dry static energy transport for all cases, and a slight reduction of the latent energy transport. This can be seen in Fig. 1.5, where we show the vertically integrated cross-equatorial MSE transport at NH summer solstices (pentad 18) for all modeled obliquities. The decrease in latent heat transport occurs because the warmer and moister regions are progressively more and more confined to the summer pole as obliquity is increased, and contribute little to the overall transport.

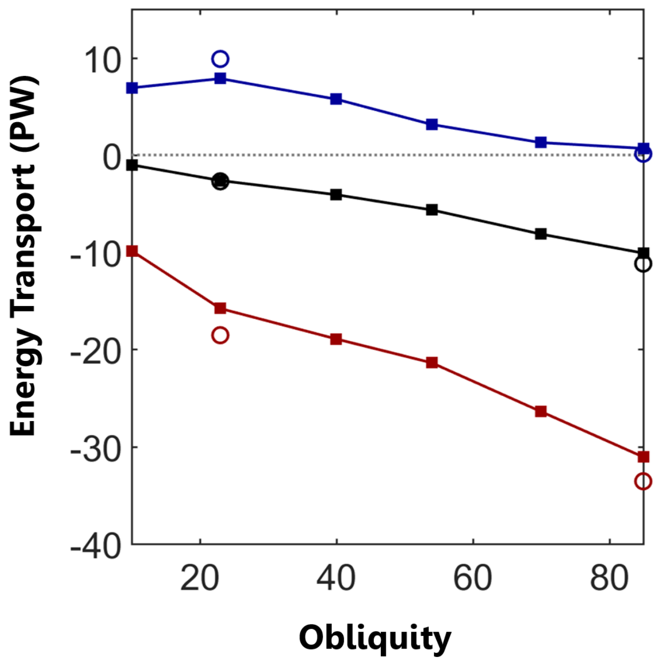

Figure 1.5: Cross-equatorial (average between 5°S and 5°N) MSE transport (black) at NH summer solstice, and its dry static energy (gravitational + sensible energy, red) and latent energy (blue) components for all obliquity values. $\tau_{control}$ and τ_{wv} results are shown with squares and open circles, respectively.

The latent energy transport distribution shown in Fig. 1.4 also gives some insight into the precipitation patterns. At 23.5° obliquity, we see moisture converging (a negative slope in the flux) both near the equator and near 25° latitude, which correspond well to the two main convergence zones that can be seen in the tropical region at this time of the year (Fig. 1.6). At high obliquity, however, convergence is primarily centered at around 40° from the equator. While the low obliquity case is dominated by the mean transport, at high obliquity we see a competition between the mean and eddy terms. The mean latent energy transport is northward, in the same direction as the low-level flow in the mean Hadley circulation, whereas the eddy transport is in the opposite direction, consistent with transport down the mean gradient, with maximum moisture values at the summer pole.

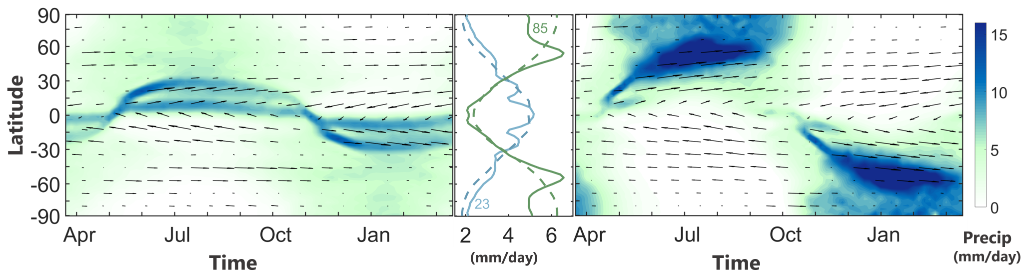

Figure 1.6: Precipitation (color contours, mm/day) and near-surface wind vectors vs time for 23.5° (left) and 85° (right) obliquity with $\tau_{control}$. The center panel shows annual mean values of precipitation (solid lines) and evaporation (dashed lines), also in mm/day.

The relationship between moisture transports, associated convergence, and precipitation is made more apparent in Fig. 1.6, which shows near-surface winds and precipitation at 23.5° and 85° obliquities. As obliquity increases, there are consistent patterns of precipitation changes: 1) the tropical precipitation distribution shifts from a double ITCZ structure, with a near-equatorial secondary peak and a subtropical primary peak, to a single ITCZ structure peaking at progressively higher latitudes; and 2) high latitude precipitation outside of the ITCZ also increases. Mechanisms behind these changes will be discussed in Chapter 2.

Another feature of interest in the precipitation patterns at all obliquities is the absence of a storm track, that is a band of enhanced precipitation in the winter hemisphere extratropics. This raises the question of to what extent this might be associated with the lack of eddy activity. To more quantitatively answer this question, in Fig. 1.7 we show the vertically integrated eddy kinetic energy (EKE) at NH summer solstice. We see that, as obliquity increases, EKE decreases because of decreased lower-level temperature gradients in the winter hemisphere. Also, though EKE is relatively large at Earth's obliquity, there is still no obvious precipitation storm track because of very low temperatures and, hence, very little available moisture. Notice how this is not representative of Earth's present-day climate because of the very shallow mixed layer depth, which allows for more extreme temperature variations than what is seen on Earth. We explore the patterns of eddy activity in more detail in Chapter 3.

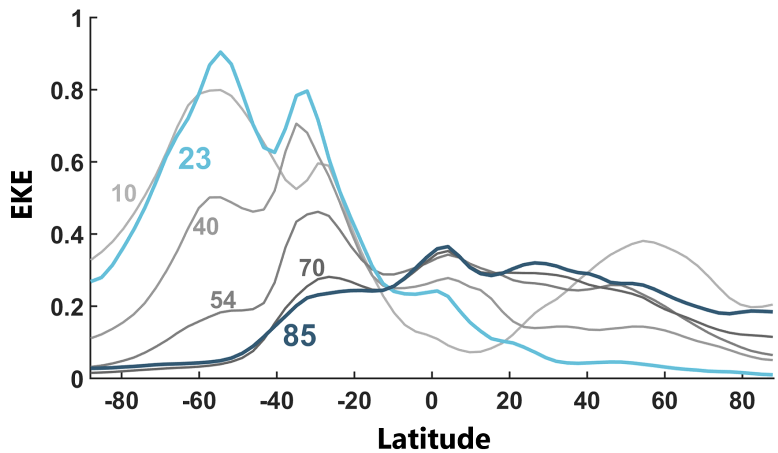

Figure 1.7: Vertically integrated eddy kinetic energy (up to $\sigma = 0.23$) in MJ/m^2 for all obliquities at NH summer solstice (pentad 18).

References

J. J. Barsugli and D. S. Battisti. The basic effects of atmosphere-ocean thermal coupling on midlatitude variability. *Journal of the Atmospheric Sciences*, 55(4):477–493, 1998. ISSN 00224928. doi:10.1175/1520-0469(1998)055<0477:TBEOAO>2.0.CO;2.

S. Bordoni and T. Schneider. Monsoons as eddy-mediated regime transitions of the tropical overturning circulation. *Nature Geoscience*, 1:515–519, 2008. ISSN 1752-0894. doi:10.1038/ngeo248.

T. W. Cronin and K. A. Emanuel. The climate time scale in the approach to radiative-convective equilibrium. *Journal of Advances in Modeling Earth Systems*, 5(4):843–849, 2013. doi:10.1002/jame.20049.

A. Del Genio and W. Zhou. Simulations of superrotation on slowly rotating planets: Sensitivity to rotation and initial condition. *Icarus*, 120(2):332–343, 1996. ISSN 00191035. doi:10.1006/icar.1996.0054.

S. Faulk, J. Mitchell, S. Bordoni, S. Faulk, J. Mitchell, and S. Bordoni. Effects of rotation rate and seasonal forcing on the ITCZ extent in planetary atmospheres. *Journal of the Atmospheric Sciences*, pages JAS–D–16–0014.1, 2017. ISSN 0022-4928. doi:10.1175/JAS-D-16-0014.1.

D. Ferreira, J. Marshall, P. A. O'Gorman, and S. Seager. Climate at high-obliquity. *Icarus*, 243:236–248, 2014. ISSN 10902643. doi:10.1016/j.icarus.2014.09.015.

D. M. W. Frierson, J. Lu, and G. Chen. Width of the Hadley cell in simple and comprehensive general circulation models. *Geophysical Research Letters*, 34 (18), 2007. ISSN 1944-8007. doi:10.1029/2007GL031115.

A. E. Gill. *Atmosphere-ocean dynamics*. Academic Press, New York, 1982. ISBN 9780122835223.

I. Guendelman and Y. Kaspi. An axisymmetric limit for the width of the hadley cell on planets with large obliquity and long seasonality. *Geophysical Research Letters*, 45(24):13,213–13,221, 2018. ISSN 19448007. doi:10.1029/2018GL080752.

T. M. Merlis and T. Schneider. Atmospheric dynamics of earth-like tidally locked aquaplanets. *Journal of Advances in Modeling Earth Systems*, 2(4): 1–17, 2010. ISSN 1942-2466. doi:10.3894/JAMES.2010.2.13.

T. M. Merlis, T. Schneider, S. Bordoni, and I. Eisenman. The tropical precipitation response to orbital precession. *Journal of Climate*, 26(6):2010–2021, 2013. ISSN 08948755. doi:10.1175/JCLI-D-12-00186.1.

P. A. O'Gorman and T. Schneider. The Hydrological Cycle over a Wide Range of Climates Simulated with an. *Journal of Climate*, 21:3815–3832, 2008. ISSN 0894-8755, 1520-0442. doi:10.1175/2007JCLI2065.1.

T. Schneider and S. Bordoni. Eddy-Mediated Regime Transitions in the Seasonal Cycle of a Hadley Circulation and Implications for Monsoon Dynamics. *Journal of the Atmospheric Sciences*, 65(3):915–934, mar 2008. ISSN 0022-4928. doi:10.1175/2007JAS2415.1.

A. P. Showman, R. D. Wordsworth, T. M. Merlis, and Y. Kaspi. Atmospheric Circulation of Terrestrial Exoplanets. In *Comparative Climatology of Terrestrial Planets*. University of Arizona Press, 2013. doi:10.2458/azu_uapress_9780816530595-ch12.

M. S. Singh. Limits on the extent of the solsticial Hadley cell: the role of planetary rotation. *Journal of the Atmospheric Sciences*, pages 1989–2004, 2019. ISSN 0022-4928. doi:10.1175/jas-d-18-0341.1.

E. P. Turtle, J. E. Perry, A. S. McEwen, A. D. DelGenio, J. Barbara, R. A. West, D. D. Dawson, and C. C. Porco. Cassini imaging of Titan's high-latitude lakes, clouds, and south-polar surface changes. *Geophysical Research Letters*, 36(2):n/a–n/a, jan 2009. ISSN 00948276. doi:10.1029/2008GL036186.

H. Wang and M. I. Richardson. The origin, evolution, and trajectory of large dust storms on Mars during Mars years 24–30 (1999–2011). *Icarus*, 251: 112–127, may 2015. ISSN 00191035. doi:10.1016/j.icarus.2013.10.033.

H.-h. Wei and S. Bordoni. Energetic constraints on the ITCZ in idealized simulations with a seasonal cycle. *Journal of Advances in Modeling Earth Sciences (JAMES)*, pages 1–35, 2018.

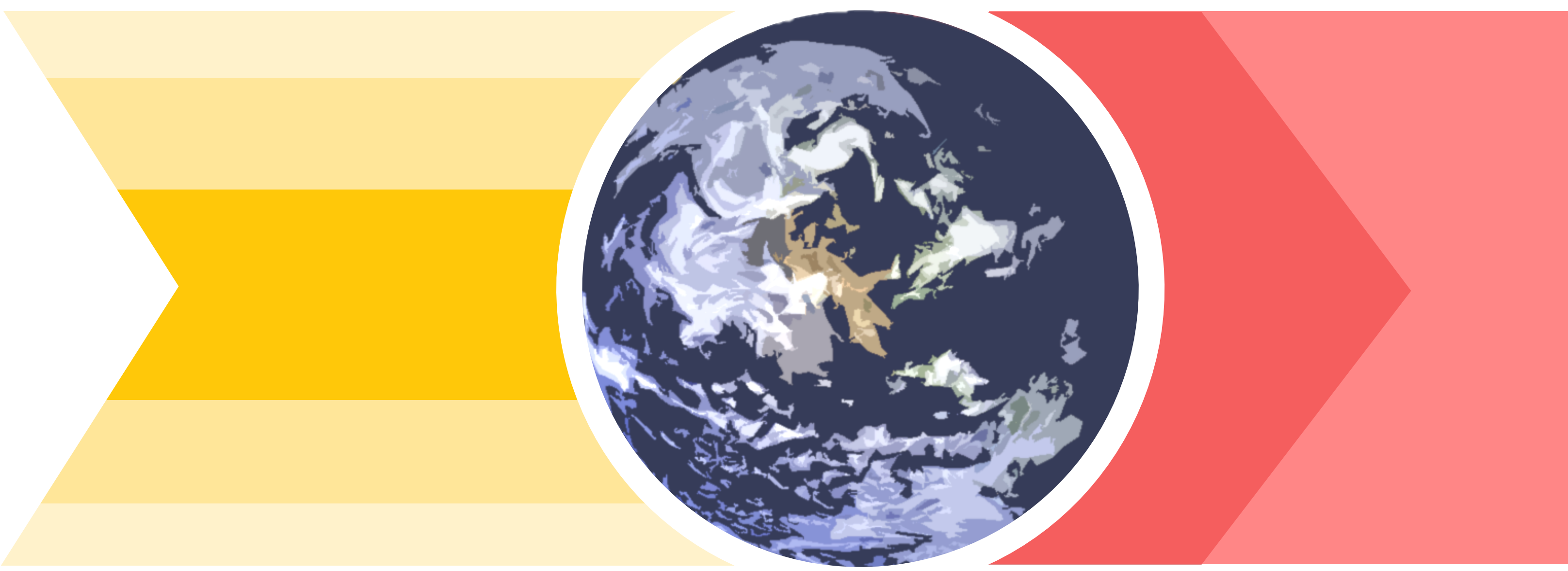

Chapter 2

TROPICAL DYNAMICS AND THE HYDROLOGICAL CYCLE

2.1 The Hadley Cell

The surface climate described in the previous chapter is strongly influenced by the large-scale circulation and associated moisture and energy transports. Thus, it is important that we more explicitly quantify the changes in the Hadley cell as obliquity is increased. Solstitial Hadley cells in aquaplanet simulations with shallow mixed layer depths, and their relevance to monsoonal cross-equatorial circulations in the Earth's atmosphere, have been previously discussed in the literature (e.g., Bordoni and Schneider, 2008; Merlis and Schneider, 2010; Faulk et al., 2017; Zhou and Xie, 2018). Similarly to those studies, we find that in the solstice seasons for Earth-like obliquity, the Hadley cell is dominated by a solstitial pattern, with a strong cross-equatorial winter Hadley cell and a negligible summer cell. This can be seen in Fig. 2.1, which shows the overturning circulation at NH summer solstice for 23.5 and 85° obliquity, together with the distribution of zonal winds and eddy momentum flux divergence. The small inertia of the shallow mixed layer depth makes it possible for the lower-level MSE to adjust rapidly on seasonal time scales, allowing the cell to intensify and expand rapidly into the summer hemisphere following the lower-level MSE maximum, which can move to around 30 degrees off the equator for Earth-like conditions (e.g., Privé and Plumb, 2007; Bordoni and Schneider, 2008).

As the circulation becomes cross equatorial and more strongly approaches conservation of angular momentum, upper-level easterlies develop over the tropics spanning almost the entire cell extent (Lindzen and Hou, 1988). Eddy momentum flux divergence is weak throughout the cell extent thanks to the shielding effect of the upper-level easterlies and, in fact, only affects the Hadley cell in its descending branch (e.g., Schneider and Bordoni, 2008; Bordoni and Schneider, 2008). Near the surface, westerlies develop in the summer hemisphere from around the equator up to the circulation's poleward boundary

(Fig. 1.6), as friction on the westerly flow balances the Coriolis force on the poleward meridional flow.

As obliquity is increased, and so are the latitude of the maximum solar forcing and the summer pole-to-equator temperature gradient, the cross-equatorial circulation broadens and intensifies, upper-level easterlies strengthen and prevail over an increasing portion of the cross-equatorial cell, and eddy momentum flux divergence is significant only in its descending branch. As the circulation becomes increasingly cross equatorial, its ascending branch broadens, consistent with the precipitation patterns shown in Fig. 1.6. It is however important to note how, while much broader than what is seen in the 23.5° case, the winter cross-equatorial cell in the 85° case is not truly global, with most of the circulation mass flux being confined within 60 degrees of the equator. As we discuss in the following section, energy and angular momentum constraints prevent the circulation from extending up to the latitude of maximum temperature and MSE (e.g., Hill et al., 2019; Guendelman and Kaspi, 2018), and the precipitation in the polar region is not associated with the ascending branch of the mean overturning circulation.

It is also worth noting how these overturning patterns confirm the overall lack of a significant Ferrel cell at solstice in the winter hemisphere. We see a weak winter Ferrel cell at 10° (not shown) and 23.5° obliquity (Fig. 2.1), but it disappears at higher obliquities. This is at odds with the simulations in Ferreira et al. (2014), who argue that the single cell dominating the overturning circulation in their high obliquity simulations results from a merging of the Ferrel cell with a Hadley cell driven by reversed meridional temperature gradients. In the absence of ocean dynamics, at least in this model with our chosen parameters, the resulting cross-equatorial Hadley cell becomes so strong that the associated energy transport, combined with moisture effects, smoothens out temperature gradients in both hemispheres and prevents any significant eddy activity (see Chapter 3). This is also consistent with the absence of any reversal in the meridional PV gradient in the higher obliquity runs (not shown).

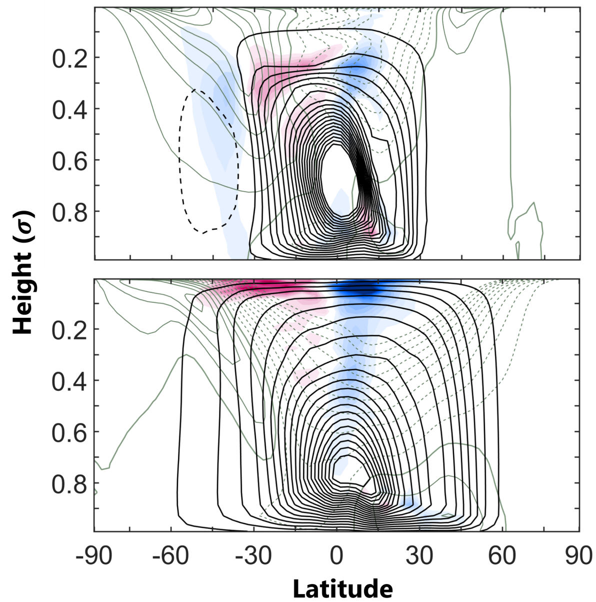

Figure 2.1: Hadley Cell at NH summer solstice for 23.5° (top) and 85° (bottom). Streamfunction is shown in solid black lines (contour intervals of 25×10^9 kg/s), eddy momentum flux divergence, $\nabla\cdot(\overline{u'v'}cos\phi)$, in color contours (contour intervals of 5×10^{-6} m^2/s^2), and zonal wind in gray lines (contour intervals of 10 m/s, with solid (dashed) for positive (negative) values).

2.2 ITCZ

In its simplest definition, the ITCZ is the region of maximum zonal mean tropical precipitation, associated with the ascending branch of the Hadley cell (Kang et al., 2008; Kang et al., 2009). However, when applied to diagnosing the ITCZ position from our simulations, any metric based on the detection of the absolute precipitation maximum presents some challenges. As can be seen from Fig. 1.6, tropical precipitation can have a double, rather than a single, peak structure: in addition to the precipitation peak associated with the ascending branch of the Hadley cell, especially for low obliquities, there exists a secondary precipitation band in the summer hemisphere that remains close to the equator and, at times, can become the locus of most intense rainfall. Additionally, as obliquity increases, not only does the ITCZ shift to higher latitudes, but it also becomes broader and somewhat less defined.

To account for these difficulties, here we detect the ITCZ position using three different methods that exist in the literature: 1. Latitude of maximum precipitation $\phi_{P_{max}}$; 2. Precipitation centroid ϕ_{P_C} (Frierson and Hwang, 2012), defined as the center of mass of the area-integrated precipitation between $\pm\phi_e$:

$$\int_{-\phi_e}^{\phi_{P_C}} P\cos(\phi)d\phi = \int_{\phi_{P_C}}^{\phi_e} P\cos(\phi)d\phi; \tag{2.1}$$

where we have chosen symmetric integration limits, prescribed based on a visual inspection to include the entire precipitation distribution associated with the Hadley cell. The values vary smoothly from 30° to 77° latitude as obliquity increases from 10° to 85°. This cutoff becomes increasingly arbitrary for the higher obliquity cases where additional polar precipitation can blend into the ITCZ, but results are robust to different choices of ϕ_e. 3. An integer power N of area-integrated tropical precipitation (Adam et al., 2016):

$$\phi_{P_N} = \frac{\int_{\phi_a}^{\phi_b} \phi[\cos(\phi)P]^N d\phi}{\int_{\phi_a}^{\phi_b} [\cos(\phi)P]^N d\phi}. \tag{2.2}$$

As discussed in Adam et al. (2016), higher N values provide estimates of the ITCZ that are close to the actual precipitation maximum, but are less sensitive to the horizontal resolution of the precipitation output. We choose N = 10, $\phi_a = -90°$ and $\phi_b = 90°$.

Values of these three different ITCZ metrics are shown in Fig. 2.2 for all simulations. Note that here we show only the maximum latitudinal reach of ϕ_{P_N}, which occurs at different times for the different obliquity values. For instance, in the 85° simulation the ITCZ reaches its maximum poleward excursion one month later than what is seen in the 10° case. The remaining metrics in Fig. 2.2 are shown at the time of maximum ϕ_{P_N}. These three precipitation-based metrics tend to agree well with each other at low obliquities; as obliquity is increased, however, we see that, while $\phi_{P_{max}}$ and ϕ_{P_N} are generally collocated, they become increasingly separated from ϕ_{P_C} (by about 10° in the larger obliquity cases). This reflects an overall widening of the ITCZ. While primarily due to a widening of the Hadley cell ascending branch, the ITCZ broadening also results from changes in the contribution of large-scale eddies to the moisture budget (discussed in the following subsection). More specifically, as poleward temperature and moisture gradients in the summer hemisphere increase with increasing obliquity, large-scale eddies acting down the mean moisture gradient diverge moisture from the higher latitudes and converge it to lower latitudes, right on the equatorward side of the

ITCZ (Fig. 2.3). Correspondingly, the contribution to the total precipitation from large-scale condensation (that is, the one arising from grid-scale saturation rather than that arising from sub-grid convective scale motion) increases in this region, as will be discussed in Section 2.3.

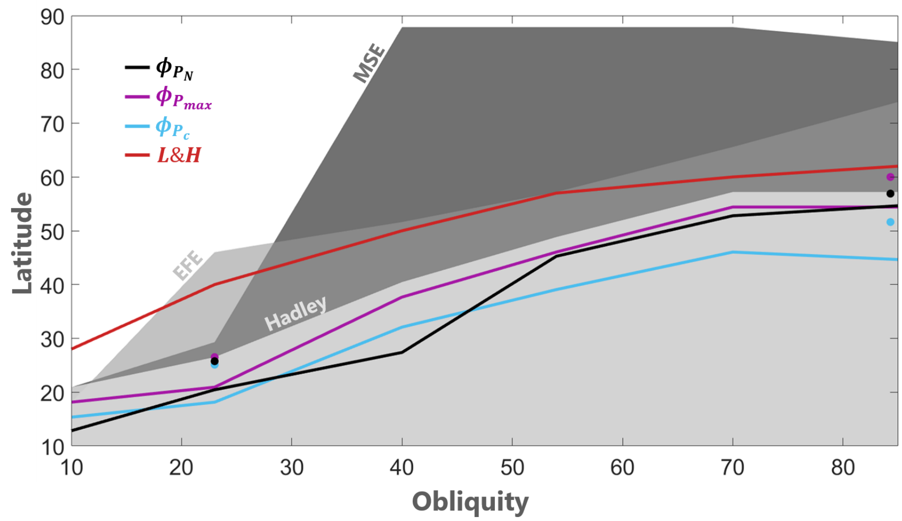

Figure 2.2: Maximal off-equatorial ITCZ reach during NH summer vs obliquity: ϕ_{P_N} (black), ϕ_{P_C} (blue), and $\phi_{P_{max}}$ (magenta). Gray shading indicates latitude of the lower-level MSE maximum (dark), of the EFE (medium), and the Hadley cell extent (light). The red line shows theoretical predictions of the Hadley cell extent from angular momentum conserving theory. The maximum ITCZ reach is also shown for τ_{wv} simulations, using markers of the same colors.

Tracking changes of just the ITCZ's maximum latitudinal reach facilitates comparison between different simulations in Fig. 2.2, but hides some of the changes in timing that occur for higher obliquities and how different metrics capture the corresponding changes in precipitation patterns. In Fig. 2.4, we zoom into the NH summer for 85° obliquity. As it can be seen, the poleward shift of the ITCZ occurs very smoothly during the start of the summer season, during which time the three ITCZ position metrics agree well with each other. At the end of summer, however, tropical precipitation decreases rapidly in the summer hemisphere, before switching to the opposite hemisphere and intensifying there, as the associated warm season begins (Fig. 1.6). The three ITCZ position metrics capture different aspects of these changes in precipitation patterns: the centroid misleadingly portrays a smooth transition into the opposite hemisphere; ϕ_{P_N} briefly moves to the latitudes of the very weak near-equatorial precipitation zone, and $\phi_{P_{max}}$ rapidly shifts to polar latitudes, where a local precipitation peak develops (as discussed more in detail in Section 2.3).

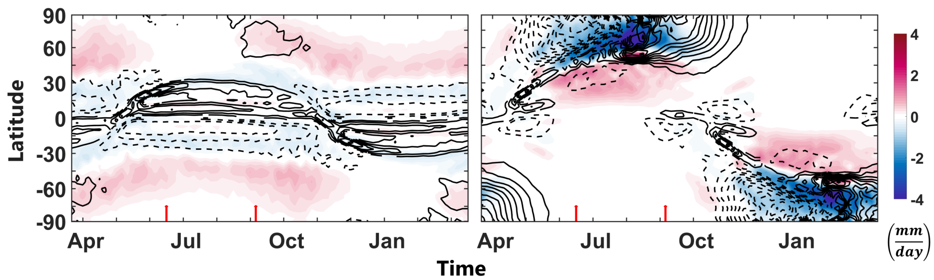

Figure 2.3: Time evolution of the eddy moisture flux convergence (shading, mm/day) and net precipitation (line contours, mm/day). Red arrows on the x-axis indicate the pentads of the time slices in Fig. 2.6.

With these measures of the ITCZ reach in mind, it is of interest to test the applicability of other diagnostics that are not based on precipitation and are traditionally used for Earth's ITCZ. One very common diagnostic used to predict the location of maximum tropical precipitation is the maximum in near-surface MSE. As discussed in Sobel et al. (2007), local thermodynamic constraints would predict maximum convection, and with it maximum lower-level convergence and precipitation, to occur near maximal surface temperatures. When combined with considerations for an angular momentum conserving overturning circulation (Lindzen and Hou, 1988), and quasi-equilibrium theories of moist convection (Emanuel et al., 1994), local controls would suggest the ITCZ's location be just equatorward of the near-surface MSE maximum (Emanuel et al., 1994; Privé and Plumb, 2007; Bordoni and Schneider, 2008).

The location of the near-surface MSE maximum for each obliquity at the time of the maximal ITCZ excursion is plotted in Fig. 2.2 as the dark shaded area. At obliquities larger than 40°, the MSE maximum moves to the pole, following the maximum of solar insolation. And yet, the precipitation maximum does not follow. This emphasizes how the maximum lower-level MSE is not always a good indicator of the ITCZ when planetary regimes other than Earth's are being considered (e.g., Faulk et al., 2017; Hill et al., 2019). As the MSE maximum moves outside of the tropics, convective heating anomalies are no longer communicated to remote regions through gravity waves and horizontal temperature gradients are no longer constrained to be small outside of the boundary layer (Sobel and Bretherton, 2000). In other words, convection can no longer self-organize in a coherent ITCZ over the MSE maximum and suppress convection elsewhere if the MSE maximum is removed from the tropics (e.g., Faulk et al., 2017). As will be discussed in Section 2.3, the region of high-latitude MSE maximum is correlated with polar convective activity; this however remains a local process and is not embedded within the ascending branch of the Hadley cell. Theoretical arguments based on axisymmetric Hadley cell theory as to why lower-level MSE might not always be predictive of the poleward extent of cross-equatorial Hadley circulations have recently been discussed by Hill et al. (2019).

Another commonly used metric of the ITCZ position for Earth's climate is the energy flux equator (EFE), defined as the latitude at which the vertically integrated meridional MSE flux vanishes (Kang et al., 2008). In particular, the vertically integrated atmospheric energy budget in recent years has provided the theoretical framework to understand shifts in the ITCZ induced by remote forcing, as part of the anomalous energy fluxes by the Hadley cell needed to restore energy balance (e.g., Bischoff and Schneider, 2014; Frierson and Hwang, 2012). Under Earth's conditions, where the asymmetry between the two Hadley cells is small, their dividing boundary approximately coincides with the latitude at which the vertically integrated energy transport vanishes. That is to say, the EFE is well defined. As the Hadley cell becomes more hemispherically asymmetric, with a strong, broad, and intense winter cell and vanishing summer cell (e.g., Faulk et al., 2017; Wei and Bordoni, 2018), this boundary becomes ill-defined and in fact does not always correspond with a change of sign in energy or mass transport. For these reasons, here we identify the EFE as the latitude at which the energy transport by the cross-equatorial Hadley cell reduces to 5% of its maximum value. As shown in Fig. 2.2, being a measure of the dividing boundary of the two Hadley cells (or of the poleward extent of the cross-equatorial winter cell), the EFE overestimates the ITCZ position at all obliquities. Yet, it performs better than the MSE maximum, and, at high obliquities, it is only separated by about 10° from the ITCZ.

Given that the EFE and, at least for Earth-like conditions, the lower-level MSE maximum are a metric of the dividing boundary of the two Hadley cells, rather than of the ITCZ position itself, it is also of interest to explore how more direct measures of the circulation extent compare to these other

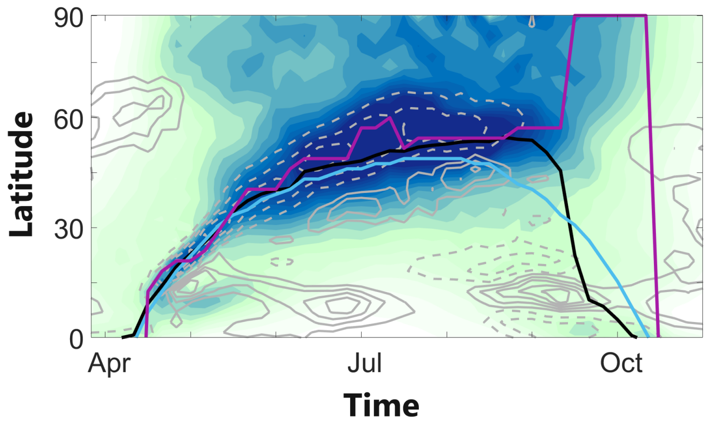

Figure 2.4: ITCZ location over time for 85° obliquity and $\tau_{control}$, during NH summer. Line colors match definitions in Fig. 2.2 with ϕ_{P_N} (black), ϕ_{P_C} (blue), and $\phi_{P_{max}}$ (magenta). Color contours show precipitation with the same color scheme as Fig. 1.6, and gray contours show near surface convergence ($\partial v/\partial y$) where positive (negative) values are shown as solid (dashed) lines.

indicators. Here we take two approaches: we first estimate the poleward extent of the cross-equatorial Hadley cell directly from the simulated overturning mass streamfunction, and then we use estimates based on the angular-momentum conserving theory of Hadley cells forced by off-equatorial heating (e.g., Held and Hou, 1980; Lindzen and Hou, 1988).

The simulated Hadley cell edge, which is shown in light gray shading in Fig. 2.2, much like the EFE, is difficult to define for the high obliquity cases since there is no reversal in the sign of the streamfunction. Hence, here we computed it as the latitude at which the streamfunction decreases to 5% of its maximum values. We also use a cosine factor to account for Earth's geometry, as was first done by Singh (2019), such that $\Psi(\phi)\cos\phi = 0.05\Psi^*\cos\phi^*$ where ϕ^* is the latitude where the streamfunction maximizes, and Ψ^* is the maximum streamfunction value.

The theoretical angular momentum conserving Hadley cell extent of Lindzen and Hou (1988) is obtained utilizing an assumed radiative-equilibrium temperature profile of the form:

$$\theta_{re} = \theta_o\left\{1 + \frac{\Delta_H}{3}[1 - 3(\sin\phi - \sin\phi_o)^2]\right\}. \tag{2.3}$$

Note that Eq. 2.3 is not the GCM forcing; it is the vertically averaged forcing used in Lindzen and Hou (1988), which allows for numerical simplicity. θ_o is a reference temperature (300K), ϕ is latitude, ϕ_o is the latitude of maximum forcing, here interpreted as obliquity, and Δ_H is the fractional change of potential temperature. Values of Δ_H were calculated based on vertically integrated potential temperatures at equinox from the model output, as per the Lindzen and Hou (1988) definition of Δ_H, and ranged from 0.21 to 0.23.

The solution assumes that the regions beyond the Hadley cell are in radiative equilibrium, with temperatures satisfying Eq. 2.3, while within the Hadley cell, temperatures are in gradient-wind balance with the angular momentum conserving winds, yielding:

$$\theta(\phi) = \frac{-\Omega^2 a^2}{2gH}\theta_o \frac{(\sin^2\phi - \sin^2\phi_1)^2}{\cos^2\phi} + \theta(\phi_1), \tag{2.4}$$

where ϕ_1 is the latitude of the dividing boundary between the southern and northern cell, and H is the tropospheric height (here taken as 12 km). By requiring conservation of energy in the Hadley cell region to either side of the ITCZ, and continuity of temperature at the Hadley cell edges, it is possible to solve for ϕ_1, shown in red in Fig. 2.2.

The simulated Hadley cell edge follows a trend similar to the angular momentum conserving limit, which expands with obliquity but remains constrained and does not extend into the polar regions. The agreement between estimates of the cell extent based on the Lindzen and Hou (1988) model and those directly derived from the simulations is not surprising, as strong cross-equatorial circulations tend to approach conservation of angular momentum, at least in their ascending and upper branches, even when eddy fluxes in the winter hemisphere are not negligible (e.g., Schneider and Bordoni, 2008).

2.3 Polar Precipitation

Beyond the ITCZ, there is an increasing tendency for local precipitation maxima to occur at high latitudes with increasing obliquity (Fig. 1.6). A close up of the polar region for 85° obliquity is shown in Fig. 2.5, with contours of the large-scale precipitation. Because the summer pole at high obliquities is where lower-level MSE maximizes, local convective activity does contribute significantly to the polar precipitation during the peak of the summer. Interestingly, however, at the end of the summer, when temperatures are starting to decrease rapidly, large-scale condensation increases sharply as convective activity declines. What determines this rapid increase in large-scale precipitation?

To answer this question, we analyze the vertically integrated moisture budget, which relates the net precipitation $(P-E)$ to the convergence of moisture flux into the atmospheric column and water vapor storage. Further decomposing the water vapor flux into mean and eddy components, the moisture budget becomes:

$$(\overline{P}-\overline{E}) = -\nabla.<\overline{q}\,\overline{\mathbf{u}}> -\nabla.<\overline{q'\mathbf{u'}}> -\partial_t <\overline{q}>, \tag{2.5}$$

where $<\cdot>$ indicates a mass-weighted vertical integral and $\overline{(\cdot)}$ indicates a long term pentad average. The three terms on the right-hand side of Eq. 2.5 represent the mean moisture flux convergence, the eddy moisture flux convergence and the storage terms, respectively. Note that storage is the rate at which water vapor is stored in the atmospheric column (also called precipitable water).

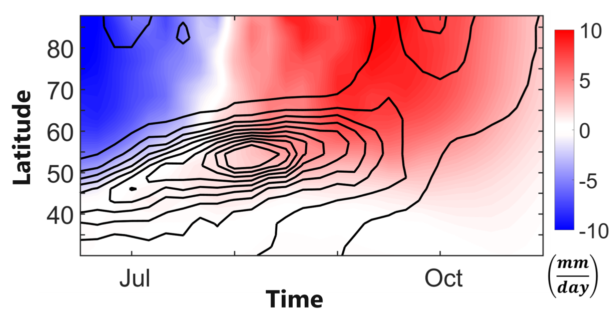

Figure 2.5: Close-up of polar large-scale precipitation (black contours) around the NH warm season for the 85° simulation and $\tau_{control}$ in intervals of 2 mm/day. Color contours show the evolution of storage term $-<\partial q/\partial t>$ for this region, also in mm/day.

The panels in Fig. 2.6 show the moisture budget and contributions by each component for two different time slices, with one slice at peak summer and one in the fall. The specific times at which the slices were taken are indicated with red arrows in Fig. 2.3, which also shows the eddy moisture flux convergence over time. For 23.5° obliquity, we see a balance that is typical of the tropics: the mean moisture flux convergence produces most of the precipitation, with very little contribution from the eddies and an insignificant storage term.

At higher obliquities, we see that this balance is no longer valid. For 85° obliquity the mean moisture flux convergence still dominates over the eddies in the tropics, but neither dominates at the summer pole. It is interesting to see

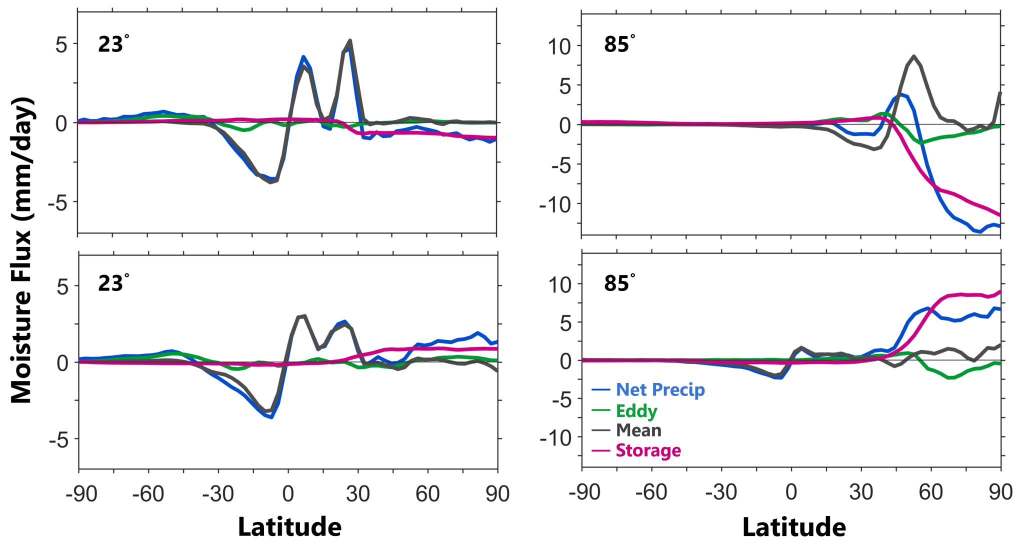

Figure 2.6: Moisture budget decomposition at two times of the seasonal cycle for 23.5°(left) and 85°(right) obliquity and $\tau_{control}$, with net precipitation in blue, mean moisture flux convergence $(-\nabla. < \overline{\mathbf{u}}\,\overline{q} >)$ in dark gray, eddy moisture flux convergence $(-\nabla. < \overline{q'\mathbf{u}'} >)$ in green, and storage $(-\partial_t < q >)$ in pink. All values are in mm/day.

how at the peak and end of the warm season, the summer pole experiences, respectively, large net evaporation ($E > P$) and net precipitation ($P > E$) which are not balanced by moisture flux convergence by either the mean or eddy motions. It is in fact the moisture storage term, which is usually negligible at Earth's obliquities, that takes a dominant role at these times and latitudes.

During the summer at high obliquities, as temperatures increase, so does the water holding capacity of the atmosphere, and hence excess evaporation is primarily stored in the atmospheric column as precipitable water. At the end of summer, temperatures drop rapidly (Fig. 1.2) and the stored water vapor condenses and precipitates out. Storage increases monotonically with obliquity, as can be seen in Fig. 2.7.

It is important to note how these results are not dependent on the specific choice of the optical depth: while the specific value of the optical depth at the poles influences some quantitative aspects of the simulated seasonal cycle, the behavior of the moisture budget remains qualitatively the same, driven by the rapid changes in temperature experienced at the poles. Hence, storage, which is usually neglected in studies of the Earth's hydrological cycle, becomes a leading-order term in climates with more extreme seasonal cycles. The dynamical implications of the polar precipitation will be discussed in Chapter 3, which focuses on extratropical dynamics.

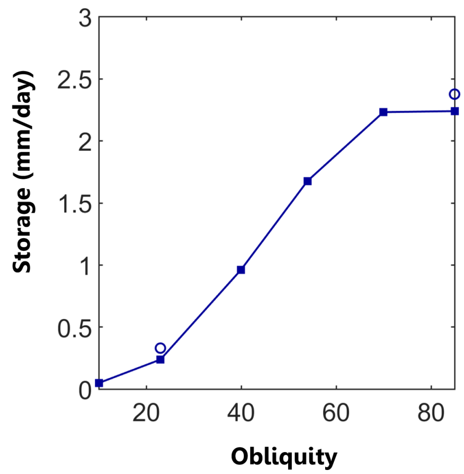

Figure 2.7: Peak value of water vapor storage ($-<\partial q/\partial t>$, averaged from 60 to 90 degrees latitude) in mm/day for various obliquities. Values for $\tau_{control}$ are indicated with squares, and values for τ_{wv} are shown with circular markers.

2.4 Equatorial Secondary Maximum

In the lower obliquity scenarios, tropical precipitation has a double ITCZ structure, with a secondary precipitation band in the summer hemisphere that remains at the same near-equatorial location throughout the summer season. This near-equatorial convergence zone can at times rival the ITCZ in precipitation values and even be the absolute precipitation maximum, with values greater than the ones in the ITCZ (Fig. 1.6). Interestingly, this feature is largely absent at high obliquities, with the result that in the annual mean the near-equatorial region has negative net precipitation (that is, evaporation exceeds precipitation) unlike what is seen on Earth (center panel, Fig. 1.6).

This near-equatorial precipitation maximum is collocated with strong ascending motion in latitudes where the return flow of the lower branch of the cross-equatorial Hadley circulation rises above the boundary layer. This happens well equatorward of the ascending branch, which is close to its poleward boundary. This "jumping" behavior has been shown to be ubiquitous in idealized simulations of cross-equatorial Hadley circulations (e.g., Wei and Bordoni, 2018). But unlike previous studies, in our simulations the "jump" is located in the summer rather than the winter hemisphere (e.g., Pauluis, 2004; Privé and Plumb, 2007).

The dynamics of this near-equatorial jump has been described in detail by Pauluis (2004). In short, strong virtual temperature gradients are necessary for strong meridional flow in the boundary layer around the equator, where the Coriolis parameter is negligible. If that flow cannot be accommodated in the boundary layer, either because of weak virtual temperature gradients or a too shallow boundary layer, the return flow is prevented from occurring in the boundary layer and must in fact occur in the free troposphere.

In order to explore to what extent differences in the near-equatorial and near-surface virtual temperature (and hence pressure) gradients can explain the presence or absence of this secondary precipitation maximum in the low and high obliquity cases, respectively, we use the boundary layer momentum equations introduced by Pauluis (2004). For an axisymmetric model, with a homogenized mixed layer of constant depth (D_{ml}) and constant virtual temperature gradient throughout the layer, Pauluis (2004) shows that the linearized boundary layer momentum equations in steady state become:

$$f v_b - \tau^{-1} u_b = 0, \tag{2.6}$$

$$f u_b + \frac{1}{a}\frac{\partial \Phi}{\partial \phi}\Big|_b + \tau^{-1} v_b = 0, \tag{2.7}$$

where surface friction has been parameterized through a frictional dissipation time scale τ. From Eqs. 2.6 and 2.7, we can solve for the meridional flow v_b:

$$v_b = \frac{-\tau}{(\tau^2 f^2 + 1)}\frac{1}{a}\frac{\partial \Phi}{\partial \phi}\Big|_b, \tag{2.8}$$

with

$$\frac{1}{a}\frac{\partial \Phi}{\partial \phi}\Big|_b = -f u_f - \frac{D_{ml}}{2H_r}\frac{R}{a}\frac{\partial T_v}{\partial \phi}, \tag{2.9}$$

where H_r is the atmospheric scale height, R is the ideal gas constant, a is the planetary radius, T_v is the virtual temperature, and u_f is the zonal velocity right above the mixed layer.

Right at the equator, where the Coriolis parameter is equal to zero, the cross-equatorial meridional flow is entirely driven by the near-surface pressure, and hence, temperature gradient. More generally, free-tropospheric geopotential gradients (which are geostrophically balanced by the term $-fu_f$ in Eq. 2.9) are weak in the near-equatorial region and hence inefficient at driving any cross-equatorial flow. Hence, the meridional component in the Hadley cell return flow nearby the equator is primarily determined by the near-surface virtual temperature gradient, which needs to be positive (negative) to sustain the poleward flow in the NH (SH) during summer, as required by mass balance in a cross-equatorial circulation with ascending branch in the summer hemisphere. In Fig. 2.8 we show the meridional virtual temperature gradients (color contours) from the 23.5° and 85° simulations with $\tau_{control}$. In the 23.5° obliquity simulation, it is evident that the near-surface meridional temperature gradient changes sign in a narrow region which well coincides with the near-equatorial precipitation band. The lower-level poleward flow cannot cross this region at low levels, and hence, has to jump out of the boundary layer, creating lower-level convergence and divergence, respectively, on the upstream and downstream side of it. This behavior is also apparent from the streamlines in Fig. 2.1.

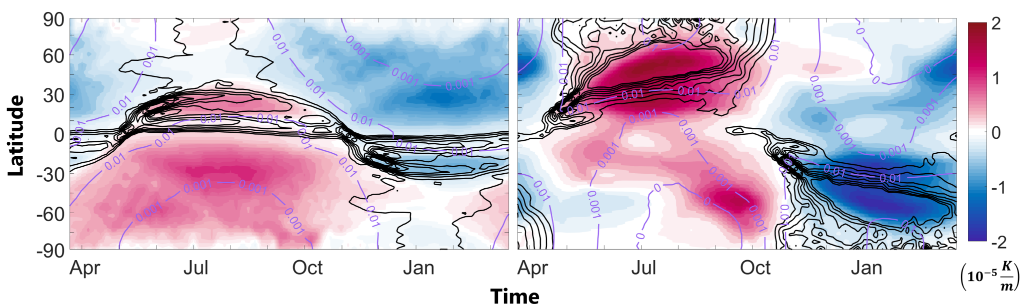

Figure 2.8: Near-surface meridional virtual temperature gradients (color contours, 10^{-5} K/m), precipitation (black line contours from 5 to 12 mm/day), and near-surface specific humidity (gray line contours, kg/kg) vs time for 23.5° (left) and 85° (right) obliquity with $\tau_{control}$.

The absence of the near-equatorial precipitation maximum at higher obliquities is partly explained by differences in the seasonal evolution of the near-surface virtual temperature gradients. More specifically, the near-surface temperature gradient (Fig. 2.8, right panel) remains positive throughout the warm season, with the exception of short times at its beginning and end. These are also the only times when near-equatorial precipitation is nonnegligible (Fig. 1.6, right panel).

While not featuring a reversal in the meridional temperature gradient, the 85° simulation still features an inflection point at around 8 degrees on the summer side of the equator, which would also prevent any poleward flow crossing that region of the boundary layer and would result in a region of lower-level convergence. This inflection point is collocated with the equatorial precipitation maxima at the start and end of summer, and persists throughout the summer even when near-equatorial precipitation is nearly absent (Fig. 2.8). This suggests that reasons other than just the temperature gradients are responsible for the different precipitation patterns in the low and high obliquity cases. Not surprisingly, the availability of moisture also plays a very important role. For low obliquities, the jumping occurs in regions with still relatively high lower-level moisture and MSE. Latent heat release in such moist ascent partially compensates the adiabatic cooling and results in a decrease in gross moist stability, which leads to deep ascent (Pauluis, 2004). For obliquities larger than 54°, MSE and moisture maxima move rapidly away from the equatorial region into higher latitudes, with the lower latitudes being relatively cold and dry throughout the warm season. In this case, any ascent that occurs in this region is effectively dry and, in the absence of circulation-moist convection feedbacks, remains more shallow, as is also evidenced in the flatter streamlines of the return flow in the high obliquity case shown in Fig. 2.1.

In the literature focused on Earth-like dynamics„ debate remains somewhat open as to whether tropical precipitation is more strongly controlled by thermodynamic or dynamic constraints (e.g., Sobel et al., 2007). Thermodynamic theories emphasize the importance of local temperature and moisture, with precipitation and convergence being primarily collocated with SST and MSE maxima (e.g., Neelin and Held, 1987; Sobel and Bretherton, 2000; Privé and Plumb, 2007). Dynamic theories instead consider the boundary layer momentum budget to determine the region of stronger lower-level convergence and hence precipitation (e.g, Lindzen and Nigam, 1987; Pauluis, 2004). Our simulations suggest that both thermodynamic and dynamic arguments can provide powerful constraints on the tropical precipitation distribution. They also emphasize how well-accepted theories for studies of the Earth's hydrological cycle need refinement when applied to more exotic climates (e.g., Hill et al., 2019).

2.5 Discussion of High Obliquity Climate and Habitability

In this chapter, we have systematically explored the impact of increasing obliquity on an Earth-like planet with a completely saturated lower boundary of small thermal inertia and no active ocean. Under these conditions, obliquity-induced insolation changes lead to significant changes in the atmospheric circulation. These are dominated by changes in the solstitial Hadley circulation, which becomes increasingly broad and cross-equatorial as the insolation contrast between the summer and winter hemispheres increases. The winter, cross-equatorial Hadley cell at high obliquity transports so much energy from the summer into the winter hemisphere as to significantly reduce the thermal contrast. The combination of reduced temperature gradients in the winter extratropics and low temperatures (and hence moisture) leads, somewhat surprisingly, to a weakening of eddy activity and absence of precipitating storm tracks.

While becoming broader with increasing obliquity, the solstitial cross-equatorial Hadley cells do not become global even as temperature and MSE maximize at the summer poles, in agreement with energetic and dynamical constraints on these circulations (e.g. Held and Hou, 1980; Guendelman and Kaspi, 2018; Hill et al., 2019) (e.g., (Held and Hou, 1980); Lindzen and Hou, 1988; Guendelman and Kaspi, 2018; Hill et al., 2019). This is worth emphasizing, as in the Earth's literature, the maximum in lower-level MSE is commonly used as a proxy for the poleward extent of the zonally averaged and monsoonal Hadley circulations (e.g., Privé and Plumb, 2007; Shekhar and Boos, 2016). It is clear that this constraint fails in a broader planetary context.

While not embedded within the ascending branch of the cross-equatorial Hadley cell, the summer poles in high-obliquity planets still experience non-negligible precipitation. This arises from both locally forced convection at the peak of the summer, when the summer pole is the hottest place on the planet, and condensation of atmospheric water vapor at the end of the summer, as temperatures drop rapidly. This shall be discussed further in Chapter 3.

When considering habitability, the lower obliquity scenarios are at first glance more favorable candidates for life. These planets, such as our own, experience less extreme temperature variations throughout the year. Therefore, if the planet is in the habitable zone, it seems more likely that a large portion of the surface would be viable.

However, higher obliquities might not be as unfavorable to life as it might seem. Extreme temperature variations could be dampened, for example, by an ocean, in which case the higher obliquity planets would be just as viable as the low obliquity cases. Even in the absence of an active ocean, the atmospheric circulation appears to be able to provide a pathway through which temperature extremes are significantly dampened. Caveats to bear in mind are the absence in our model of important feedbacks, such as those related to ice albedo and clouds, which might have both quantitative and qualitative impacts on our results. These will be explored in future studies.

Furthermore, the response of the ITCZ and surface temperature gradients to obliquity leads to significant changes in the precipitation distribution at all latitudes. At high obliquities, the mid-to-high latitudes become regions of high annual mean net precipitation, while the equator becomes a region of net evaporation. Therefore, the distribution of wet and arid regions would be roughly reversed and this could alter which regions would most likely be hospitable.

Thus, while we cannot make absolute statements about habitability and we have not sought to reproduce any individual planet, increased obliquity leads to seasonal phenomena that shape in fundamental ways the planet's climate. Obliquity is therefore an important consideration for climate characterization, intensifying the need to not only study planetary mean climate but also seasonal behavior.

References

O. Adam, T. Bischoff, and T. Schneider. Seasonal and interannual variations of the energy flux equator and ITCZ. Part I: Zonally averaged ITCZ position. *Journal of Climate*, 29(9):3219–3230, 2016. ISSN 08948755. doi:10.1175/JCLI-D-15-0512.1.

T. Bischoff and T. Schneider. Energetic Constraints on the Position of the Intertropical Convergence Zone. *Journal of Climate*, 27(13):4937–4951, 2014. ISSN 08948755. doi:10.1175/JCLI-D-13-00650.1.

S. Bordoni and T. Schneider. Monsoons as eddy-mediated regime transitions of the tropical overturning circulation. *Nature Geoscience*, 1:515–519, 2008. ISSN 1752-0894. doi:10.1038/ngeo248.

K. A. Emanuel, J. David Neelin, and C. S. Bretherton. On large-scale circulations in convecting atmospheres. *Quarterly Journal of the Royal Meteorological Society*, 120(519):1111–1143, jul 1994. ISSN 00359009. doi:10.1002/qj.49712051902.

S. Faulk, J. Mitchell, S. Bordoni, S. Faulk, J. Mitchell, and S. Bordoni. Effects of rotation rate and seasonal forcing on the ITCZ extent in planetary atmospheres. *Journal of the Atmospheric Sciences*, pages JAS–D–16–0014.1, 2017. ISSN 0022-4928. doi:10.1175/JAS-D-16-0014.1.

D. Ferreira, J. Marshall, P. A. O'Gorman, and S. Seager. Climate at high-obliquity. *Icarus*, 243:236–248, 2014. ISSN 10902643. doi:10.1016/j.icarus.2014.09.015.

D. M. W. Frierson and Y. T. Hwang. Extratropical influence on ITCZ shifts in slab ocean simulations of global warming. *Journal of Climate*, 25(2): 720–733, 2012. ISSN 08948755. doi:10.1175/JCLI-D-11-00116.1.

I. Guendelman and Y. Kaspi. An axisymmetric limit for the width of the hadley cell on planets with large obliquity and long seasonality. *Geophysical Research Letters*, 45(24):13,213–13,221, 2018. ISSN 19448007. doi:10.1029/2018GL080752.

I. M. Held and A. Y. Hou. Nonlinear Axially Symmetric Circulations in a Nearly Inviscid Atmosphere. *Journal of the Atmospheric Sciences*, 37(3): 515–533, 1980. doi:10.1175/1520-0469(1980)037<0515:NASCIA>2.0.CO;2.

S. A. Hill, S. Bordoni, and J. L. Mitchell. Axisymmetric constraints on cross-equatorial hadley cell extent. *Journal of the Atmospheric Sciences*, 76(6): 1547–1564, 2019. ISSN 15200469. doi:10.1175/JAS-D-18-0306.1.

S. M. Kang, I. M. Held, D. M. Frierson, and M. Zhao. The response of the ITCZ to extratropical thermal forcing: Idealized slab-ocean experiments with a GCM. *Journal of Climate*, 21(14):3521–3532, 2008. ISSN 08948755. doi:10.1175/2007JCLI2146.1.

S. M. Kang, D. M. W. Frierson, and I. M. Held. The Tropical Response to Extratropical Thermal Forcing in an Idealized GCM: The Importance of Radiative Feedbacks and Convective Parameterization. *Journal of the Atmospheric Sciences*, 66(9):2812–2827, 2009. ISSN 0022-4928. doi:10.1175/2009JAS2924.1.

R. S. Lindzen and A. Y. Hou. Hadley circulations for zonally averaged heating centered off the equator. *Journal of the Atmospheric Sciences*, 45(17):2416–2427, 1988. ISSN 0022-4928. doi:10.1175/1520-0469(1988)045<2416:HCFZAH>2.0.CO;2.

R. S. Lindzen and S. Nigam. On the Role of Sea Surface Temperature Gradients in Forcing Low-Level Winds and Convergence in the Tropics. *Journal of the Atmospheric Sciences*, 44(17):2418–2436, sep 1987. ISSN 0022-4928. doi:10.1175/1520-0469(1987)044<2418:OTROSS>2.0.CO;2.

T. M. Merlis and T. Schneider. Atmospheric dynamics of earth-like tidally locked aquaplanets. *Journal of Advances in Modeling Earth Systems*, 2(4): 1–17, 2010. ISSN 1942-2466. doi:10.3894/JAMES.2010.2.13.

J. D. Neelin and I. M. Held. Modeling Tropical Convergence Based on the Moist Static Energy Budget. *Monthly Weather Review*, 115(1):3–12, jan 1987. ISSN 0027-0644. doi:10.1175/1520-0493(1987)115<0003:MTCBOT>2.0.CO;2.

O. Pauluis. Boundary Layer Dynamics and Cross-Equatorial Hadley Circulation. *Journal of the Atmospheric Sciences*, 61(10):1161–1173, 2004. ISSN 0022-4928. doi:10.1175/1520-0469(2004)061<1161:BLDACH>2.0.CO;2.

N. C. Privé and R. A. Plumb. Monsoon Dynamics with Interactive Forcing. Part I: Axisymmetric Studies. *Journal of the Atmospheric Sciences*, 64(5): 1417–1430, 2007. doi:10.1175/JAS3916.1.

T. Schneider and S. Bordoni. Eddy-Mediated Regime Transitions in the Seasonal Cycle of a Hadley Circulation and Implications for Monsoon Dynamics. *Journal of the Atmospheric Sciences*, 65(3):915–934, mar 2008. ISSN 0022-4928. doi:10.1175/2007JAS2415.1.

R. Shekhar and W. R. Boos. Improving energy-based estimates of monsoon location in the presence of proximal deserts. *Journal of Climate*, 29(13): 4741–4761, 2016. doi:10.1175/JCLI-D-15-0747.1.

M. S. Singh. Limits on the extent of the solsticial Hadley cell: the role of planetary rotation. *Journal of the Atmospheric Sciences*, pages 1989–2004, 2019. ISSN 0022-4928. doi:10.1175/jas-d-18-0341.1.

A. H. Sobel and C. S. Bretherton. Modeling tropical precipitation in a single column. *Journal of Climate*, 13(24):4378–4392, 2000. ISSN 08948755. doi:10.1175/1520-0442(2000)013<4378:MTPIAS>2.0.CO;2.

A. H. Sobel, G. Bellon, and J. Bacmeister. Multiple equilibria in a single-column model of the tropical atmosphere. *Geophysical Research Letters*, 34 (22):1–5, 2007. ISSN 00948276. doi:10.1029/2007GL031320.

H.-h. Wei and S. Bordoni. Energetic constraints on the ITCZ in idealized simulations with a seasonal cycle. *Journal of Advances in Modeling Earth Sciences (JAMES)*, pages 1–35, 2018.

W. Zhou and S. P. Xie. A hierarchy of idealized monsoons in an intermediate GCM. *Journal of Climate*, 31(22):9021–9036, 2018. ISSN 08948755. doi:10.1175/JCLI-D-18-0084.1.

Chapter 3

EXTRATROPICAL CIRCULATION AND MOISTURE STORAGE

Planetary atmospheric general circulations are driven by top-of-atmosphere radiative imbalances, arising from local differences between the absorbed stellar shortwave radiation and the longwave radiation emitted to space. On long timescales, a local surplus of energy must be compensated for by energy export by atmospheric and oceanic circulations towards regions of energy deficit. But on shorter time scales, energy storage in the atmospheric column and/or the planetary surface can play a role. Understanding how changes in the energy budget impact the atmospheric circulation and surface climate is a challenge fundamental to atmospheric dynamics, and is of increasing interest for exoplanet studies, where top of atmosphere radiation is the main observable quantity available for climate characterization. In this chapter, we use an idealized general circulation model (GCM) to study the response to changes in shortwave and longwave radiation of the seasonally varying atmospheric circulation of Earth-like planets, its impact on surface climate, and the response of the extratropical and polar circulation.

On Earth, most of the atmospheric energy transport in the tropics is effected by the Hadley cells. Here we neglect ocean heat transport, which is responsible for a significant portion of the total energy transport in the deep tropics (Held, 2001). Under equinox conditions, the Hadley cells are roughly hemispherically symmetric, with both ascending branches near the equator. Under solstice conditions, the summer cell becomes weaker and the winter Hadley cell strengthens and expands, in response to the insolation peak moving poleward (Lindzen and Hou, 1988), as also happens with increased obliquity (Fig. 3.1 a,c). However, the Hadley cell is dynamically constrained and cannot expand beyond the midlatitudes at Earth's rotation rate (Held and Hou, 1980; Faulk et al., 2017; Kaspi and Showman, 2015; Guendelman and Kaspi, 2019) even with extreme insolation changes (Lobo and Bordoni, 2020; Guendelman and Kaspi, 2018). Thus, increased radiative imbalances at the poles, beyond the winter Hadley cell's reach, require additional changes in atmospheric circulations other than the Hadley cells.

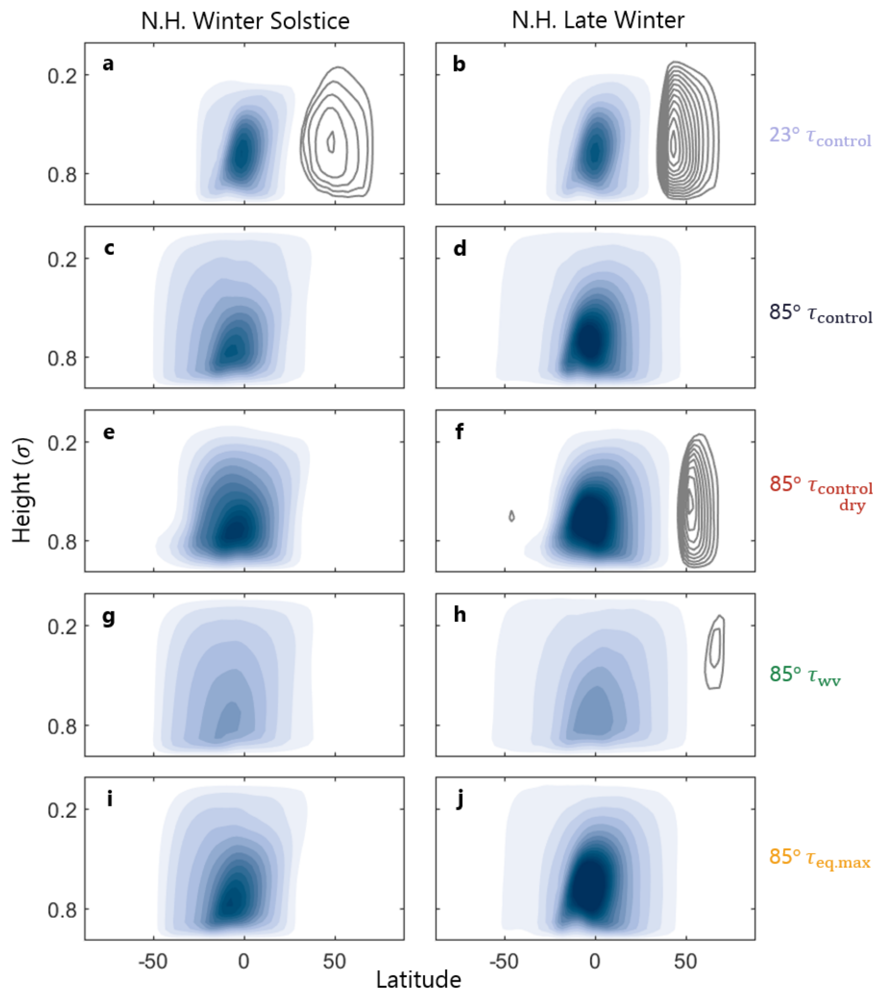

Figure 3.1: Contours of stream functions during northern hemisphere winter solstice (day 270, left) and late winter (day 330, right). Color contours show the clockwise winter Hadley cell, with intervals of 5×10^{10} kg/s. Grey lines show stream function values for the counter-clockwise winter Ferrel cells, with intervals of 5×10^{9} kg/s and a minimum cutoff of 10^{10} kg/s. The top 2 rows compare simulations with constant optical depth (τ_{control}), at 23° (a,b) and 85° (c,d) obliquity. The middle row (e,f) shows a dry version of the simulation above. The bottom rows show 85° obliquity with τ_{wv} (g,f) and $\tau_{\text{eq.max}}$ (i,j) optical depth setups.

The dynamical constraints on the Hadley cell have an important impact on the hydrological cycle, for instance determining the position of the region of most intense tropical precipitation within the intertropical convergence zone (ITCZ). Lobo and Bordoni (2020) showed that for high obliquity simulations, the ITCZ remains in the midlatitudes, as does the ascending branch of the winter Hadley cell in solsticial seasons, even if near-surface temperature and moist static energy (MSE) maximize at the summer pole. They also discussed important features of the hydrological cycle outside of the latitudes spanned by the Hadley circulations. At the poles, nonnegligible precipitation is seen during the summer season. This is driven by small-scale convection over the near-surface MSE maximum early in the summer, and by large-scale condensation at the end of the summer. Moisture budget analyses revealed how this arises from rapid variations in the atmospheric water holding capacity due to rapid decreases in temperature at the end of the warm season (see Chapter 2.3). The lack of a storm track in the winter hemisphere was also noteworthy.

Storm tracks, bands of enhanced precipitation particularly evident in the extratropics of the winter hemisphere, are associated with moisture flux convergence by large-scale baroclinic eddies, fueled by available potential energy in regions of strong horizontal temperature gradients (Schneider and Walker, 2006; Peixoto and Oort, 1992). Thus their intensity and position can vary significantly throughout the season, as temperature gradients shift in position and/or magnitude. One would expect that large solsticial meridional insolation gradients would have strong meridional temperature gradients and enhanced eddy activity. However, high obliquity simulations with idealized GCMs (Lobo and Bordoni, 2020; Guendelman and Kaspi, 2018; Ferreira et al., 2014) where the solsticial pole-to-pole insolation gradient is maximized indicate a significant strengthening of the winter Hadley cell but a surprising general reduction of baroclinic eddy activity, particularly around the winter solstice. This results in a weakening or absence of the storm tracks and of the winter Ferrel cell.

The relationships between radiative forcings, surface climate, and the atmospheric circulation are complex and include many nonlinear interactions. Some of the strongest nonlinearities in the climate system are associated with atmospheric water vapor, which has a strong nonlinear dependence on temperature through the Clausius Clapeyron relation. More specifically, water vapor can impact the surface climate, especially when seasonal cycles are considered, through a number of pathways: i. it is a potent greenhouse gas, exerting a strong positive radiative feedback (e.g. Held and Soden, 2000); ii. it undergoes phase transitions, with the associated latent heat release/absorption having direct and indirect impacts on the temperature distribution, the atmospheric circulation, and the hydrological cycle in the tropics (Neelin and

Held, 1987; O'Gorman, 2011; Pfahl et al., 2015; Feldl et al., 2017; Lobo and Bordoni, 2020); iii. finally, it can alter the effective heat capacity of the atmospheric column (e.g. Cronin and Emanuel, 2013), thus exerting an impact on the response to any seasonally varying forcing.

3.1 Aquaplanet Simulations

We use the idealized GCM of an ideal-gas atmosphere (Frierson et al., 2007; O'Gorman and Schneider, 2008), as described in Chapter 1.1, with a uniform slab ocean of constant depth (aquaplanet) and constant surface albedo of 0.38. The model uses a two-stream gray radiation scheme and a 360 day seasonal cycle of insolation. In this configuration there is no ocean heat transport.

To explore the response of the atmospheric circulation to radiative perturbations, we run simulations with changes to both the prescribed shortwave radiation and longwave optical depth. Changes in shortwave radiation are introduced by varying the planetary obliquity, with values equal to 23°, 40°, 54°, 70°, and 85°. Changes in longwave are obtained by varying the pole-to-equator structure of the optical depth, at both 23° and 85° .

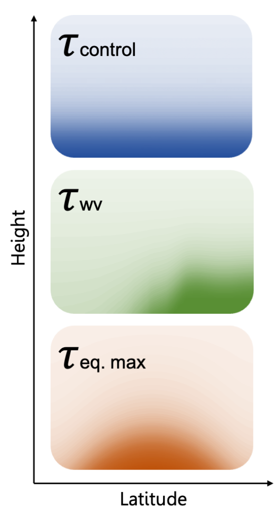

Figure 3.2: Cartoon of optical depth structures.

In the control runs (τ_{control}) the prescribed longwave optical depth of the atmosphere only varies vertically as a function of pressure. The vertical structure reproduces a well mixed CO_2-like absorber and a bottom-heavy "water vapor" absorber:

$$\tau(p) = \tau_o \left[f\left(\frac{p}{p_0}\right) + (1-f)\left(\frac{p}{p_0}\right)^4 \right] \tag{3.1}$$

where $\tau_{\mathrm{o}} = 4.57$ and $f = 0.2$. Given that τ is fixed and independent of water vapor concentration, there is no water vapor feedback.

We perform additional simulations in which the prescribed optical depth is also a function of latitude, maximizing at the equator and minimizing at the poles ($\tau_{\text{eq. max.}}$), according to:

$$\tau_o = \tau_{o_{eq}} + (\tau_{o_{pole}} - \tau_{o_{eq}}) \sin^2(\phi), \tag{3.2}$$

where ϕ is latitude, $\tau_{\mathrm{o_{eq}}} = 7.2$ and $\tau_{\mathrm{o_{pole}}} = 1.8$. These are the same values as those used in O'Gorman and Schneider (2008) to study the annual mean atmospheric circulation on Earth. $\tau_{\text{eq.max}}$ has an optical depth lower than τ_{control} poleward of 45° latitude.

We also include simulations where the optical depth varies over time according to the local water vapor concentration (τ_{wv}), thus providing a simple representation of the water vapor feedback (Merlis and Schneider, 2010), with the optical depth modified as:

$$\tau(p) = \tau_{\mathrm{o}} \left(\frac{p}{p_0}\right) + \tau_{\mathrm{o_{wv}}} \left(\frac{p}{p_0}\right)^4, \tag{3.3}$$

where $\tau_{o_{\text{wv}}}$ is the vertically integrated specific humidity, divided by an empirical constant (98 Pa) chosen so that $\tau_{o_{\text{wv}}}$ remains order one. τ_o is set to 1.39.

All of the parameters in the different optical depth formulations were chosen so that at 23° obliquity, they result in approximately the same planetary global mean temperatures. Thus, we are focusing on the effects of a spatial redistribution of energy, rather than an overall warming or cooling. For comparison, we also show "dry" runs at 23° and 85° obliquity. These simulations have the same optical depth as in τ_{control}, but the saturation vapor pressure is prescribed to be zero everywhere, thus eliminating the atmosphere's ability to store or transport water vapor.

Given that we are particularly interested in the seasonal cycle, we use a shallow 1 m mixed layer depth for most simulations. These conditions result in more extreme seasonal variations than we would expect for an ocean-covered surface on Earth, which helps isolate mechanisms behind the seasonal changes and provides some insight into the climate of Land Planets. We also address the effects of increased surface heat capacity, with results from 85° obliquity simulations with a mixed layer depth of 10, 25, and 50 m. The simulations with increased mixed layer depth more closely represent a planet with an ocean-covered surface (ocean world), with thermal inertia timescales of up to 2 months.

All remaining planetary and orbital parameters are given Earth-like values (as listed in Chapter 1). For simplicity, we only consider planets with Earth's rotation rate in this paper, though we note that for different rotation rates the division between tropical and extratropical dynamical regimes would shift in latitude (see Showman et al. 2013), such that very slow rotating planets would be "all-tropics" planets (Mitchell et al., 2009), with global Hadley cells (Faulk et al., 2017; Guendelman and Kaspi, 2019; Kaspi and Showman, 2015).

3.2 Response to Changes in Shortwave Distribution

We begin by studying the planetary circulation response to obliquity-induced changes in the insolation forcing. Incoming stellar radiation is a prescribed model quantity, and its intensity is easily observable for most planetary systems. Varying the magnitude through changes in orbital radius (e.g. Kaspi and Showman, 2015) or radiative profile (e.g. Wolf et al., 2017) can significantly alter surface climate. But changes in the insolation meridional distribution are at least as important for a planet's climate as its intensity. As a simple means to examine the influence of the insolation spatial distribution, we shall consider simulations where obliquity is varied between 23° (Earth-like) and 85°. In the high obliquity cases, summer insolation has a single maximum at the poles and on the annual average more energy is delivered to the poles than the equator.

Obliquity-induced changes in the seasonal insolation distribution manifest in corresponding changes in the surface temperatures (Fig. 3.3), which tend to follow the insolation pattern albeit with a lag of about a month. Given the small thermal inertia of the lower boundary, this lag arises from atmospheric dynamic and thermal inertia. Not surprisingly, relative to the low obliquity cases, the high obliquity simulations feature more extreme polar temperatures, with very high temperatures during the summer and very cold temperatures during the winter. Hence, the poles in high obliquity simulations experience a much larger range of temperature throughout the seasonal cycle.

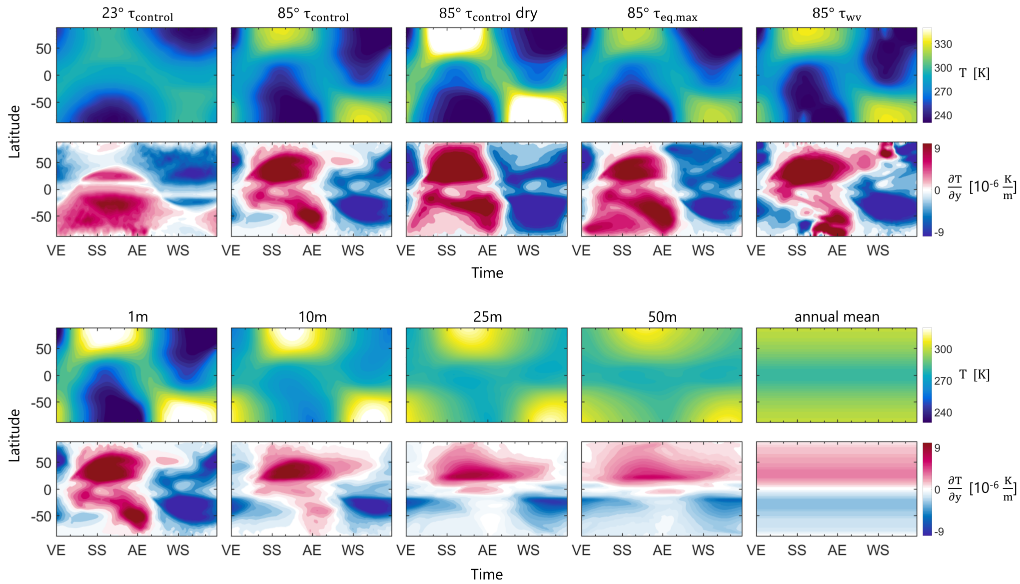

Figure 3.3: Near-surface temperatures (row 1 & 3), and meridional temperature gradient (row 2 & 4). The top panels show values for simulations with different obliquities and optical depth structures. From left to right, these include $23°\tau_{\text{control}}$, $85°\tau_{\text{control}}$, $85°\tau_{\text{control}}$ dry, $85°\tau_{\text{eq.maxl}}$, and $85°\tau_{\text{wv}}$. The bottom panels show 85° obliquity simulations with mixed layer depths increasing from left to right (1, 10, 25 and 50m). The panels on the far right show simulation where insolation is kept at its annual mean value. Note that the temperature color bars are different for each row. The x-axis shows time, labeled at the northern hemisphere vernal equinox (VE), summer solstice (SS), autumnal equinox (AE), and winter solstice (WE).

However, the temperature contrast between the summer and winter hemispheres is weaker than we would expect from radiative equilibrium, due in part to the strong cross-equatorial energy transport by the winter Hadley cell, which significantly broadens and strengthens with increasing obliquity (Fig. 3.1). This results in increased energy transport towards the winter hemisphere, as the Hadley cell tends to transport energy in the direction of its upper-level mass transport. Comparing the low obliquity simulation ($23°$ τ_{control}) to the high obliquity case ($85°$ τ_{control}), we can observe how the winter Hadley cell edges broaden from $\sim 30°$ latitude in either hemispheres at 23° obliquity to $\sim 60°$ latitude at high obliquity. See Hill et al. (2019) for a discussion of theoretical mechanisms that might explain why a winter Hadley cell extends as far into the winter hemisphere as the summer hemisphere. Despite this significant broadening, it is important to emphasize that the cell is not global even in the highest obliquity case and remains within the high midlatitudes (see Fig. 9 in Lobo and Bordoni, 2020).

Given that the Hadley cell does not become truly global, it might seem surprising that in the high obliquity control simulations, there is no evidence of a Ferrel cell in the winter hemisphere (Fig. 3.1 c and d). We might expect that the strong solsticial insolation gradients at high obliquities, which result in a strengthening of the low latitude moist static energy transport, would result in a similar strengthening of the high latitude eddy transport and a corresponding intensification of the winter Ferrel cell. But, while we see a strong winter Ferrel cell for 23° obliquity, both in mid and late winter (Fig. 3.1 a & b), it is entirely absent for 85° τ_{control}.

3.3 Eddy Activity

The absence of the Ferrel cell, and with it of a precipitation storm track, is linked to a reduction in eddy activity. This reduction was previously noted in Lobo and Bordoni (2020), which showed that increasing obliquity from 23° to 85° leads to a monotonic decrease in winter eddy kinetic energy (EKE). Here, we examine its seasonal evolution across simulations. In particular, Fig. 3.4 shows vertically integrated EKE values averaged over the NH mid and high latitudes (between 35 and 90°N). We average over a relatively broad meridional band to capture baroclinic eddy activity across the various simulations. As obliquity is increased, in addition to the EKE weakening, we also see changes in its seasonality, with a weakened, delayed, and shorter lived maximum. In all of the τ_{control} simulations, the maximum in EKE occurs well after the winter solstice, in fact around boreal vernal equinox, and the timing of the maximum shifts roughly 20 days further from solstice with increased obliquity. If we were to choose a threshold to demarcate the start of significant baroclinic eddy activity, e.g. 0.5 MJ/m^2, we would note an even more dramatic delay of roughly 120 days among the control simulations.

Baroclinic eddies form as a result of the vertical shear in the mean flow, sustained through thermal wind balance with the mean meridional temperature gradients. One of the Charney-Stern-Pedloski necessary conditions for baroclinic instability is that the near surface vertical gradient of the horizontal

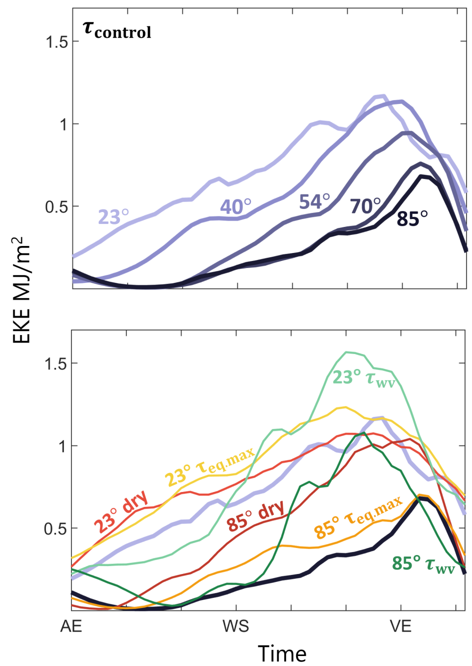

Figure 3.4: NH winter EKE, vertically integrated and averaged between 35 and 90° latitude. EKE values are shown over time, measured in days since equinox. We use a 3 pentad simple rolling average to make the figure easier to read. The top panel shows τ_{control} results, and the bottom panel shows a variety of configurations at 23° and 85° obliquity. Dry τ_{control} simulations are shown in red, τ_{wv} in green and $\tau_{\text{eq.max}}$ in yellow.

flow (U_z) has the same sign as the interior potential vorticity gradient. The potential vorticity combines the flow's relative vorticity, planetary rotation, and a measure of column thickness to describe the absolute circulation of a given air parcel. The meridional gradient of mean quasi-geostrophic potential vorticity (q_y) can be written as:

$$\overline{q_y} = \beta - \overline{u_{yy}} + f^2 \frac{\partial}{\partial p}\left(\frac{1}{S^2}\frac{\partial \overline{u_p}}{\partial \overline{\theta_p}}\right), \tag{3.4}$$

where β is the meridional gradient of the Coriolis parameter (f), θ is the potential temperature, and $S^2 = R(p/p_0)^k p^{-1}$ (R is the ideal gas constant, p_0 is a reference surface pressure, and $k = 2/7$). In our simulations, q_y is dominated by the beta effect and is positive. Based on thermal wind, this implies that the necessary condition for baroclinic instability during NH winter is that the meridional temperature gradient is negative. We can clearly confirm that this is the case by examining the top panels in Fig. 3.5, which show near-surface meridional temperature gradients (color contours) and EKE (black contours) throughout the NH winter. For 23° obliquity, extratropical meridional temperature gradients become predominantly negative just before boreal autumnal equinox (Fig. 3.5a) and eddy activity increases shortly after as the gradients intensify. For 85° obliquity the necessary condition for instability is only met briefly at the end of the winter, well after the solstice and around boreal vernal equinox, and baroclinic eddy activity is only sustained during the short time interval in which gradients remain negative (Fig. 3.5b).

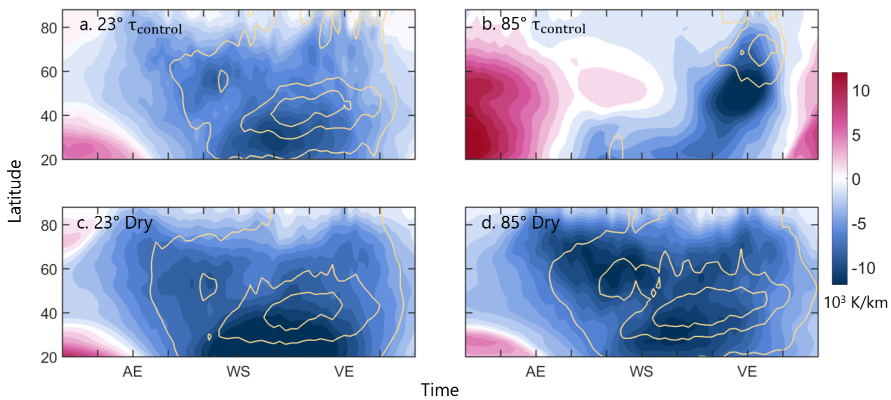

Figure 3.5: NH near surface meridional temperature gradients (K/km, color contours) during NH winter. Vertically integrated EKE (intervals of 0.5 MJ/m^2, line contours). The panels show values for 23° (left) and 85° (right) simulations, both with τ_{control} (top) and dry (bottom) configurations.

3.4 Role of Moisture in the Temperature Seasonal Evolution

What is causing the delay in the timing of the temperature gradient reversal in the high obliquity simulations? Or, in other words, why does the pole emerging from the summer season cool more slowly when obliquity is large? Note that we focus primarily on the seasonal evolution of high-latitude temperatures because changes in equatorial temperatures are smaller than those at the poles, and no significant shift in the timing of their variations is observed. This is not to say that there are no changes at the low latitudes, but rather that the changes are small compared to the polar seasonal effects. We will briefly discuss some low latitude effects in Section 3.6.

To gain some insight into the different seasonal cycles of near-surface temperatures at low and high obliquities, we consider the vertically integrated atmospheric energy budget (e.g. Neelin, 2007):

$$\frac{\partial}{\partial t} < \overline{(c_pT + L_vq)} > + \frac{\partial}{\partial y} < \overline{vh} >= R_{toa} - F_{sfc}, \tag{3.5}$$

where $h = c_pT + L_vq + gz$ is the moist static energy, comprised of dry enthalpy c_pT, with air isobaric specific heat c_p, potential energy gz, and latent energy L_vq, with latent heat of vaporization L_v and specific humidity q. Vertical integrals are denoted by $<>$, and the $\overline{(\cdot)}$ denotes both a zonal and a temporal long term pentad average. The first term on the left hand side represents energy storage in the atmospheric column, while the second term is the divergence of the meridional energy flux $< \overline{vh} >=< \overline{v}\overline{h} > + < \overline{v'h'} >$, comprised of mean and eddy energy fluxes, respectively. The right hand side of Eq. 3.5 represents the net energy input (NEI) into the atmospheric column, through top-of-atmosphere radiative fluxes R_{toa} and surface radiative and turbulent enthalpy fluxes F_{sfc}. At lower latitudes, regardless of obliquity value, the dominant balance is between the net energy input, and the MSE flux divergence (Fig. 3.6). However, as obliquity is increased, the net energy input can be very large in the high latitudes, with negative values, indicative of energy deficit, in the high latitudes of the winter hemisphere, and positive values, indicative of energy surplus, in the high latitudes of the summer hemisphere (Fig 3.6). The weak MSE flux convergence/divergence at these polar latitudes implies an increasing role of the atmospheric energy storage, which include both a dry ($< \partial_t\overline{c_pT} >$) and latent ($< \partial_t\overline{L_vq} >$) component. Importantly, in a moist atmosphere, changes in net energy input are accompanied by changes in latent energy (moisture) in addition to changes in dry enthalpy (temperature). In other words, moisture can buffer temperature changes in response to insolation changes. Fig. 3.6 shows the different terms of the MSE budget at different times of the seasonal cycle for all simulations. Below, we will however primarily focus on the behavior of the high obliquity simulation compared to the low obliquity simulation, and we will focus on the high latitudes for the reasons articulated above.

As the net energy input starts increasing in the warm hemisphere after spring equinox, both in the low and high obliquity simulations we see an increase in energy storage, initially in the dry component and then, with a slight

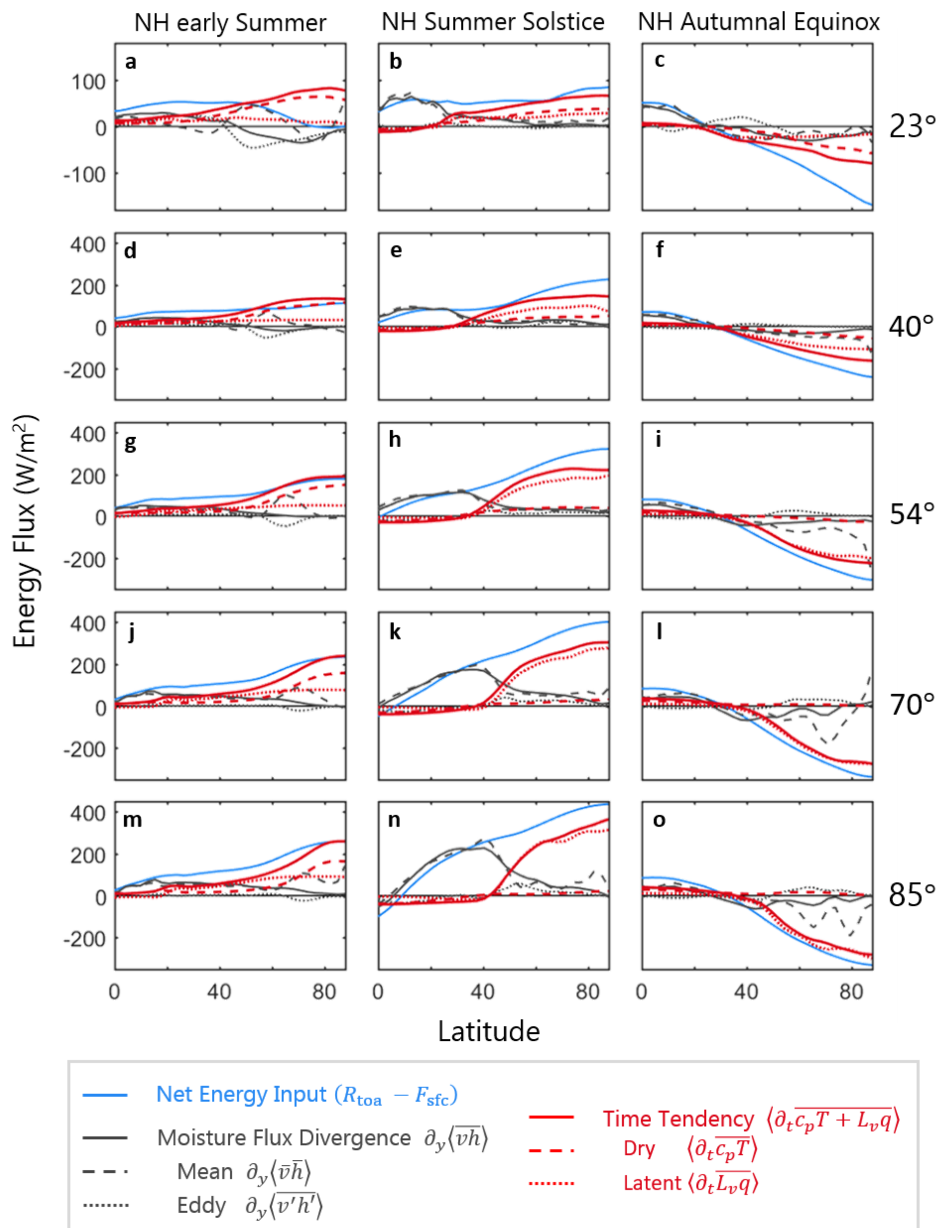

Figure 3.6: Moist static energy budget and the role of energy storage during seasonal transitions. Panels on the left show NH in early summer (40 days after VE), center shows summer solstice, and panels on the right show autumnal equinox. Net energy input into the atmosphere (blue) is predominantly balanced by mean moisture flux convergence (dashed grey) in the low latitudes. In the high latitudes, time tendencies terms, both dry (dashed red) and latent (dotted red) play a dominant role.

lag, in the latent energy component as well (Fig. 3.7). As summer progresses, the relative contribution of the latent energy storage increases and does more so with higher obliquity: at summer solstice, it is about as large as the dry energy storage in the low obliquity simulation and it is the dominant component in the high obliquity simulation. By providing an alternative means of energy storage, moisture hence provides a buffering effect on the temperature response to changes in radiative forcing with obliquity, which both reduces the temperature maximum and delays its occurrence relative to the time of summer solstice as obliquity is increased. This delay is about 10 days larger in the 85 than in the 23 case (not shown).

The transition from the summer to the winter season reveals even more striking differences between the low and high obliquity simulations. In the low obliquity case, the net energy input, which becomes negative around 50 days after summer solstice, is primarily balanced by MSE flux convergence and dry enthalpy loss, with latent energy loss playing a negligible role. Significant atmospheric cooling is seen to occur between autumnal equinox and winter summer solstice. At high obliquity, instead, the large and negative net energy input around autumnal equinox is primarily balanced by loss of latent energy in the atmospheric column, which reduces and slows down the dry enthalpy loss, which becomes negative only around autumnal equinox and peaks around 50 days later. In other words, latent energy loss at high obliquity also buffers the temperature response in the winter season, slowing down and delaying the cooling due to the negative NEI.

We explore in more detail the behavior of atmospheric energy storage throughout the winter in the high latitudes in Fig. 3.9, which shows the rate at which the vertically integrated atmospheric column is losing dry and latent energy. The dry enthalpy loss also increases with increasing obliquity, but as discussed above, its relative contribution to the total energy storage decreases. There is also evidence of delay in the time at which it reaches its minimum value. The latent energy loss is strongest at equinox, with small variations in timing, but large variations in intensity amongst the simulations, showing a monotonic increase in magnitude with increased obliquity. The dry enthalpy loss shows a much smaller magnitude increase than the latent energy loss, switching from being the primary means of energy loss in the low obliquity simulation to playing a more minor role in the high obliquity simulations.

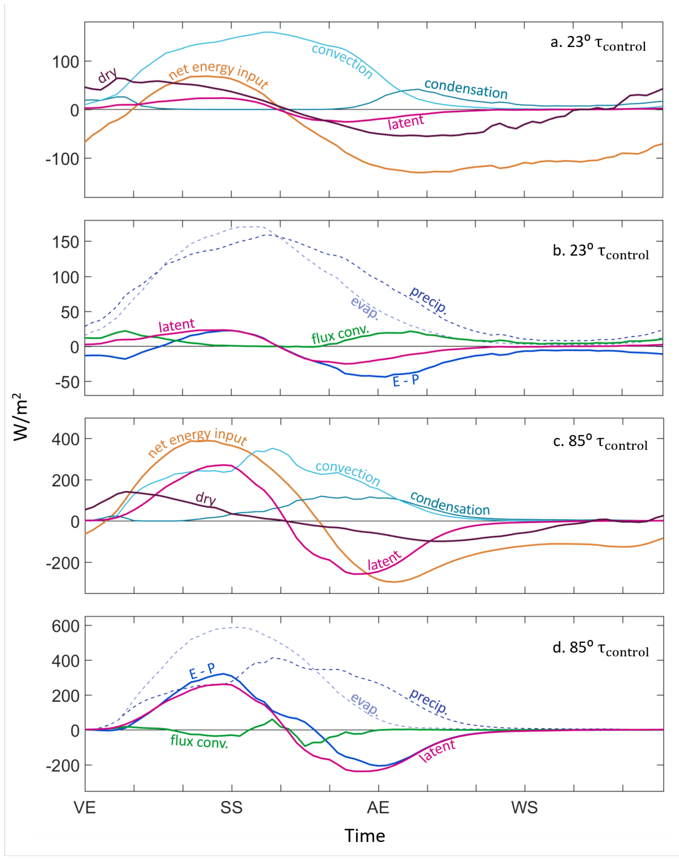

Figure 3.7: Evolution of energy budget terms (a,c) and moisture budget (b,d) throughout the year for the 23° and 85° τ_{control} simulations. Values show the area weighted average between 60 and 90°N. Panels a and c show changes in atmospheric dry (brown) and latent (pink) energy storage, in comparison with the net energy input into the atmosphere. Energy release from convection (light blue) and condensation (dark blue) are also shown. Panels b and d show the net precipitation (blue) and moisture flux convergence (green) which balance the atmospheric moisture storage (pink). The net precipitation is defined as evaporation (dashed light blue) and precipitation (dashed dark blue).

The role that atmospheric moisture plays in shaping the temperature distribution can be further explored by using the vertically integrated moisture budget, which relates the water vapor storage in the atmosphere to the net precipitation (P-E) and convergence of moisture flux by atmospheric motion:

$$\partial_t < \overline{q} >= \overline{E} - \overline{P} - \nabla\cdot < \overline{q}\,\overline{\mathbf{u}} > -\nabla\cdot < \overline{q'\mathbf{u}'} >, \tag{3.6}$$

The left hand side represents the storage term, while the right hand side includes net evaporation, and mean and eddy moisture flux convergence.

All terms of the moisture budget are also shown in Fig. 3.7 for both the 23° and the 85° cases. In the 23° simulation, the small excess evaporation after vernal equinox is balanced by both moisture flux convergence and moisture storage. As the warm season progresses, evaporation grows in excess of precipitation and this is primarily accompanied by an increase in atmospheric moisture (or equivalently in latent energy), which peaks around summer solstice. The large evaporation is driven by large surface temperature and MSE, which sustain some degree of convective activity (Fig. 3.7a). About a month after summer solstice, precipitation starts exceeding evaporation (Fig. 3.7b), which is initially balanced by a decrease in atmospheric moisture, at which time large-scale condensation starts picking up. Near autumnal equinox, however, net precipitation is primarily balanced by eddy moisture flux convergence rather than local condensation. This high-latitude precipitation is however much smaller than the precipitation seen at lower latitudes at the same time, and the associated latent heat release is not large enough to compensate the radiative cooling tendency, resulting in dry enthalpy loss and atmospheric cooling lasting from before autumnal equinox throughout winter solstice (not shown).

In the 85° simulation, we see a much smaller role for moisture flux convergence by the atmospheric circulation and, with the exception of about a month before autumnal equinox, the dominant balance is between moisture storage and net evaporation. Similarly to what is seen in the 23° case, evaporation exceeds precipitation from around vernal equinox to about a month before autumnal equinox, during which time the moisture storage is positive (Fig. 3.7d). Differently than the low obliquity case, however, the high near-surface temperatures and MSE maintain vigorous convection throughout the summer, with precipitation rates smaller than, but of the same order of magnitude of, precipitation rates within the ITCZ (c.f. Lobo and Bordoni, 2020). As evaporation rates decrease towards the end of the summer, but the high near-surface surface temperatures continue to sustain convection, precipitation starts exceeding evaporation about one month before autumnal equinox. This is primarily balanced, especially as net precipitation reaches its peak at autumnal equinox, by latent energy loss. Note how the latent heat release associated with both the convective and large-scale precipitation associated with this vigorous convective activity is large enough to compensate for the radiative cooling from summer solstice throughout autumnal equinox, preventing any atmospheric cooling. It is only after autumnal equinox, as convective precipitation rates start decreasing, that cooling radiative tendencies on temperatures are no longer balanced by latent heat release and dry energy loss (and cooling) occurs. In other words, it is only around this time that the latent energy loss is no longer capable of balancing the negative NEI and the dry energy loss is required to achieve energy balance. As discussed in more detail by Lobo and Bordoni (2020), this drop in temperature is accompanied by local condensation of moisture, with large-scale precipitation reaching its peak right after the maximum in latent energy loss.

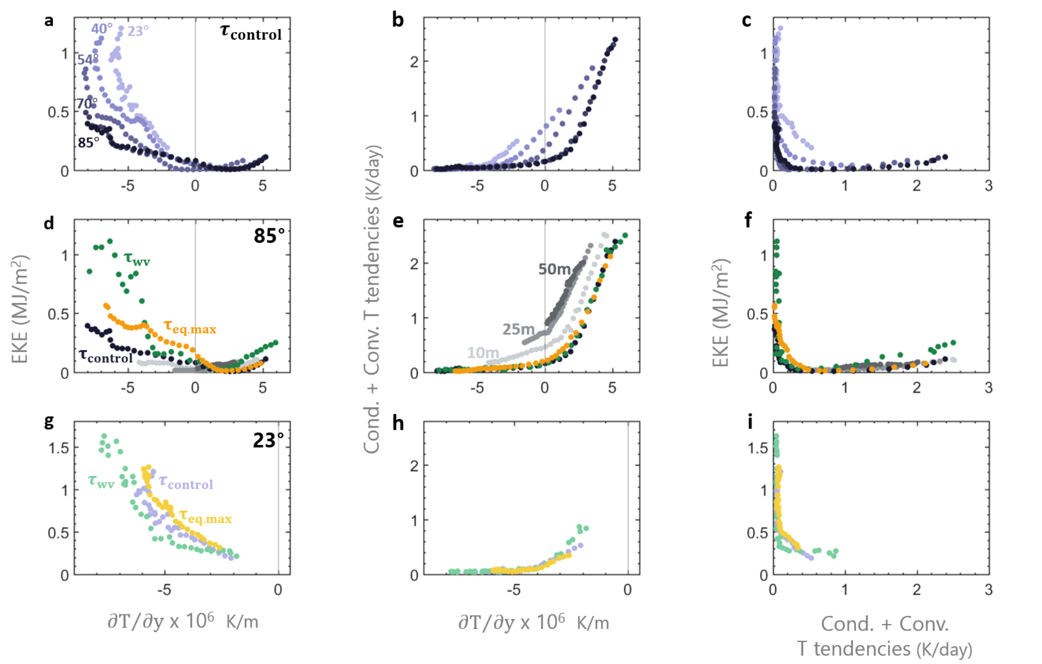

Figure 3.8: EKE averaged between 35° and 90° latitude, compared with average meridional temperature gradient (left). Condensation and convection temperature tendencies in the high latitudes compared to meridional temperature gradient (center). Comparison of EKE and temperature tendencies due to latent heat release (right). All measurements were vertically integrated, and plotted over the northern hemisphere winter (from pentad 37 to 71). The simulations used in each row are the same as in Fig. 3.9, but the dry simulations have been removed.

We can more directly examine the relationship between latent heat release and temperatures by exploring its contribution to temperature tendencies (Fig. 3.8). Temperature, in fact, changes due to various local energy sources and sinks, including shortwave and longwave radiative fluxes, diffusion, condensation, and convection. We group the latter two together and refer to them as $\partial T_{water}/\partial t$. While condensation or convection are occurring, latent heat is being released and there is a positive $\partial T_{water}/\partial t$ in the high latitudes (Fig. 3.8b). We can see that high values of $\partial T_{water}/\partial t$ in the high latitudes lead to low, or in some cases positive, meridional temperature gradients. In other words, the poles remain warm thanks to the latent heat release. By keeping temperature gradients small or negative, this results in weak baroclinic eddy activity. Then, once the water vapor is sufficiently depleted and the $\partial T_{water}/\partial t$ term tends to zero, we see a quick increase in negative temperature gradients and a sharp rise in EKE. In panel c, we directly compare $\partial T_{water}/\partial t$ to EKE, which showcases the clear shift that occurs as latent heat release due to water vapor condensation ceases and eddy activity grows.

3.5 Comparison with Dry Land Planets

To further illustrate the importance of moisture effects on the temperature patterns and circulation, we compare the control simulations to runs where the saturation vapor pressure is set to zero. These dry simulations, at both 23° and 85° obliquity, make it easier to visualize the distinction between the system's inertia and the moisture's buffering effect. As can be noted in Fig. 3.5, in the absence of moisture, the meridional temperature gradients reverse near equinox. Similarly, cooling rates are strongest approximately at equinox (Fig. 3.9), such that the atmospheric sensible energy loss maximizes roughly 50 days earlier than in the moist simulations.

By affecting the meridional temperature gradients, it is clear that moisture can play a strong role in determining eddy activity. But it is worth briefly considering other mechanisms through which moisture can affect eddies. Latent heat release reduces the atmosphere's effective static stability (Lapeyre and Held, 2004; Chang et al., 2002), such that dry models underestimate eddy activity by nearly an order of magnitude if mean fields are held constant (O'Gorman, 2011). Based on that alone, we would expect the moist simulations to have significantly higher EKE values. However, we see that for 85° obliquity the dry simulation has the largest values for EKE, as well as significantly longer duration of winter baroclinic eddy activity (Fig. 3.4). Even for the 23° case, the dry simulation has slightly larger EKE. This allows us to conclude that the buffering effect is dominant, such that the inclusion

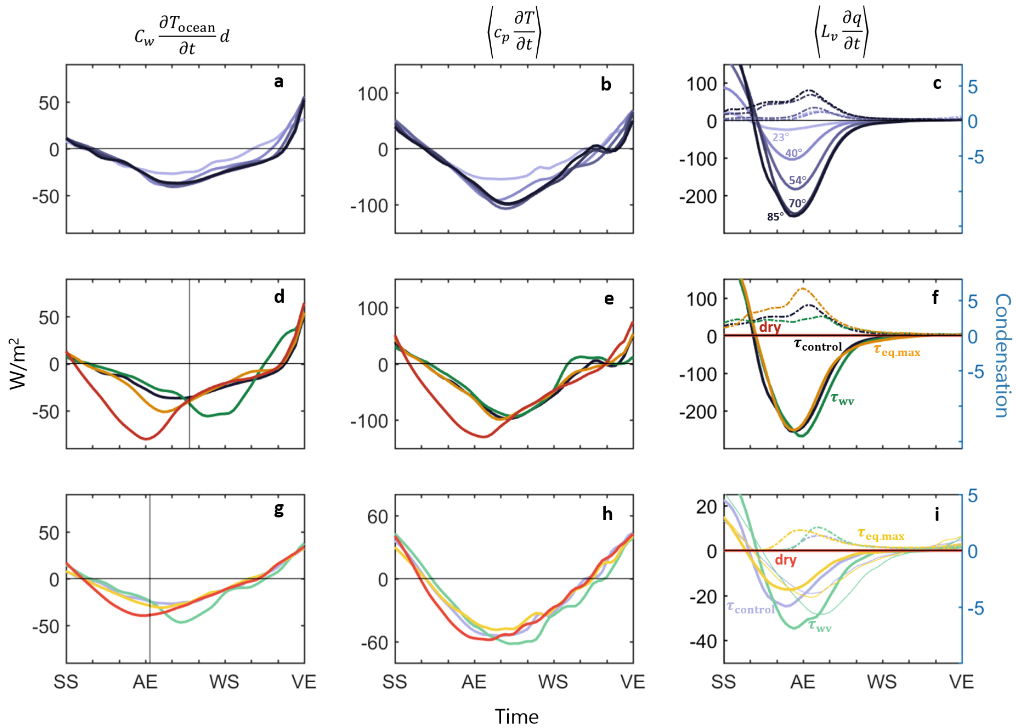

Figure 3.9: Depiction of atmospheric and ocean cooling during the NH winter. The rate at which the ocean mixed layer loses heat (left), as well as the change in atmospheric sensible heat (middle) and latent heat (right, solid lines) components are shown in terms of energy (W.m^{-2}). Values are vertically integrated and averaged between -60° and -90° latitude. Dash-dotted lines (right) show large-scale precipitation values (mm/day). The top row shows τ_{control} simulations, middle row includes all 85° simulations, and the bottom row shows 23° values. We use a 3 pentad simple rolling average to make the figure easier to read. The vertical lines in figures d and g show the time when the near-surface high latitude τ_{wv} optical depth drops below the τ_{control} value. The dotted lines in panel i show change in latent heat between -50 and -20° latitude. Note that C_w is the specific heat capacity of water, and d is the depth of the ocean mixed layer.

of atmospheric water is suppressing rather than enhancing winter baroclinic eddy activity.

As was previously noted, changes in eddy activity also impact the Ferrel cell and storm tracks. For 85° obliquity, the moisture's buffering effect leads to a 70 day delay in the formation of the winter Ferrel cell relative to the dry simulation (Fig. 3.10). Overall, the effects of atmospheric moisture storage on the climate bear many similarities to those of the surface heat capacity, which shall be discussed in Section 3.7. Both mechanisms slow warming during the summer, and increase the amount of heat that is available when there is a radiative deficit in the winter, keeping polar temperatures more moderate year-round. In both cases, this leads to a weakening, or to the absence of winter baroclinic eddy activity, storm tracks, and winter Ferrel cells.

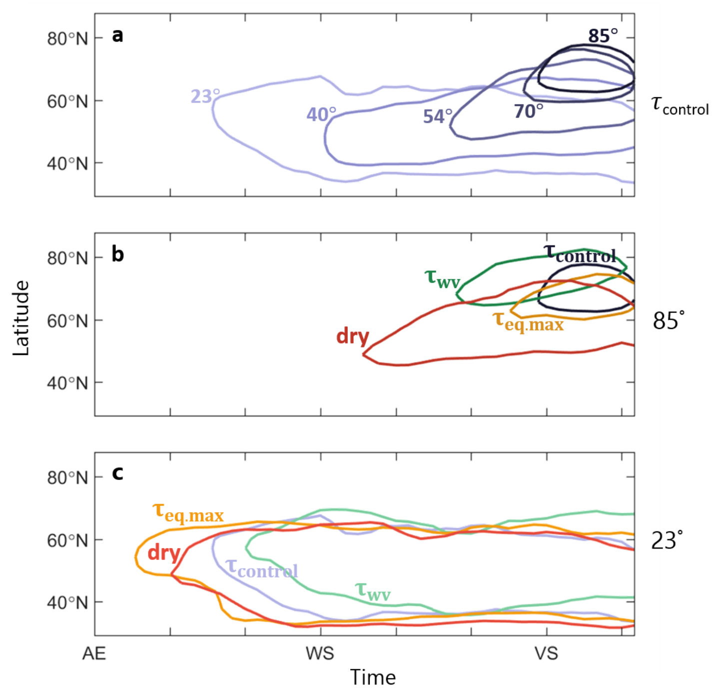

Figure 3.10: 5NH Ferrel cell activity shown over time. The cell edge is shown where the vertically integrated stream function surpasses 10^{10} kg/s in magnitude. Model colors match previous figures, with (a) showing $\tau_{control}$ simulations with various obliquities, (b) 85° simulations, and (c) 23° simulations. We apply the same 3 pentad averaging here to match previous figures.

Recap

To summarize the results so far, moisture influences the seasonal cycle of high obliquity planets through the following mechanisms:

1. During early summer, the increase of atmospheric moisture storage slows the rate of warming and reduces and delays temperature maxima.

2. At the end of summer, the negative net energy input is primarily balanced by latent energy loss, which delays the atmospheric cooling.

3. The latent energy loss (drying of the atmospheric column) occurs at times when vigorous convective precipitation exceeds evaporation. Significant high-latitude convective activity in high-obliquity simulations results from MSE maximazing at the summer poles.

4. As latent energy loss is no longer able to compensate for the increasingly negative NEI, temperatures start decreasing, which is accompanied by local large-scale condensation of atmospheric moisture. This further extends the high-latitude rainy season to one month after autumnal equinox.

5. The steps described above can be re-interpreted in terms of the positive temperature tendencies due to the diabatic heating associated with high-latitude precipitation. It is the latent heat released as moisture condenses out at times of latent energy loss that gives rise to positive temperature tendencies that counteract the radiatively driven cooling, slowing down polar cooling and impacting the meridional temperature patterns. For high obliquities these effects are sufficiently strong to keep the poles warmer than the low latitudes, preventing baroclinic eddy activity, the formation of storm tracks, and the winter Ferrel cell.

3.6 Dependence of Latent Heat Effects on Longwave Optical Depth

The intensity of longwave radiation emissions is not a prescribed model quantity and has a complex relationship with the circulation and temperature. However, we can examine the sensitivity of our results to changes in longwave radiation by using different optical depth examples, as described in Section 3.1. As was the case when we varied obliquity, these simulations were designed to redistribute energy without any net warming or cooling of the planet. In the low latitudes, these various simulations tend to produce qualitatively similar climates. There are some significant changes in overturning intensity and structure that can be noted in Fig. 3.1, but here we focus on the higher latitudes because relatively small changes in longwave optical depth have a strong impact on eddy activity. The EKE response to optical depth changes is similar in magnitude to the response to obliquity changes. For example, the EKE maximum for 23° τ_{control} is closer to 85° τ_{wv} than to 23° τ_{wv} values. Also, the delay in baroclinic activity in 23° τ_{wv} is comparable to the delay for 40° τ_{control}, which can also be noted in the Ferrel cell behavior in Fig. 3.10.

In simulations with latitudinally varying optical depth ($\tau_{\mathrm{eq.max}}$), the atmosphere is optically thicker (thinner) at the equator (pole). At high obliquity it results, as might be expected, in a cooler polar summer (Fig. 3.3) and also allows for slightly faster cooling during the fall (Fig. 3.9d). The polar moisture storage is reduced and the $\partial T_{\mathrm{water}}/\partial t$ has a lower maximum (Fig. 3.8). As we might expect, in these simulations high latitude eddies form more rapidly and achieve higher EKE values than the control simulation. This can be noted in Fig. 3.4 for both high and low obliquity cases. The changes in eddy activity are relatively subtle, but can also be noted in the slightly earlier Ferrel cell formation (Fig. 3.10b and c).

In the lower obliquity simulations, changes in mid and low latitude moisture storage may have an impact on the high latitude effects we are describing. The high latitude latent energy variations (solid lines, Fig. 3.9i) are weaker in low obliquity simulations, such that their magnitude is comparable with the midlatitude variations (dashed lines). The latent heat release in the midlatitudes occurs a few weeks later than at the poles, and would facilitate more negative temperature gradients during NH winter. Thus, for the 23° $\tau_{\mathrm{eq.max}}$ simulation where there is latent heat release in the midlatitudes, combined with a higher optical depth in the low latitudes, it is not surprising that the EKE values surpass those of the τ_{control} simulation (Fig. 3.4). Note that these midlatitude values are not shown in the remaining panels (c and f) because they are very small in comparison to the large polar latent terms of high obliquity simulations and would be difficult to visualize.

We also consider the effects of a water vapor feedback, which requires the optical depth to vary with time. During the summer in τ_{wv} simulations, temperature increases lead to increased evaporation, which increases the longwave optical depth, establishing a positive feedback. However, once temperatures begin to decrease in the winter and most of the water condenses out, the local optical depth can become lower than in τ_{control}, reducing the greenhouse effect. The time at which the near-surface τ_{wv} polar optical depth (at $\sim 75°$ latitude) drops below τ_{control} is indicated with a vertical grey line in Fig. 3.9 (f, i). The increased high latitude latent heat effects in τ_{wv} simulations, together with increased summer temperatures, hinders eddy formation in the early winter (Fig. 3.10c). But the accelerated polar cooling later in the season (Fig. 3.9) can facilitate stronger temperature gradients and stronger EKE maxima for τ_{wv} simulations (Fig. 3.4 & 3.8).

3.7 Land vs. Ocean Worlds: Effects of Varying Mixed Layer Depth

The effects of atmospheric moisture storage are in many ways similar to the seasonal effects of increased surface heat capacity. The model's prescribed ocean mixed layer depth determines the surface heat capacity, such that a deep mixed layer increases the capacity for local energy storage. Increasing the mixed layer depth from 1m to 50m increases the thermal inertia timescale from a day to 2 months (Lobo and Bordoni, 2020; Cronin and Emanuel, 2013), reducing the amplitude of seasonal variations in climate. To examine this effect, we compare high obliquity simulations with mixed layer depths of 1, 10, 25, and 50m.

In high obliquity simulations with a deep mixed layer, the poles remain warm year-round and the meridional temperature gradients in the northern hemisphere stay positive most (10m and 25m) or all of the year (50m). Increasing the mixed layer depth leads to behavior increasingly similar to that of simulations forced with annual mean insolation (Fig. 3.3). However, this does not mean that the atmospheric moisture storage is absent. Fig. 3.11 shows that an increase in mixed layer depth leads to a reduction in all moisture budget terms. But the moisture storage remains an important part of the budget even in the 50m case, helping to shape the net precipitation patterns.

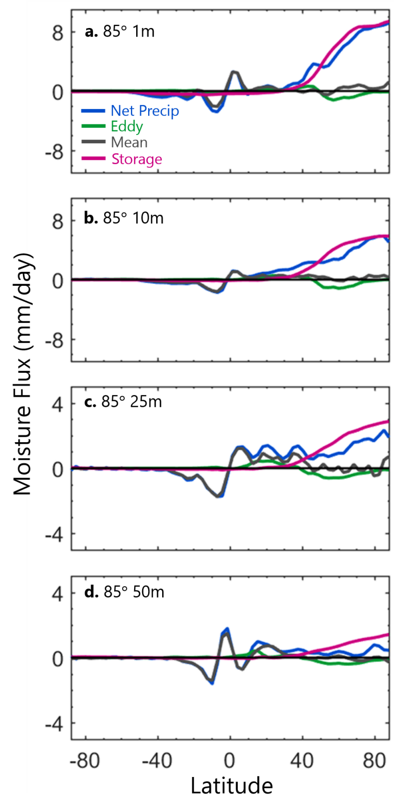

Figure 3.11: Moisture budget decomposition at NH autumnal equinox showcasing northern hemisphere atmospheric moisture storage for high obliquity (85° τ_{control}) simulations with increasing mixed layer depths. Net precipitation, shown in blue, is balanced by mean moisture flux convergence ($-\nabla\cdot <\overline{\mathbf{u}}\overline{q}>$) shown in gray, eddy moisture flux convergence ($-\nabla\cdot <\mathbf{u}'q'>$) shown in green, and moisture storage ($-\partial_t <q>$) shown in pink.

Increasing the mixed layer depth not only weakens the Hadley cell, but also reduces its extent, and results in a more prominent equatorial jump. Strong virtual temperature gradients are necessary for the meridional flow in the boundary layer to cross the equator (Pauluis, 2004), where the Coriolis parameter is negligible. As discussed in Lobo and Bordoni (2020), the high obliquity simulations with 1m mixed layer depth have negative near-surface equatorial temperature gradients during the spring and fall (Fig. 3.12). This prevents the poleward flow and creates low-level convergence (orange contours, Fig. 3.12). The flow is forced to rise above the boundary layer, crossing the equator in the free troposphere. This also results in condensation and an equatorial secondary precipitation maximum which is present in the spring and fall.

During the remainder of the year, there are still inflection points in the near-surface temperature gradients, that could cause low-level convergence. But the equatorial atmospheric moisture values are low (Fig. 3.12), such that without significant latent heat release during the ascent, the jump becomes shallow and there is no notable secondary precipitation maxima during solstices.

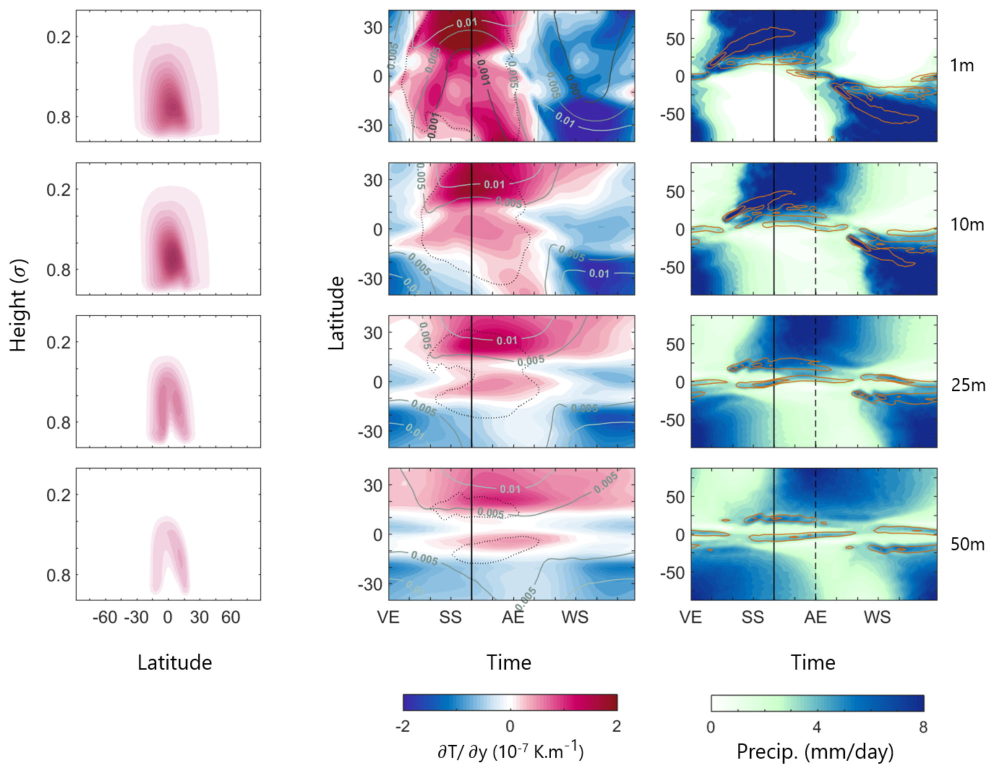

Figure 3.12: Atmospheric response to changes in mixed layer depth for 85° simulations, with mixed layer depths of 1, 10, 25, and 50m shown from top to bottom. Left column shows Hadley cell structure during late summer (pentad 30, at the time indicated by black line in other plots). Color contours show the counter-clockwise winter Hadley cell, with intervals of 5×10^{10} kg s^{-1}. The center column color contours show meridional temperature gradients in the low latitudes. The black contours indicate where near surface streamfunction values rise above 10^{10} kg s^{-1}, roughly outlining the winter cell during the NH summer. Yellow contours show near-surface atmospheric moisture values (kg/kg). The right column shows precipitation values throughout the year (in mm/day) with orange contours indcating regions of strong near surface convergence, defined as $\partial v/\partial y$ surpassing -5×10^{-8}.

However, with a deeper mixed layer, there is a clear temperature gradient reversal near the equator that sustains strong low-level convergence throughout most of the year. Also, moisture values are subject to less fluctuation and near-surface equatorial water vapor content remains relatively high year-round. This results in a strong equatorial jump and long-lasting equatorial precipitation maxima, with magnitude at times rivaling the ITCZ precipitation values.

The energy budget for simulations with moderate mixed layer depths (10 and 25m) are mildly influenced by atmospheric latent heat release (Fig. 3.8e). But the heat exchanges with the surface dominate the atmospheric energy budget. The surface heat loss during the winter in these deep mixed layer simulations is shown in Fig. 3.13. The results from the energy budget largely agree with the behavior observed in coupled atmosphere-ocean simulations (Ferreira et al., 2014), where the reduction in winter eddy activity at high obliquity was linked to changes in surface temperature gradients. While ocean heat transport played a role in the coupled simulations, the dominant effect was determined to be local ocean heat uptake, which absorbed energy during summer and warmed the atmosphere from below during winter.

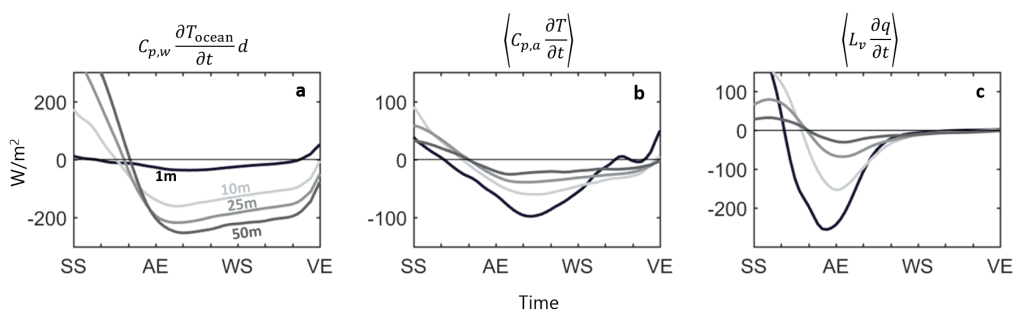

Figure 3.13: Atmospheric and surface cooling rates, as in Fig. 3.9, for 85° simulations with mixed layer depths of 1, 10, 25, and 50m.

The aquaplanet simulations suggest that in Earth-like planets, with a global ocean and a deep mixed layer, the ocean heat storage would control the energy budget and could keep the poles warm enough to weaken or even prevent baroclinic eddy activity. However, it is important to note that the 50m mixed layer depth also results in a weak seasonal cycle and a weak atmospheric circulation (Fig. 3.12), which implies a weakening of the very wind stress and seasonal buoyancy forcings that help sustain a deep mixed layer. Therefore, additional future studies with coupled atmospheric and ocean models will be valuable for constraining plausible planetary ocean configurations.

3.8 Seasonal Cycle vs Annual Mean Simulations

High obliquity planets have a stronger seasonal cycle of insolation than their low obliquity counterparts, especially in a planet without an active ocean, whose surface has a low heat capacity like the one modeled in Chapter 1.1. This results in more extreme temperatures and strong seasonal phenomena that are of leading order and yet are not captured in a model forced with annual mean insolation.

While this may appear to be an obvious statement, it merits emphasis in the field of planetary sciences. As we work towards coarse characterizations of planetary climates of more distant planetary bodies, for which we have limited data, it may be tempting to focus exclusively on annual mean conditions. And yet, this may hide seasonal atmospheric responses that fundamentally shape the planetary climate.

Simple energy balance considerations already provide clues on how ignoring seasonally varying insolation might introduce nonnegligible errors in the estimate of the meridional distribution of the annual mean surface temperature. If we assume the planet behaves as a blackbody, energy balance requires the absorbed shortwave radiation be balanced by the outgoing longwave radiation as $S = \sigma T^4$. Because the outgoing longwave is a strongly nonlinear function of temperature, it is clear that the annual mean surface temperature at each latitude in response to annual mean forcing will be different from the one obtained by annually averaging the response to seasonally varying forcing, with differences in the two increasing as seasonal variations increase.

We have in fact conducted simulations where insolation is kept at its annual mean value. Differences in the meridional distribution of the annual mean temperature with and without a seasonal cycle of insolation are shown in Fig. 3.14 for the 23.5° and 85° obliquity cases (with 1m mixed layer depth). Notice how temperatures in the annual mean simulations are not only higher, but also feature higher pole-to-equator temperature contrast.

The discussion in the previous sections also makes clear how the planetary climate is dominated by seasonally varying phenomena that are not captured in simulations with annual mean forcing, first and foremost the Hadley circu-

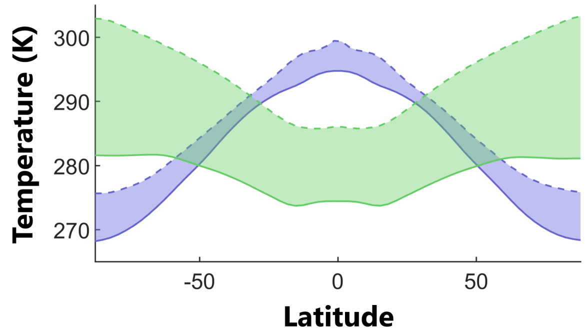

Figure 3.14: Annual-mean surface temperatures in 23.5°(blue) and 85°(green) obliquity simulations, with $\tau_{control}$. Results obtained with seasonally varying insolation are plotted with a solid line, while those resulting from annual-mean forcing are shown with a dashed line, and the difference between the two is shaded.

lation. In fact, as obliquity increases and the pole-to-equator insolation (and temperature) gradient in the annual mean reverses (Fig. 1.1 and 3.14), the Hadley cells reverse, with rising motions in the subtropics and descending motion at the equator (not shown). While overturning in a direction opposite to the one seen at Earth's obliquities, these cells are still thermally direct cells, with air in the warmer subtropics rising and air in the colder equator sinking. However, when a seasonal cycle is resolved, the annually averaged overturning (and associated energy transport) is inconsequential, as the atmospheric circulation is dominated by seasonally-reversing, strong and broad cross-equatorial Hadley circulations. These circulations effect significant energy transport from the warm summer hemisphere to the cold winter hemisphere, leading to a much smaller annual mean pole-to-equator temperature gradient than what is seen in the annual mean simulation (Fig. 3.14). Other seasonal phenomena that are not captured in annual-mean simulations pertain to the hydrological cycle in polar regions, where seasonal storage effects are nonnegligible at high obliquities.

In summary, for a high obliquity planet with moderate-to-low surface heat capacity (and thus, strong seasonal cycles), modeling the atmospheric behavior without the seasonal cycle is not only a matter of oversimplification, but could result in errors that would make climate characterizations and habitability considerations unreliable.

3.9 Discussion of Extratropical Dynamics

On planets with a strong seasonal cycle, atmospheric energy storage can significantly impact the energy budget. The latent component of the energy storage tends to reduce and delay summer temperature maxima, and at the end of summer it helps keep the high latitudes warm relative to the low latitudes. This effectively prolongs the summer season and reduces the duration and intensity of winter at the poles. The reduction in meridional temperature gradients also leads to weakening or even prevention of winter baroclinic eddy activity.

The absence of eddies limits the high latitude meridional energy transport in high obliquity simulations. In their stead, limited thermally direct transport can occur beyond what we would consider to be the Hadley cell edge, though the cell edge also becomes less clearly defined for high obliquity planets (see Lobo and Bordoni, 2020). It is only when polar temperatures drop significantly, after the latent energy has been depleted, that an organized Ferrel cell is able to take shape and transport energy poleward. As is the case on Earth, a thermally indirect mean flow also develops, transporting some energy equatorward. The balance of these fluxes results in modest values of net poleward energy transport.

Though it is not clear how many rocky planets will have surface water, any such planets would be immensely appealing targets for habitability studies, given that water is a minimum requirement for life as we know it. As we have shown, the presence of moisture on Earth-like planets can have a significant effect on the atmospheric circulation, its response to changes in radiation, and the resulting surface climate. This work, combined with previous studies of lower latitude features (Lobo and Bordoni, 2020), highlights the importance of accounting for latent heat effects in simulations of Earth-like planets.

The use of a slab ocean allows us to focus on the atmospheric circulation, and a shallow mixed layer emphasizes seasonal behavior, allowing us to isolate various mechanisms controlling the atmospheric circulation. While it is not representative of Earth's ocean covered surfaces, this setup is both a valuable theoretical tool and potentially a useful representation of land planets. Land planets could have wider habitable zones than ocean worlds (Abe et al., 2011; Kodama et al., 2018, 2019), making them attractive targets for further work. In particular, land planets are thought to have higher runaway greenhouse thresholds if the surface water were concentrated poleward of the Hadley cell edge (Kodama et al., 2018). We expect that the atmospheric moisture storage effects discussed in this work could be particularly relevant for planets with such surface water configurations.

On planets with abundant surface liquid water (ocean worlds), we might expect to see expansive and deep Earth-like oceans that would dampen the seasonal cycle. But little is known regarding the existence of ocean-covered terrestrial exoplanets or their ocean properties. Many factors, including salinity, could significantly affect the ocean's mixed layer depth and thus its ability to store heat locally (Olson et al., 2020). Until further constraints can be placed, it will be important to systematically consider planetary configurations ranging from those with climates primarily controlled by atmospheric transport and storage to those controlled by the ocean.

We have mostly contrasted the effects of atmospheric moisture storage and surface heat capacity on the meridional temperature gradients. But it is worth noting that their combined effects suggest that temperate and moist high obliquity planets, including both ocean worlds and land planets, will likely have weak baroclinicity. It is possible that planet-specific properties such as clouds, surface albedo, and topography could alter these results. For example, an anomalously low polar optical depth could, as we have shown, facilitate seasonal temperature gradient reversals. But in the absence of large meridional gradients in these planetary properties, if the surface has sufficiently high heat capacity, it will keep the poles warm year-round. In cases where the surface has a low heat capacity, the latent component of the atmospheric energy storage can also help keep the poles warm during fall and early winter. Thus, for high obliquity planets, pole-to-equator temperature gradients are generally weaker in winter, and we would not expect strong winter Ferrel cells or storm tracks regardless of mixed layer depth.

Strong latent heat effects during seasonal transitions can complicate our understanding of planetary thermal inertia. Previous studies have attempted to relate planetary thermal inertia to changes in light curves of terrestrial exoplanets (e.g. Cowan et al., 2012; Gaidos and Williams, 2004). However, significant atmospheric latent heat effects, such as those in our high obliquity simulations, could shift planetary emissions, delaying temperature maxima and minima for the high latitudes. Thus, depending on the viewing geometry, the atmospheric moisture storage could make it even more challenging to determine surface properties and distinguish delays due to latent heat effects from those due to high surface heat capacity. Also, while water is of particular interest for habitable planets, the mechanisms described here could be relevant for a broader range of planets with other atmospheric constituents that undergo phase changes.

References

Y. Abe, A. Abe-Ouchi, N. H. Sleep, and K. J. Zahnle. Habitable zone limits for dry planets. *Astrobiology*, 11(5):443–460, jun 2011. ISSN 1531-1074. doi:10.1089/ast.2010.0545.

E. K. Chang, S. Lee, and K. L. Swanson. Storm track dynamics. *Journal of Climate*, 15(16):2163–2183, 2002. ISSN 08948755. doi:10.1175/1520-0442(2002)015<02163:STD>2.0.CO;2.

N. B. Cowan, A. Voigt, and D. S. Abbot. Thermal phases of earth-like planets: Estimating thermal inertia from eccentricity, obliquity, and diurnal forcing. *Astrophysical Journal*, 757(1), 2012. ISSN 15384357. doi:10.1088/0004-637X/757/1/80.

T. W. Cronin and K. A. Emanuel. The climate time scale in the approach to radiative-convective equilibrium. *Journal of Advances in Modeling Earth Systems*, 5(4):843–849, 2013. doi:10.1002/jame.20049.

S. Faulk, J. Mitchell, S. Bordoni, S. Faulk, J. Mitchell, and S. Bordoni. Effects of rotation rate and seasonal forcing on the ITCZ extent in planetary atmospheres. *Journal of the Atmospheric Sciences*, pages JAS–D–16–0014.1, 2017. ISSN 0022-4928. doi:10.1175/JAS-D-16-0014.1.

N. Feldl, S. Bordoni, and T. M. Merlis. Coupled high-latitude climate feedbacks and their impact on atmospheric heat transport. *Journal of Climate*, 30(1):189–201, 2017. ISSN 08948755. doi:10.1175/JCLI-D-16-0324.1.

D. Ferreira, J. Marshall, P. A. O'Gorman, and S. Seager. Climate at high-obliquity. *Icarus*, 243:236–248, 2014. ISSN 10902643. doi:10.1016/j.icarus.2014.09.015.

D. M. W. Frierson, I. M. Held, and P. Zurita-Gotor. A gray-radiation aquaplanet moist GCM. Part II: Energy transports in altered climates. *Journal of the Atmospheric Sciences*, 64(5):1680–1693, 2007. ISSN 0022-4928. doi:10.1175/JAS3913.1.

E. Gaidos and D. M. Williams. Seasonality on terrestrial extrasolar planets: Inferring obliquity and surface conditions from infrared light curves. *New Astronomy*, 10(1):67–77, 2004. ISSN 13841076. doi:10.1016/j.newast.2004.04.009.

I. Guendelman and Y. Kaspi. An axisymmetric limit for the width of the hadley cell on planets with large obliquity and long seasonality. *Geophysical Research Letters*, 45(24):13,213–13,221, 2018. ISSN 19448007. doi:10.1029/2018GL080752.

I. Guendelman and Y. Kaspi. Atmospheric dynamics on terrestrial planets: The seasonal response to changes in orbital, rotational, and radiative timescales. *The Astrophysical Journal*, 881(1):67, 2019. ISSN 1538-4357. doi:10.3847/1538-4357/ab2a06.

I. M. Held. The partitioning of the poleward energy transport between the tropical ocean and atmosphere. *Journal of the Atmospheric Sciences*, 58(8):943–948, 2001. ISSN 00224928. doi:10.1175/1520-0469(2001)058<0943:TPOTPE>2.0.CO;2.

I. M. Held and A. Y. Hou. Nonlinear axially symmetric circulations in a nearly inviscid atmosphere. *Journal of the Atmospheric Sciences*, 37:515–533, mar 1980. ISSN 0022-4928. doi:10.1175/1520-0469(1980)037<0515:NASCIA>2.0.CO;2.

I. M. Held and B. J. Soden. Water vapor feedback and global warming. *Annual Review of Energy and the Environment*, 25(1):441–475, nov 2000. ISSN 1056-3466. doi:10.1146/annurev.energy.25.1.441.

S. A. Hill, S. Bordoni, and J. L. Mitchell. Axisymmetric constraints on cross-equatorial Hadley cell extent. *Journal of the Atmospheric Sciences*, 76(6): 1547–1564, 2019. ISSN 15200469. doi:10.1175/JAS-D-18-0306.1.

Y. Kaspi and A. P. Showman. Atmospheric Dynamics of Terrestrial Exoplanets over a Wide Range of Orbital and Atmospheric Parameters. *The Astrophysical Journal*, 804(1):60, 2015. doi:10.1088/0004-637X/804/1/60.

T. Kodama, A. Nitta, H. Genda, Y. Takao, R. O'ishi, A. Abe-Ouchi, and Y. Abe. Dependence of the onset of the runaway greenhouse effect on the latitudinal surface water distribution of earth-like planets. *Journal of Geophysical Research: Planets*, 123(2):559–574, 2018. ISSN 21699100. doi:10.1002/2017JE005383.

T. Kodama, H. Genda, R. O'ishi, A. Abe-Ouchi, and Y. Abe. Inner edge of habitable zones for earth-sized planets with various surface water distributions. *Journal of Geophysical Research: Planets*, 124(8):2306–2324, 2019. ISSN 21699100. doi:10.1029/2019JE006037.

G. Lapeyre and I. M. Held. The role of moisture in the dynamics and energetics of turbulent baroclinic eddies. *Journal of the Atmospheric Sciences*, 61(14):1693–1710, 2004. ISSN 00224928. doi:10.1175/1520-0469(2004)061<1693:TROMIT>2.0.CO;2.

R. S. Lindzen and A. V. Hou. Hadley circulations for zonally averaged heating centered off the equator. *Journal of the Atmospheric Sciences*, 45(17):2416–2427, 1988. ISSN 0022-4928. doi:10.1175/1520-0469(1988)045<2416:HCFZAH>2.0.CO;2.

A. H. Lobo and S. Bordoni. Atmospheric dynamics in high obliquity planets. *Icarus*, 340(November 2019):113592, 2020. ISSN 10902643. doi:10.1016/j.icarus.2019.113592.

T. M. Merlis and T. Schneider. Atmospheric dynamics of earth-like tidally locked aquaplanets. *J. Adv. Model. Earth Syst.*, 2(4):1–17, 2010. ISSN 1942-2466. doi:10.3894/JAMES.2010.2.13.

J. L. Mitchell, R. T. Pierrehumbert, D. M. Frierson, and R. Caballero. The impact of methane thermodynamics on seasonal convection and circulation in a model Titan atmosphere. *Icarus*, 203(1):250–264, 2009. ISSN 00191035. doi:10.1016/j.icarus.2009.03.043.

J. D. Neelin. Moist dynamics of tropical convection zones in monsoons, teleconnections and global warming. In T. Schneider; A. H. Sobel., editor, *The Global Circulation of the Atmosphere*, pages 267–301. Princeton University Press, 2007.

J. D. Neelin and I. M. Held. Modeling tropical convergence based on the moist static energy budget. *Monthly Weather Review*, 115(1):3–12, jan 1987. ISSN 0027-0644. doi:10.1175/1520-0493(1987)115<0003:MTCBOT>2.0.CO;2.

P. A. O'Gorman. The effective static stability experienced by eddies in a moist atmosphere. *Journal of the Atmospheric Sciences*, 68(1):75–90, 2011. ISSN 00224928. doi:10.1175/2010JAS3537.1.

P. A. O'Gorman and T. Schneider. The hydrological cycle over a wide range of climates simulated with an idealized gcm. *Journal of Climate*, 21:3815–3832, 2008. ISSN 0894-8755, 1520-0442. doi:10.1175/2007JCLI2065.1.

S. L. Olson, M. Jansen, and D. S. Abbot. Oceanographic considerations for exoplanet life detection. *The Astrophysical Journal*, 895(1):19, 2020. ISSN 1538-4357. doi:10.3847/1538-4357/ab88c9.

O. Pauluis. Boundary layer dynamics and cross-equatorial hadley circulation. *Journal of the Atmospheric Sciences*, 61(10):1161–1173, 2004. doi:10.1175/1520-0469(2004)061<1161:BLDACH>2.0.CO;2.

J. P. Peixoto and A. H. Oort. *Physics of Climate*. New York, NY (United States); American Institute of Physics, United States, 1992. URL https://www.osti.gov/biblio/7287064.

S. Pfahl, P. A. O'Gorman, and M. S. Singh. Extratropical cyclones in idealized simulations of changed climates. *Journal of Climate*, 28(23):9373–9392, 2015. ISSN 08948755. doi:10.1175/JCLI-D-14-00816.1.

T. Schneider and C. C. Walker. Self-organization of atmospheric macroturbulence into critical states of weak nonlinear eddy-eddy interactions. *Journal of the Atmospheric Sciences*, 63(6):1569–1586, 2006. ISSN 00224928. doi:10.1175/JAS3699.1.

A. P. Showman, R. D. Wordsworth, T. M. Merlis, and Y. Kaspi. Atmospheric Circulation of Terrestrial Exoplanets. In *Comparative Climatology of Terrestrial Planets*. University of Arizona Press, 2013. doi:10.2458/azu_uapress_9780816530595-ch12.

E. T. Wolf, A. L. Shields, R. K. Kopparapu, J. Haqq-Misra, and O. B. Toon. Constraints on climate and habitability for earth-like exoplanets determined from a general circulation model. *The Astrophysical Journal*, 837(2):107, 2017. ISSN 1538-4357. doi:10.3847/1538-4357/aa5ffc.

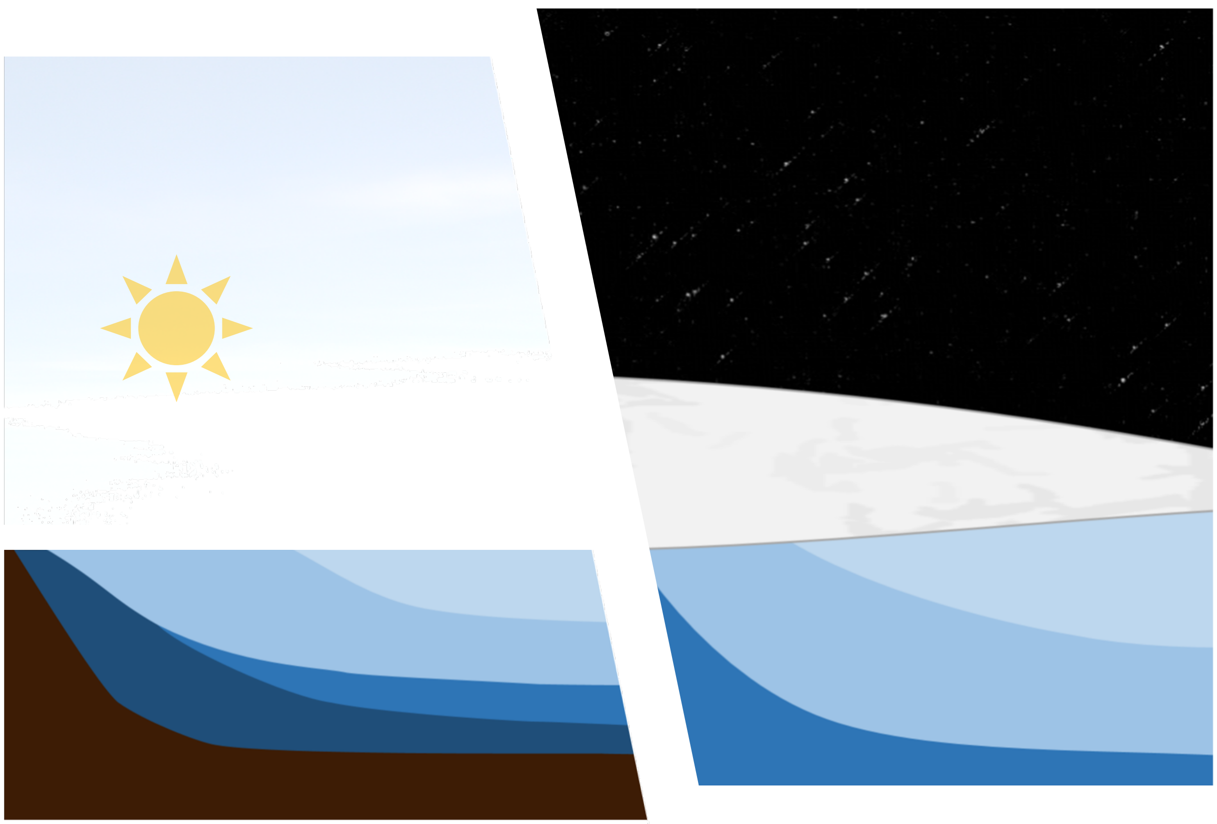

Chapter 4

ICY WORLDS OCEAN MODEL

Liquid water oceans within our solar system provide intriguing laboratories for the coupled interaction between physical, chemical, and biological processes needed to support life. They challenge pre-existing definitions of the "habitable zone," demonstrating that large liquid water reservoirs are not only possible in the outer regions of the solar system, but that they might even be common. It is no surprise that there is growing interest in icy worlds. However, the idea that many of the solar system's distant moons could have subsurface oceans is not entirely new. Early theoretical studies were underway even before the Voyager mission and later received significant support from geodesic, geological (Carr et al., 1998, for Europa), and magnetic (Zimmer et al., 2000, for Europa and Callisto) data collected by the Galileo spacecraft, as summarized in the Nimmo and Pappalardo (2016) review. Yet, despite this relatively long history and the recent surge in attention, we still know very little about the structure and circulation of these hidden oceans.

Many studies of icy world ice shells have treated the oceans as well-mixed, homogeneous, and static boundaries. However, the inhomogeneities in both the interior and surface of the ice shell suggest a more complex picture. In particular, the nonuniformity of the heat flux through the shell (Čadek et al., 2019), and the chaos terrains near the equator of Europa (Soderlund et al., 2014) are likely linked to the underlying ocean circulation.

Soderlund et al. (2014) modeled the thermally-driven ocean circulation in a vertically homogeneous ocean across a variety of configurations. They showed that for Europa-like oceans, a two-cell structure develops with upwelling at the low latitudes, thus concentrating the delivery of geothermal heat to the equatorial ice shell. However, those simulations did not take into account variations in the ocean's density distribution. Given that these icy world oceans are expected to have significant salinity (e.g. Postberg et al., 2009), ocean-ice interactions that include phase changes (Lobo et al., 2021), and depths at least an order of magnitude greater than Earth's oceans (e.g. Beuthe et al., 2016), exploring the role of vertical structure and density variations is a crucial next step.

Earth's Southern Ocean provides an example of how density variations linked to ocean-ice interactions can help drive a meridional overturning circulation. Antarctic bottom water forms as a result of heat loss to the atmosphere and brine rejection from ice formation. This high density water causes downwelling in the polar region and an equatorward abyssal flow. Diabatic mixing allows the water to rise to mid-depths, where the flow becomes poleward and largely adiabatic, eventually outcropping back in the Southern Ocean, closing the overturning loop (Marshall and Speer, 2012; Lumpkin and Speer, 2007).

There are, of course, significant differences between icy worlds and Earth's oceans. Earth's oceans are predominantly heated by the absorption of shortwave radiation at the surface, which produces a strongly stratified system. In contrast, icy worlds are expected to have significant heating at their base (mantle-ocean boundary) due to tidal heating (Choblet et al., 2017), which may promote a weaker stratification. Though, the exact distribution of tidal heating between the upper and lower ocean boundaries is still subject to some debate. Earth's ocean circulation is partially driven by surface winds and other interactions with the atmosphere, which are absent in icy worlds. Instead, the ice shells, which are significant geodynamic entities unto themselves, can assume an important role at the upper ocean boundary and can help shape the ocean circulation. For example, friction between the ocean and ice shell could play a similar role in transmitting momentum fluxes as a surface wind stress. Also, as we shall discuss (Section 4.2), variations in the ice shell thicknesses, which were recently inferred from Cassini observations for Enceladus and Titan, can lead to ice transport and result in equator-to-pole buoyancy differences in the ocean. In other words, despite their exotic appearance, icy world oceans such as those on Enceladus, Europa, and Titan and their subsequent heat and salt distributions are likely to be, much like Earth's oceans, controlled by processes occurring at the ocean boundaries.

In this chapter, we introduce an idealized ocean model inspired by the residual circulation framework used to study the Southern Ocean. This model seeks to identify the primary dynamical balances that govern the ocean circulation on icy worlds. Because this model is very idealized, it allows us to examine a broad range of parameter space, explore many of the possible circulation configurations, and provide guidance for future studies using more computationally intensive general circulation models. Results specific to Enceladus are discussed in Chapter 5.

4.1 The Basic Equations

In this section, we describe the governing equations of the spherical, zonally averaged, idealized overturning model. We begin with buoyancy conservation. Buoyancy is linearly related to density ρ through the relationship,

$$b = g\left(\frac{\rho_0 - \rho}{\rho_0}\right), \tag{4.1}$$

where ρ_0 is a reference density. The use of buoyancy emphasizes that differences in density constrain the overturning circulation as opposed to the absolute density.

Conservation of buoyancy is given by:

$$\frac{Db}{Dt} = -\nabla \cdot \mathbf{F_b} \approx -\frac{\partial F_b}{\partial z}, \tag{4.2}$$

where $\mathbf{F_b}$ is the buoyancy flux. We apply the assumptions that the buoyancy flux at the ocean-ice interface decays to zero over the depth of the mixed layer, such that water mass transformation due to ocean-ice interactions is confined to this layer, and the vertical divergence of the vertical flux dominates $\nabla \cdot \mathbf{F_b}$ (right-hand side of Eq. 4.2). The buoyancy flux varies with latitude and our sign convention is that $F_b(z = 0) > 0$ produces more buoyant (lighter) water and $F_b(z = 0) < 0$ produces less buoyant (denser) water. Expanding the material derivative, and applying a parameterization for the turbulent buoyancy flux in the ocean interior (discussed below), gives:

$$\begin{aligned} \frac{\partial b}{\partial t} &= -\mathbf{u} \cdot \nabla b - \nabla \cdot \mathbf{F_b} \qquad (4.3) \\ &\approx \underbrace{-v\frac{\partial b}{\partial y} - w\frac{\partial b}{\partial z}}_{\text{advection}} + \underbrace{\frac{\partial}{\partial z}\left(\kappa \frac{\partial b}{\partial z}\right)}_{\substack{\text{interior} \\ \text{mixing}}} - \underbrace{\frac{\partial F_b}{\partial z}}_{\substack{\text{buoyancy} \\ \text{flux at} \\ \text{surface}}} . \end{aligned}$$

In steady state, $\partial b/\partial t = 0$ such that both adiabatic advection and diabatic mixing in the ocean interior are balanced by transformation at the ocean-ice interface. In other words, volume is conserved in each layer at steady state.

The flow, represented by v and w, is the total ocean circulation comprising both mean and eddy components, for example $v = \overline{v} + v'$. The total flow is more commonly referred to as the residual circulation in the oceanographic literature on water mass transformation due to the tendency for mean and eddy components to cancel in certain regions of the terrestrial ocean (Groeskamp et al., 2019).

Residual Framework

For Earth's Southern Ocean, it is well documented that the overturning circulation cannot be understood simply by accounting for the Eulerian mean flow. In fact, in certain energetic regions, eddies can be strong enough to nearly cancel out the mean flow. Thus, it is useful to define the flow resulting from both mean and eddy components as the *residual* flow. The residual flow, or rather net flow, is defined as:

$$\Psi_{res} = \overline{\Psi} + \Psi' \tag{4.4}$$

where $\overline{\Psi}$ is the Eulerian mean streamfunction and Ψ' is the streamfunction associated with eddy activity, defined such that

$$\Psi' = -\frac{\overline{w'b'}}{\overline{b}_y}. \tag{4.5}$$

Similarly, we have:

$$v_{res} = \overline{v} + v', \quad \text{where} \quad \overline{v} = -\partial_z \overline{\Psi} \quad \text{and} \quad v' = -\partial_z \Psi'. \tag{4.6}$$

Assuming the upper part of Enceladus' ocean is zonally unbounded, the mean meridional velocity is weak and the meridional transport is dominated by eddy fluxes, e.g. $\overline{v'b'}$ and $\overline{w'b'}$. The mean meridional velocity, $\overline{v}$, vanishes in the absence of frictional forces because, assuming a small Rossby number, there is no zonally-averaged zonal pressure gradient to support this flow.

We parameterize the eddy transport using a well-tested closure from the oceanographic literature (Gent and McWilliams, 1990), in which the adiabatic component of the advection arises from the relationship

$$\Psi_{\text{adiabatic}} = K_{\text{e}} s L, \tag{4.7}$$

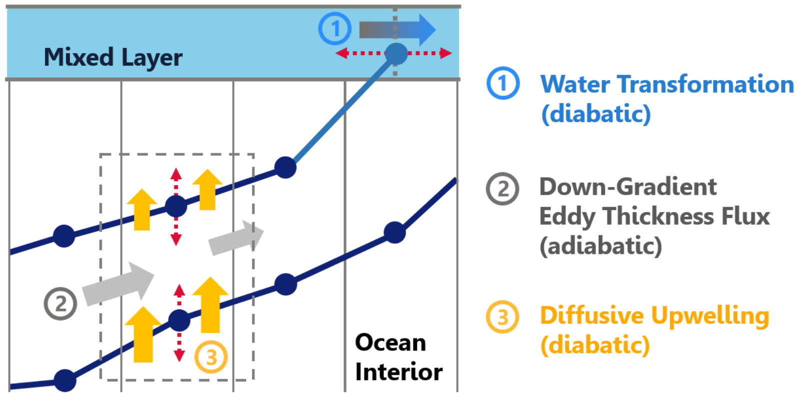

Figure 4.1: Diagram of how physical processes are represented within the model grid. The dark blue dots indicate the depth of each layer that evolves with time. The position where the interface outcrops at the ocean-ice boundary (light blue dot) also evolves in time, independent of the grid. This figure is not drawn to scale.

such that $v = -\partial\Psi/\partial z$ and $w = \partial\Psi/\partial y$. Here $s(y)$ is the slope of the interface separating density layers, $L(y)$ is the zonal length of each latitude circle, Ψ is a streamfunction quantifying a volume transport, and K_e is an isopycnal eddy diffusivity (m^2 s^{-1}). The eddy advection is assumed to act along density surfaces so that v and w combine to be parallel to the layer interfaces. Because the resulting flow is occurring within density layers, not involving mixing between different water classes, it is adiabatic in nature. In our model results, this flow can be thought of as a lateral flow, though it is technically parallel to isopycnals and not necessarily parallel to lines of constant depth or pressure. Note that while the slope of the density layers determines the intensity of the mesoscale eddies, the eddies act to transport tracers down large-scale gradients, such that a net volume transport is only possible when a layer-thickness gradient is present. If density layers are parallel (constant layer thickness), there remains an active eddy field, but there is no net volume transport. We set K_e to an Earth-like value (1000 m^2 s^{-1}) for the control simulation, and we test the sensitivity of the circulation to changes in K_e.

An important assumption in these simulations is that K_e is uniform throughout the ocean. Mixing length theory is often employed to argue that the eddy diffusivity, which is caused predominantly by mesoscale eddies, scales as $K_e \sim U\ell$, which depends on both the strength of the eddy velocities U and the size of the eddy ℓ (Vallis, 2006). We can approximate the eddy mixing length as the Rossby deformation radius $R = NH\pi^{-1}f^{-1}$. Here, f is the Coriolis parameter ($f = 2\Omega\sin\phi$) and $N^2 = \partial b/\partial z$. If we use $N^2 \approx \Delta B/H$, where H is the total ocean depth (30 km) and ΔB is the buoyancy difference between the lightest and densest layers, we would have $R = 10$ km in the midlatitudes. If we instead calculate N based on our model output and use our deepest layer as a measure of the pycnocline, such that we can set H to that layer's depth, this results in $R = 3$ km (at 45° latitude). Given that the total distance between the equator and pole on Enceladus is 395 km, this deformation radius provides reasonable support for a scale separation between the eddy and domain sizes, consistent with requirements for defining an eddy diffusivity. As the magnitude of K_e is poorly constrained, we have varied this parameter in our simulations. While K_e might be expected to have meridional structure (likely increasing from pole to equator), we expect that only those simulations that have an overturning with a larger meridional extent, *e.g.* low values of F_b and brine rejection in the low latitudes, or high values of κ, would be sensitive to these variations.

We also include a representation of diabatic transport, which flows across density surfaces in the ocean interior and occurs due to mixing at scales smaller than the mesoscale. This vertical turbulent mixing is parameterized by a small-scale turbulent eddy diffusivity κ, which supports a vertical advection-diffusion balance in the ocean interior, $wb_z = (\kappa b_z)_z$. Note that subscripts y, z, and t in this section are used to indicate partial derivatives. In the isopycnal model, the vertical velocity is approximated by

$$w(y) \approx \frac{\kappa}{\Delta z_n}, \tag{4.8}$$

where Δz_n is the thickness of the layer above the interface in question (Thompson et al., 2019). This approximation is valid if vertical variations in κ are small relative to the buoyancy gradient ($\kappa_z b_z \ll \kappa b_{zz}$). The diabatic streamfunction is defined such that

$$\Psi_{\mathrm{diabatic}}(y) = \int_{S.\,pole}^{y} w(y')L(y')\,\mathrm{d}y'. \tag{4.9}$$

4.2 Buoyancy Forcing

The last term on the right-hand side of Eq. 4.3 accounts for the buoyancy forcing at the ocean-ice interface. The buoyancy forcing arises from both differential heat uptake (changing the water temperature) and phase changes (changing salinity); we assume the latter to be the dominant cause of buoyancy differences on Enceladus. Phase changes (melting–refreezing of ice and aqueous exsolution–dissolution) must occur to compensate for processes that smooth out the meridional ice thickness gradients.

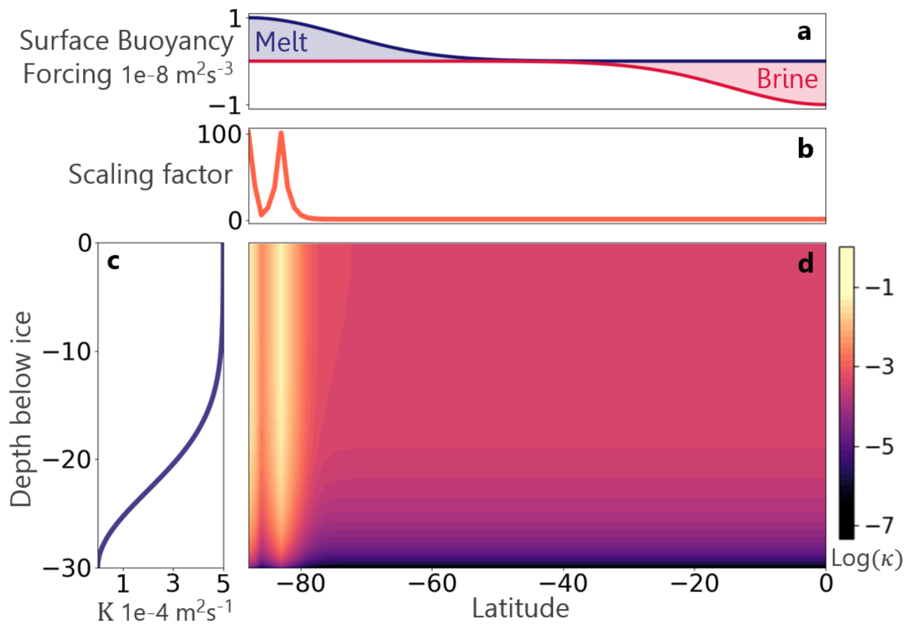

Figure 4.2: Depiction of key model parameters for control run values. (a) The prescribed surface buoyancy forcing (F_{b}) as a function of latitude for the southern hemisphere. The remaining panels show the components of the diapycnal diffusivity (κ). We include a scaling factor that varies with latitude (b), which is used in simulations that have enhanced polar mixing (plumes). κ also has a vertical dependence (shown in c). The spatial distribution of κ (logarithmic scale, e.g. $-1 = 10^{-1}$) is illustrated in the contour plot (d).

Over sufficiently long time scales, thick ice sheets deform plastically, leading to ice transport down the thickness gradient (Goodman, 2003). However, this flow is proportional to the gravitational force, which means it should be weak on a small moon such as Enceladus (g = 0.113 m s^{-2}), but could be significant on Europa (g = 1.315 m s^{-2}) and Titan (g = 1.352 m s^{-2}). An ice pump mechanism (Lewis and Perkin, 1986) could also be active, particularly for a thick shell in isostasy. The pump mechanism is fueled by the change in melt temperature as a function of pressure. Under the deeper regions of the ice shelf (at higher pressure) the melt point is lower, and the water at the interface is colder than that at shallower interfaces. If this cold water is displaced (by tides or other mechanisms), it will move up to the shallower regions where it will serve as a heat sink and promote freezing. This process would tend to reduce thickness gradients in the ice shell at a rate proportional to the temperature gradient along the base of the ice shell. The rate is proportional to the interface depth variations, such that we would expect tens of meters of ice transport per Enceladus year, but the specific rate also depends on the ocean circulation itself. In order to sustain ice shell thickness gradients against such smoothing mechanisms, ice formation is required in thicker regions and melt in thinner regions. Thus, Enceladus' ice thickness pattern implies the existence of significant buoyancy forcing variations at the ocean-ice interface.

Water within density layers that intersect this mixed layer, or outcrop, is influenced by the buoyancy flux into the surface ocean that can give rise to water mass transformation. In the model, we prescribe a buoyancy flux F_b at the interface in each hemisphere of the form:

$$F_\mathrm{b}(y) = F_0\left\{exp\left[-\left(\frac{|y-\phi_m|}{\sigma}\right)^2\right] - exp\left[-\left(\frac{|y-\phi_b|}{\sigma}\right)^2\right]\right\}, \tag{4.10}$$

where F_0 is the forcing magnitude (in m^2 s^{-3}). Regions of melt are centered at the poles ($|\phi_m| = 90° = 396$ km), and the forcing decays exponentially over a length scale of $\sigma = 90$ km. Regions of ice growth and brine rejection are centered at the equator ($\phi_b = 0° = 0$ km) for the control run, but are varied for other simulations. Transformation in the ocean surface boundary layer, and thus the meridional transport, is quantified by the relationship (Marshall and Radko, 2003):

$$\Psi_F = F_b(y)L(y)(b_y|_\mathrm{sfc})^{-1}, \tag{4.11}$$

where the last term is the meridional buoyancy gradient within the ocean mixed layer.

4.3 Reaching equilibrium

With parameterizations for the terms in Eq. 4.3 in hand, a solution for the ocean circulation can be determined by integrating in time to a steady state. In the mixed layer, where we have a buoyancy forcing and b_z is by definition negligible, we can divide both sides of Eq. 4.3 by the meridional buoyancy gradient at the interface ($b_y|_\mathrm{sfc}$), to get:

$$v_\mathrm{out.} = \frac{\partial y}{\partial t} = \frac{1}{h}\left(K_\mathrm{e}s - \frac{F_\mathrm{b}}{b_y|_\mathrm{sfc}}\right), \tag{4.12}$$

which describes the time evolution of the outcrop location for each layer interface. Meanwhile, in the ocean interior, where there is no influence from the buoyancy forcing, we can divide by b_z to arrive at:

$$w_{\text{int.}} = \frac{\partial z}{\partial t} \approx \left(K_{\text{e}} \frac{\partial s}{\partial y} + \frac{\kappa}{\Delta z} \right), \tag{4.13}$$

where $w_{\text{int.}}$ is the vertical velocity of the layer interface at a given location. Eq. 4.13 can also be derived directly from conservation of mass in the ocean interior.

The simulations presented in the paper were initialized with five layers. The buoyancy difference between each layer is $\Delta b = 4 \times 10^{-5}$ m s^{-2}. The layer interfaces were initially flat, shallow, and outcropped in the mid and high latitudes, in a region of prescribed sea ice melt. Various initial conditions were tested, including the use of deeper layers and outcrops in regions of ice formation. These simulations achieved the same steady state solutions, suggesting that solutions are not sensitive to initial conditions.

The ocean interior is modeled on a semi-adaptive grid in which each layer interface has a fixed number of meridional grid points. Thus, the vertical resolution is determined by the number of buoyancy layers. The meridional resolution is adjustable and set to 2° for this work. The ocean-ice interface depth varies in accordance with the prescribed ice structure described above. For the simulations we present in this study, we assume symmetry about the equator and run a single hemisphere. We also prescribe a sinusoidal structure to the interface, such that the difference in depth between equator and pole is Δ_{ice}. Simulations with different structures and various values of Δ_{ice} were tested, but have not been included because effects on the ocean structure and flow are small. The outcrop locations are allowed to vary freely, independent of the interior grid. The model accounts for changes in the zonal extent of latitude circles between the equator and pole to ensure conservation of volume. The model also accounts for changes in circumference with depth, though this feature is not significant for the range of parameters explored in this work.

This zonally-averaged model does not explicitly include zonal flows. However, we would expect a zonal flow to be present on Enceladus and perhaps, as is the case in Earth's Southern Ocean, it could even be stronger than the meridional circulation. However, for the purposes of understanding heat and nutrient transport, the meridional flow is most relevant and is thus the focus of this work. A strong zonal flow, or even zonal jets (Soderlund et al., 2014) may coexist with our modeled meridional circulation in the ocean interior. If the zonal flow at the ocean-ice boundary were sufficiently strong, it could produce a frictional stress and a meridional Ekman transport near the boundary (Marshall and Radko, 2003). This transport has not been included in the model, but could be easily incorporated in our residual circulation framework, as has already been done in Southern Ocean models that include a wind-driven Ekman transport (Thompson et al., 2019).

We summarize the processes described above as two key balances: (i) the flow in the ocean interior either towards or away from the ocean-ice interface must balance the water mass transformation in the mixed layer. Until this balance is met, any net convergence in the mixed layer will induce density layer outcrop displacement. (ii) Any net volume transport, through vertical mixing, into a density layer in the ocean interior must be transported along the layer and eventually flow into the mixed layer. If a divergence in the adiabatic transport is not balanced locally by a convergence in the diabatic transport, the volume flux convergence within a layer induces a change in layer depth. Once the layers reach equilibrium, the net flow into and out of each layer must exactly cancel by mass conservation. Though we do not track the flow below the bottom layer, the vertical fluxes are balanced such that mass is conserved everywhere. Note that at steady state, the diabatic transport across a given interface is balanced by the total adiabatic lateral transport above that level, such that $\Psi_{\text{diabatic}} = -\Psi_{\text{adiabatic}} = K_{\text{e}}(s - s_{\text{ice}})2\pi\cos\phi$. Finally, the equilibrium solution requires that Eq. 4.12 and Eq. 4.13 are identically zero.

References

M. Beuthe, A. Rivoldini, and A. Trinh. Enceladus's and Dione's floating ice shells supported by minimum stress isostasy. *Geophysical Research Letters*, 43(19):10,088–10,096, 2016. doi:10.1002/2016GL070650.

O. Čadek, O. Souček, M. Běhounková, G. Choblet, G. Tobie, and J. Hron. Long-term stability of Enceladus' uneven ice shell. *Icarus*, pages 476–484, 2019. ISSN 10902643. doi:10.1016/j.icarus.2018.10.003.

M. H. Carr, M. J. S. Belton, C. R. Chapman, M. E. Davies, P. Geisslerk, R. Greenbergk, A. S. Mcewenk, B. R. Tuftsk, R. Greeley, R. Sullivan, J. W. Head, R. T. Pappalardo, K. P. Klaasen, T. V. Johnson, J. Kaufman,

D. Senske, J. Moore, G. Neukum, G. Schubert, J. A. Burns, P. Thomas, and J. Veverka. Letters to Nature: Evidence for a subsurface ocean on Europa. *Nature*, 391:363–365, 1998.

G. Choblet, G. Tobie, C. Sotin, M. Běhounková, O. Čadek, F. Postberg, and O. Souček. Powering prolonged hydrothermal activity inside Enceladus. *Nature Astronomy*, pages 841–847, 2017. ISSN 2397-3366. doi:10.1038/s41550-017-0289-8.

P. R. Gent and J. C. McWilliams. Isopycnal mixing in ocean circulation models. *Journal of Physical Oceanography*, pages 150–155, 1990.

J. C. Goodman. Glacial flow of floating marine ice in "Snowball Earth". *Journal of Geophysical Research*, 108:1–12, 2003. ISSN 0148-0227. doi:10.1029/2002jc001471.

S. Groeskamp, S. M. Griffies, D. Iudicone, R. Marsh, A. G. Nurser, and J. D. Zika. The water mass transformation framework for ocean physics and biogeochemistry. *Annual Review of Marine Science*, pages 271–305, 2019. ISSN 1941-1405. doi:10.1146/annurev-marine-010318-095421.

E. L. Lewis and R. G. Perkin. Ice pumps and their rates. *Journal of Geophysical Research: Oceans*, pages 11756–11762, 1986. doi:10.1029/JC091iC10p11756.

A. H. Lobo, A. F. Thompson, S. D. Vance, and S. Tharimena. A pole-to-equator ocean overturning circulation on Enceladus. *Nature Geoscience*, 14: 185–189, 2021. ISSN 1752-0908. doi:10.1038/s41561-021-00706-3.

R. Lumpkin and K. Speer. Global ocean meridional overturning. *Journal of Physical Oceanography*, 37:2550–2562, 10 2007. ISSN 00223670. doi:10.1175/JPO3130.1.

J. Marshall and T. Radko. Residual-mean solutions for the antarctic circumpolar current and its associated overturning circulation. *Journal of Physical Oceanography*, 33(11):2341–2354, 2003. ISSN 0022-3670. doi:10.1175/1520-0485(2003)033<2341:RSFTAC>2.0.CO;2.

J. Marshall and K. Speer. Closure of the meridional overturning circulation through Southern Ocean upwelling. *Nature Geoscience*, 5(3):171–180, 2012. ISSN 1752-0908. doi:10.1038/ngeo1391.

F. Nimmo and R. T. Pappalardo. Ocean worlds in the outer solar system. *Journal of Geophysical Research: Planets*, 121(8):1378–1399, 2016. doi:10.1002/2016JE005081.

F. Postberg, S. Kempf, J. Schmidt, N. Brilliantov, A. Beinsen, B. Abel, U. Buck, and R. Srama. Sodium salts in E-ring ice grains from an ocean below the surface of Enceladus. *Nature*, 459(7250):1098–1101, 2009. ISSN 00280836. doi:10.1038/nature08046.

K. M. Soderlund, B. E. Schmidt, J. Wicht, and D. D. Blankenship. Ocean-driven heating of Europa's icy shell at low latitudes. *Nature Geoscience*, pages 16–19, 2014. ISSN 17520894. doi:10.1038/ngeo2021.

A. F. Thompson, S. K. Hines, and J. F. Adkins. A southern ocean mechanism for the interhemispheric coupling and phasing of the bipolar seesaw. *Journal of Climate*, pages 4347–4365, apr 2019. ISSN 0894-8755. doi:10.1175/JCLI-D-18-0621.1.

G. K. Vallis. *Atmospheric and Oceanic Fluid Dynamics*. Cambridge University Press, Cambridge, U.K., 2006.

C. Zimmer, K. K. Khurana, and M. G. Kivelson. Subsurface oceans on Europa and Callisto: Constraints from Galileo magnetometer observations. *Icarus*, 147(2):329–347, 2000. ISSN 0019-1035. doi:10.1006/icar.2000.6456.

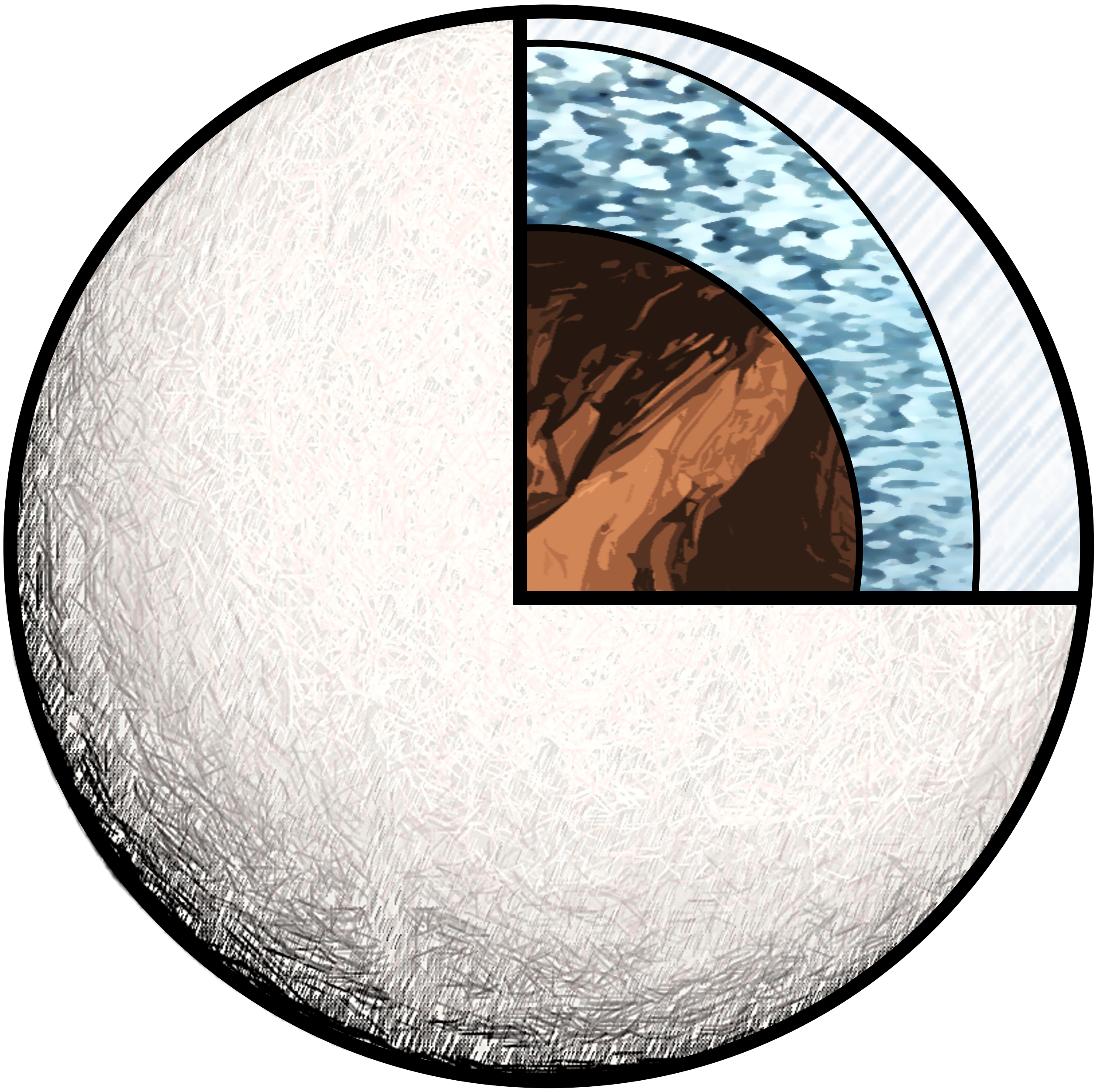

Chapter 5

A POLE-TO-EQUATOR OCEAN OVERTURNING CIRCULATION ON ENCELADUS.

Enceladus' ocean is the best characterized and potentially most accessible of the many oceans in our solar system studied to date (Glein et al., 2019). The polar asymmetry in its surface geology and active plumes at its south pole are consistent with regional heating (Choblet et al., 2017) that suggests chemical and thermal gradients on a global scale. *Cassini* spacecraft measurements provided compelling evidence for a subsurface ocean, as inferred from the south pole's high heat output (Spencer et al., 2006). Thermodynamic arguments (Collins and Goodman, 2007) and interpretations of the tiny moon's gravity and spin states (McKinnon, 2015) indicate the ocean is global, with estimated depth of at least 30 km (Čadek et al., 2019; Beuthe et al., 2016). Particles sampled from the south polar plume indicate organics in the ocean (Postberg et al., 2018), and suggest a modestly high pH with chemical affinity supportive of methanogenesis (Waite et al., 2017). Models of tidal heating that sustain the ocean and the non-uniform ice thickness indicate flexure of a porous seafloor, and localized outflow of warm fluids in the southern regions (Choblet et al., 2017). This regional upwelling of warm fluid may also suggest strong, localized melting and associated mixing and fractionation at the ocean-ice boundary, where materials enter the stream of plume ejecta.

Spatial heterogeneity in Enceladus' ice shell strongly indicate that localized regions of freezing and melt at the ocean-ice interface modify the density of the subsurface ocean through heat exchange, freshwater fluxes, and brine rejection (Postberg et al., 2009; Vance and Goodman, 2009). This scenario is analogous to Earth's high latitude oceans where variations in surface buoyancy forcing due to interactions with sea ice control the large-scale circulation (Marshall and Speer, 2012; Ferrari et al., 2014). Indeed, with some knowledge of interior mixing rates, the distribution of density fluxes into the ocean can constrain the large-scale overturning circulation's structure and strength (Marshall and Radko, 2003). We leverage this approach, commonly referred to as water mass transformation (Groeskamp et al., 2019), in our analysis of Enceladus' circulation.

A steady overturning circulation requires transformation of waters between different density classes, implying stratification in the ocean interior. Heat and freshwater exchange at the ocean-ice interface (Soderlund, 2019), as well as the generation of convective plumes (Goodman, 2003) are key mechanisms for the production and destruction, or consumption, of water of varying densities. If regions associated with production and consumption of water with distinct properties are spatially separated, a circulation must arise to connect these regions and close the overturning. In particular, if the separation between regions of melt and freezing is comparable to the size of Enceladus' ocean, then we predict the ocean will support a large-scale, pole-to-equator circulation (Zhu et al., 2017). Previous work on ice-covered oceans has largely focused on thermal driving and its impact on the zonal circulation, such as Europa's (Soderlund et al., 2014), and on the homogenization of interior properties through mixing. Freshwater-driven processes have received less attention, although previous studies have shown how this forcing can generate turbulent eddy transport in a snowball Earth scenario (Jansen, 2016) and a layered stratification on Europa (Zhu et al., 2017); other studies have highlighted their potential importance (Soderlund, 2019; Cullum et al., 2016) for various ocean worlds. Here, we show the potential for freshwater forcing at the ocean-ice interface to stratify the ocean interior.

For an ice shell at steady state, the spatial distribution of freshwater fluxes, i.e. regions of melting and freezing, can be linked to observed variations in ice shell thickness. The freshwater fluxes in turn constrain the circulation dynamics within Enceladus' ocean. Constraints on the overturning circulation would improve estimates of oceanic heat, freshwater, and nutrient transport, helping to close the system's energy budget and identifying how chemical gradients may be established and maintained. As we will show, the resulting stratification also affects the interpretation of measurements from Enceladus' surface plumes, including prior constraints on the ocean's composition and habitability (Waite et al., 2017). Here, we develop an idealized model (Fig. 5.1) to understand controls on the circulation within Enceladus' ocean. Our approach is to explore the sensitivity of the ocean circulation's structure in response to changes in ocean characteristics, such as surface buoyancy forcing and interior mixing properties, including spatially-heterogeneous turbulent plumes.

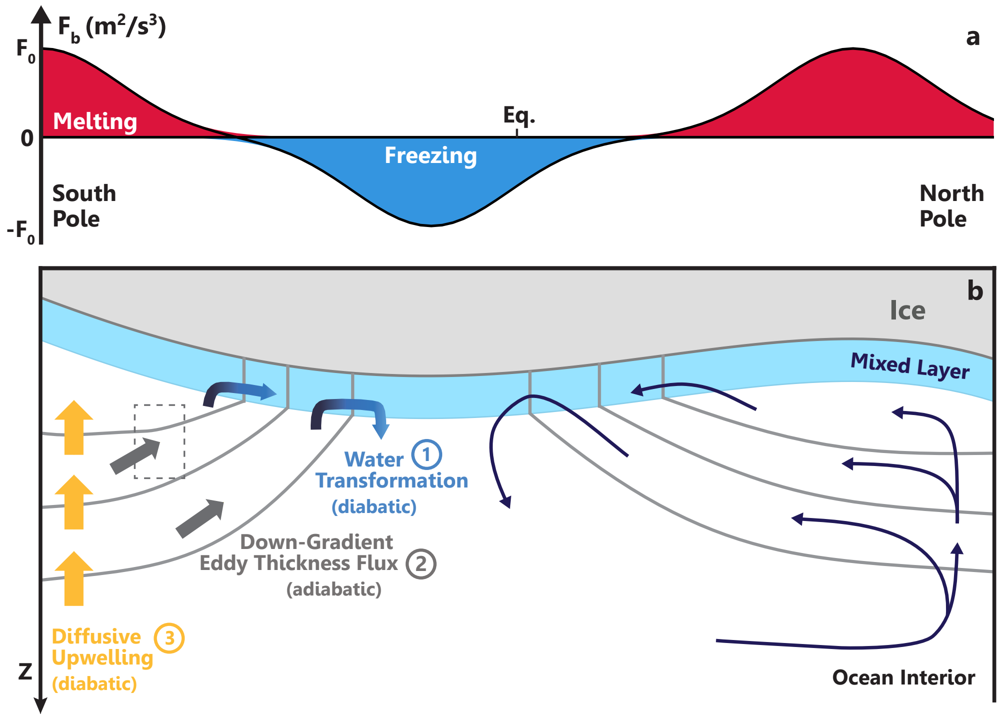

Figure 5.1: Diagram of Enceladus-like ocean and circulation. (a) Inferred surface buoyancy forcing (F_b, m^2/s^3), based on measured meridional ice thickness gradients (shown in b). (b) Schematic of the ocean interior divided into layers of different densities (grey lines). The right side provides a schematic view of the total overturning circulation, while the left illustrates the physical processes that support this circulation. The grey box is expanded in Fig. 4.1. This figure is not drawn to scale. The model assumes zonal symmetry, and simulations described in this work focus only on the Southern Hemisphere, with a simplified ice gradient (see Fig. 5.2) and surface buoyancy forcing (see Fig. 4.2)

5.1 Methods

The use of an idealized ocean model enables a broad assessment of plausible stratification and circulation regimes and their dependence on characteristics of Enceladus' ocean. This model, summarized below and described in detail in Chapter 4, enables us to (i) identify the primary dynamical balances that govern the circulation, (ii) explore possible global circulation configurations, and (iii) optimize parameter choices for more realistic but computationally-intensive general circulation models. This work will also aid in relating key parameters to observable properties from future missions. An important assumption of the model is that the global ocean sustains some level of stratification. While the density of each layer is prescribed, ocean stratification is determined from the model output based on the layer depths and thicknesses. Steady state conditions ensure conservation of mass and buoyancy in each density layer. Salinity is assumed to provide the stratifying agent, which is discussed further in Section 5.4, where we compare model densities to estimated temperature and salinity ranges for Enceladus.

Following similar terrestrial ocean applications (Marshall and Radko, 2003; Thompson et al., 2019), the model tracks the transport of water between a discrete number of fixed density classes. Transfer between layers, or "transformation," occurs due to diabatic processes through two mechanisms: mixing in the interior or direct forcing at the ocean-ice interface. We link the latter to spatial variations in the ice shell thickness.

In steady state, the formation or melt of ice must occur where the ice shell is anomalously thick or thin, respectively, to sustain ice shell thickness gradients. This pattern of melting and freezing would oppose the smoothing tendency of the ice pump mechanism (Lewis and Perkin, 1986) that arises from changes in melt temperature as a function of pressure (Chapter 4). The ice pump mechanism would be particularly strong for a thick shell in isostasy, but the exact rate depends on ocean circulation. Here, we do not address the physical drivers behind the phase changes, but they could arise, for example, due to geothermal heat release or local upwelling could drive melting in localized regions with a thinner ice shell. Regardless of the cause, spatial variations in ice thickness imply significant forcing through density (freshwater) fluxes at the ocean-ice interface. We also consider a wide range of buoyancy forcing due to the uncertainty in its magnitude.

Mixing in the ocean interior is assumed to occur primarily through rotationally constrained geostrophic turbulence (Speer et al., 2000; Jansen, 2016; Soderlund et al., 2014). The source of this geostrophic turbulence that sustains the overturning circulation is itself influenced by the ice shell thickness and its associated pattern of freezing and melting. Together these establish an ocean density that varies not only vertically, but also laterally. Horizontal density gradients, represented in our model as tilting density layers, provide the source of potential energy from which ocean eddies form and grow through baroclinic instability (Green, 1970). These eddies both stir properties along density surfaces and give rise to an eddy volume transport (Chapter 4). This adiabatic motion, or motion within density classes, plays the critical role of transporting water between spatially-separated sites of water transformation.

Interior mixing that governs the volume transport between density layers occurs through smaller-scale turbulence. In Earth's ocean, interior mixing arises due to the action of internal wave breaking (Munk, 1966), whereas on Enceladus, the interior mixing may be significantly amplified by turbulent plumes (Vance et al., 2018; Choblet et al., 2017) that may be spatially heterogeneous. At steady state, interior diabatic transport and adiabatic advection are balanced by transformation at the ocean-ice interface (fig. 5.1b).

The model evolves the interfaces between various density classes in two ways. In the ocean interior, convergence of mass in a density class due to turbulent mixing, parameterized as a turbulent diffusivity κ, either changes the thickness of a layer through a vertical displacement $w_{\text{int.}}$ (Eq. 4.13), or is balanced by adiabatic lateral transport. The latter is incorporated using a well-tested closure (Gent and McWilliams, 1990) that depends on the slope of density surfaces and an isopycnal eddy diffusivity K_{e}. The latitudinal position where density layers outcrop at the ocean-ice interface may also evolve in time, $v_{\text{out.}}$ (Eq. 4.12), due to an imbalance between water supplied adiabatically to the interface and the transformation to a different density class. A solution for the overturning circulation can be determined by integrating these velocity equations in time until a steady state is achieved. While this zonally-averaged model does not explicitly include zonal flows, based on thermal wind balance the existence of a lateral density gradient will support a vertically-sheared zonal flow. This zonal flow may coexist with the simulated overturning circulation, as in Earth's Southern Ocean, but does not impact the overturning dynamics that are the focus of this study (see Chapter 4).

Model parameters enable us to assess how various physical properties of the Enceladus system influence the global circulation. The diapycnal diffusivity κ describes the intensity of vertical mixing, or the exchange across layers, in the ocean interior. Increased tidal heat release at the ocean-core boundary could intensify turbulent mixing in the ocean interior and lead to a higher κ overall or to regional increases in the case of ocean plumes. The isopycnal diffusivity K_{e} captures the efficiency of baroclinic eddies in the ocean interior. The magnitude of K_{e} could vary spatially, due to changes in the baroclinic deformation radius, for instance, but we apply a constant K_e in the simulations described below for simplicity. The magnitude of the density (buoyancy) forcing into the ocean F_b represents the rate of ice formation/melt and its meridional distribution impacts the location where transformation takes place. Starting from a control experiment, parameters were systematically varied in the simulations, as itemized in Table 5.1 and described in Section 5.2.

Results from our parameter space exploration highlight the sensitivity of the stratification to the prescribed mixing parameters. Intense diapycnal mixing can weaken the stratification, particularly if coupled with weak isopycnal diffusivity. Until further observational or energetic constraints can be placed, future GCM results for vertical structure or flow velocities should carefully assess the dependence of results on these parameter choices. However, the meridional structure of the ocean is likely to be more robust to variations in κ, but sensitive to changes in boundary layer forcing. In future simulations, the connection between ice shell thickness and buoyancy flux should be evaluated in a model where the ocean circulation is coupled to an evolving ice shell.

Model Parameter	**Control Value**	**Min**	**Max**
Δb	4×10^{-5} m s^{-2}	-	-
K_e	10^3 m^2 s^{-1}	200 m^2 s^{-1}	5000 m^2 s^{-1}
κ	5×10^{-4} m^2 s^{-1}	10^{-4} m^2 s^{-1}	10^{-2} m^2 s^{-1}
Δice	10 km	1 km	20 km
ϕ_b	0°	0°	60°
F_0	10^{-8} m^2 s^{-3}	10^{-10} m^2 s^{-3}	10^{-7} m^2 s^{-3}

Table 5.1: Simulation parameters for control run and the range of values tested for parameters that were explored.

5.2 The Dynamical Balance of a Pole-to-Equator Overturning

To provide intuition for the dynamics influencing the ocean stratification and circulation for a given forcing at the ocean surface (for Enceladus, the ocean-ice interface), we first describe an equilibrated state for a set of control parameters. For this simulation, the ocean-ice interface is 10 km deeper at the equator than at the pole, and the buoyancy flux into the ocean $F_\mathrm{b}(y)$ varies meridionally and has a maximum amplitude of 10^{-8} m^2 s^{-3} (Fig. 5.1a), with amplitude F_0, maxima in a region of strong melt ϕ_m, and minima in regions of ice formation ϕ_b (see Chapter 4). While buoyancy aggregates thermal and haline contributions to density anomalies, our discussion focuses on how haline anomalies influence the distribution of F_b. Spatial variations in the magnitude of the vertical heat flux at the ocean-ice interface are assumed to be small (see Section 5.4). We initialize the model with 5 layers of uniform buoyancy (density) with a fixed buoyancy jump between each layer; the model is always stably stratified. The magnitude of interior mixing (diapycnal diffusivity $\kappa \approx 5 \times 10^{-4}$ m^2 s^{-1}) is laterally uniform throughout the ocean except near the poles where we prescribe enhanced diapycnal mixing to represent convective plumes. Values for control parameters are provided in Chapter 4.

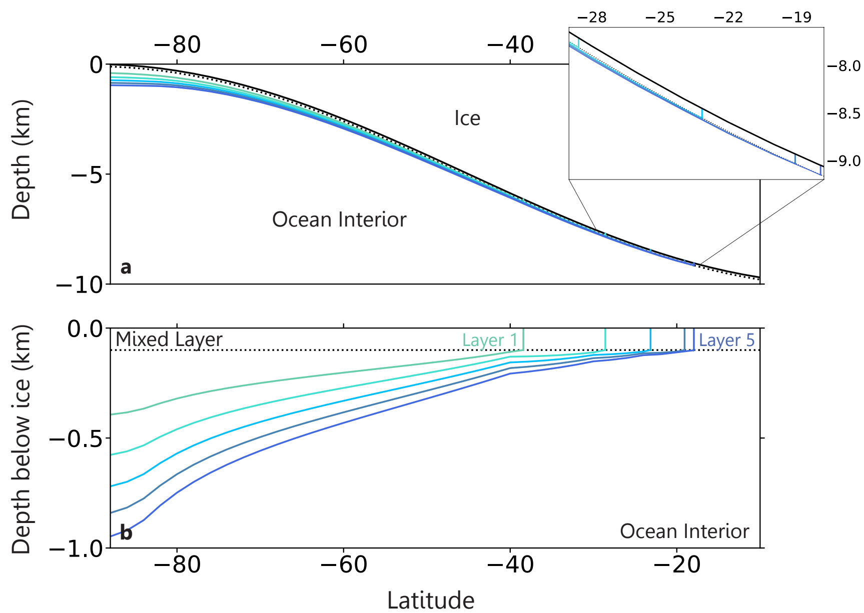

Figure 5.2: Steady state distribution of density layers in the control run. The top panel shows the position of the layer interfaces with respect to the sloped ocean-ice interface. The bottom panel shows the same layers, plotted as depth below the ocean-ice interface to more easily visualize the stratification structure.

The density structure of the control simulation (Fig. 5.2), governed by conservation of mass and buoyancy in each layer, illustrates that an overturning circulation is sustained in a relatively shallow layer below the ice shell. The stratification penetrates only ~ 1 km below the ocean-ice interface, but varies from the pole to the lower latitudes where density surfaces intersect the ocean-ice boundary layer. Density layers are thicker in the polar region, leading to deeper, but weaker stratification. Closer to the equator density layers shoal and the stratification intensifies. This stratification generates density-layer thickness gradients (Fig. 5.3a) that support an equatorward adiabatic circulation, or transport within a density layer (grey arrows in Fig. 5.1), which transports water towards the ocean-ice boundary and converges mass into the region of ice formation at lower latitudes. The water entering the ocean-ice boundary layer is transformed into denser water by brine rejection near the equator and is subducted into the deep interior. The flow in the deep ocean (below layer 5) flows poleward to conserve mass. This deep water is eventually returned to shallower depths by interior diabatic mixing (yellow arrows, Fig. 5.1), in which dense water becomes lighter and flows upward via the downward turbulent transfer of high-latitude melt that sustains the lightest (freshest) layer.

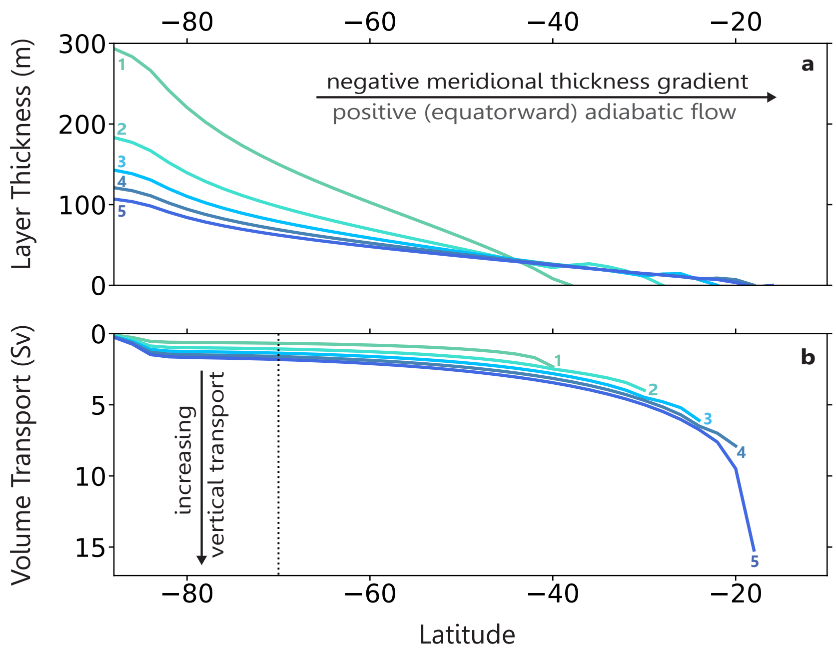

Figure 5.3: Characteristics of the control simulations. (a) Thickness of each of the five density layers (m) as a function of latitude. (b) Volume transport (1 Sv = 10^6 m^3 s^{-1}) across density surfaces, integrated such that $\Psi_{\text{diabatic}}(\phi) = \int_{-90}^{\phi} w\, 2\pi R \cos(\phi')\, \mathrm{d}\phi'$, where ϕ' is an integration variable. The black dashed line at 70° latitude indicates the location where lateral fluxes are calculated for Fig. 5.4. The y-axis has been inverted so that the deeper high density layer (5) is shown at the bottom and the lightest density (1) is at the top.

Enhanced vertical mixing at the poles, represented by increased diapycnal diffusivity (κ), increases density-layer thickness gradients and strengthens the adiabatic branch of the circulation at the poles. This increases the total volume transport or overturning circulation magnitude (Fig. 5.3b), illustrating the tight connection between adiabatic and diabatic motions. However, a large-scale overturning circulation is present even for a system with uniform interior mixing (Fig. 5.4g), where polar plumes were uniformly distributed or absent.

5.3 Sensitivity of Circulation to Ocean Properties

We next consider the sensitivity of the stratification and circulation to key parameters in the model, and seek to relate these parameters to observable quantities. To characterize the ocean's response to varying parameters, we examine three properties: (i) the outcrop position, where each layer interface intersects the ocean-ice boundary, (ii) the stratification penetration depth, equivalent to the depth of each layer interface at the pole, and (iii) the volume transport within each layer.

The layer outcrop positions are strongly constrained by the surface buoyancy flux distribution $F_{\mathrm{b}}(y)$. A poleward shift in the ice formation region (ϕ_b) confines low-density layers to higher latitudes (Fig. 5.4a). This more compact configuration increases both layer slopes and layer thickness gradients, resulting in stronger adiabatic transport (Fig. 5.4b). Meanwhile, reductions in the ice formation rates, F_0, or increases in eddy activity, K_{e}, (Fig. 5.4c,e) result in outcropping closer to the equator, where the mixed layer transformation is sufficiently strong to balance interior mixing. For large K_{e}, enhanced eddy fluxes result in stronger, but shallower, overturning in the upper ocean (Fig. 5.4f).

In contrast to the parameters described above, stratification depth is more sensitive to the magnitude of vertical mixing κ (Fig. 5.4g). An increase in κ enhances the diabatic exchange between density layers, increasing lateral layer thickness gradients. This results in both stronger lateral transport (Fig. 5.4h) and a deeper overturning circulation. To balance the stronger overturning, layers will shift to outcrop in regions where surface buoyancy forcing and water mass transformation is more intense. Therefore, while strong vertical mixing (high κ) and strong baroclinic eddy activity (high K_{e}) have opposite effects on layer depth, both lead to a broader and stronger overturning circulation.

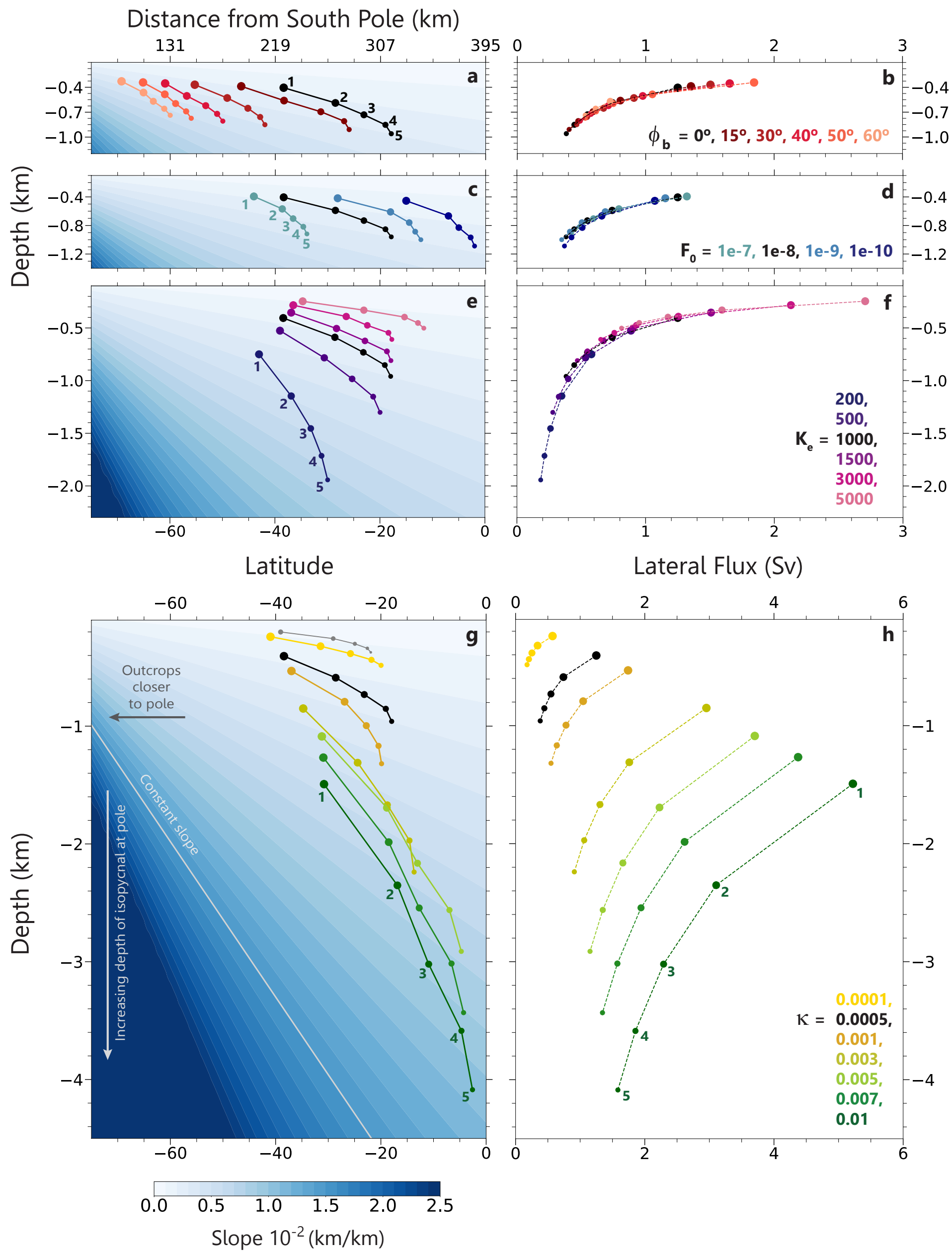

Figure 5.4: Phase diagram depicting isopycnal slope. From top to bottom, we vary the parameters ϕ_b (° latitude), F_0 (m^2 s^{-3}), K_e (m^2 s^{-1}), κ (m^2 s^{-1}). For panels on the left, the y-axis shows the depth (km) of each layer interface at the south pole and the x-axis shows latitude of interface outcrop locations. The five outcrops of each model are plotted with markers of the same color. Background colors indicate lines of constant isopycnal slope. The right panels show lateral volume flux (1 Sv = 10^6 m^3 s^{-1}) within each layer at 70° latitude. Model results shown in grey (g) are for a control-like simulation where polar amplification of diapycnal mixing κ has been removed.

5.4 Ocean Temperature and Salinity

Our control model parameters (Table 5.1) were initially selected based on Earth-like values, although the value of Δb was intentionally chosen to be small. Given that Enceladus' ocean is nearly an order of magnitude deeper than Earth's, our parameters were optimized for a weak stratification. However, we find that the isopycnals concentrate in the upper portion of the ocean in the control simulation, producing stronger stratification near the interface and weaker stratification in the deep ocean. We do not account for bottom boundary processes that could affect the deeper ocean density structure.

The buoyancy gradients in the upper ocean could occur due to variations in temperature, salinity, or a combination of both. Our model does not distinguish between these scenarios. However, for the predicted pressure and temperature range in Enceladus' ocean (Fig. 5.5, left), the equations of state predict that the density variations are almost entirely controlled by salinity.

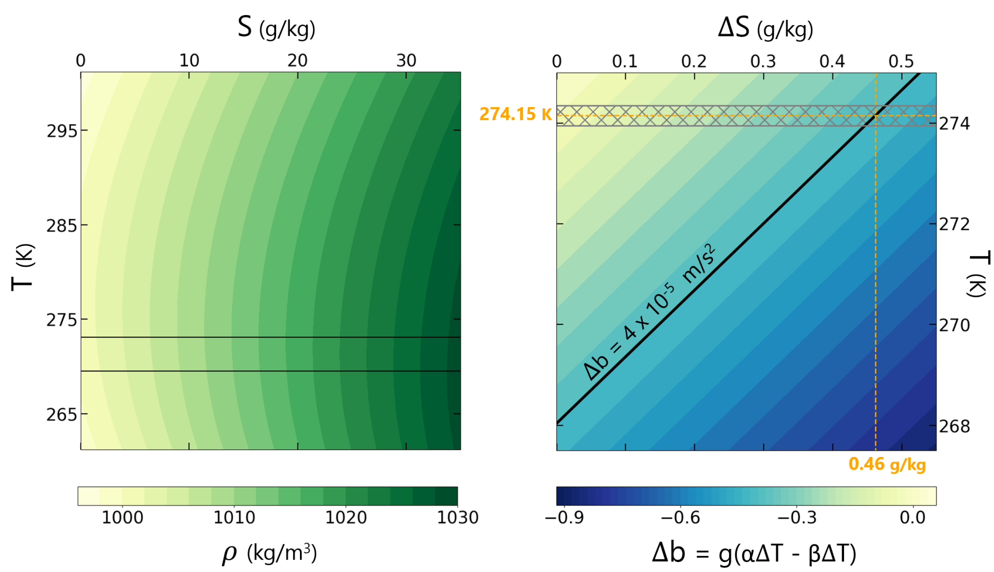

Figure 5.5: (Left) Predicted density for various temperatures and salinities at 2 MPa. The black lines highlight the temperature range relevant for Enceladus (Vance et al., 2018). (Right) Equivalent change in temperature and salinity to produce the buoyancy difference (Δ_b) between layers in the model, calculated at 2 MPa, with a mean temperature of 274.15 K. The black line highlights the model's Δb. For comparison, the grey hatching shows the expected variations in ocean temperature if the composition is kept constant (obtained using TEOS-10).

Using the linearized equation of state, a thermal expansion coefficient $\alpha = 5.788 \times 10^{-5}$ K^{-1}, and a saline contraction coefficient $\beta = 7.662 \times 10^{-4}$ kg g^{-1} (obtained using TEOS-10 for 2 MPa), we can verify the changes required to produce a buoyancy difference of $\Delta b = 4 \times 10^{-5}$ m s^{-2} (the difference between two sequential layers). These coefficients were obtained using a base temperature of 274 K, a degree higher than estimated in the literature (Vance et al., 2018), to remove negative thermal expansivity arising from the lower assumed salinity of 12 ppt consistent with *Cassini* measurements (Glein et al., 2019). These effects are probably relevant near the ice shell (Melosh et al., 2004), but are beyond the scope of this work. Under these conditions, if the ocean had constant salinity, a 6 K temperature difference would be required between layers (30 K overall). This is more than three times the temperature difference required for Earth-like conditions (1.7K). Whereas, for an isothermal ocean, a 0.46 g kg^{-1} salinity change between layers could account for the difference in buoyancy (Fig. 5.5, right).

Assuming that temperature variations in the bulk of the ocean are limited to less than 4 K (Vance et al., 2018), the buoyancy differences modeled in this work and the ensuing circulation can be attributed almost entirely to salinity differences. The total variation in salinity between our lowest density layer and our highest density layer is estimated to be roughly 2 g kg^{-1}. Further constraints could be obtained in future work through the use of additional model layers.

5.5 Implications for Ocean Structure and Composition

The idealized model indicates that a stratified ocean with a freshwater lens in the polar regions is sustainable across a broad range of parameter space with the lens' equatorward extent bounded by regions of net ice growth. This implies a direct link between the surface buoyancy forcing at the ocean-ice interface and the interior ocean stratification and circulation. If ice formation occurs predominantly at mid to high latitudes, an overturning circulation can be confined to the poles. As regions of ice formation extend to lower latitudes, a pole-to-equator overturning emerges. We expect that future ice shell measurements will allow for better estimates of surface buoyancy flux through higher resolution mapping of regional ice-shell thickness variations, and also by constraining the ice shell dynamics and composition.

Cassini measurements of the plumes venting into space from Enceladus' southern pole have provided the best insight into Enceladus' ocean composition. Based on studies of freshwater-driven processes (Zhu et al., 2017), we suggest that low-density layers tend to form where the ice is thinnest, as is the case for Enceladus' south pole. Given the expected temperature range for Enceladus (Vance et al., 2018), the ocean water thermal expansion coefficient would be very small ($\sim 5 \times 10^{-5}$ K^{-1} at 2 MPa, see Section 5.4). Therefore, salinity differences are likely the dominant source of density variations. If we assume the ocean has mean salinity equal to or larger than that of our deepest layers, the freshwater lens feeding the surface plumes would have salinity at least 2 g/kg lower than the ocean mean (Section 5.4).

Our results have focused on the circulation, but oceanic flow also influences the transport of heat and other tracers. While recent tidal heat dissipation studies support that the ocean is primarily heated from below at the poles (Choblet et al., 2017), these patterns do not match the more complex ocean-ice heat flux pattern believed to be required for ice shell stability (Čadek et al., 2019). Significant meridional overturning could carry a portion of high-latitude geothermal heat flux to lower latitudes via a lateral, likely eddy-driven, circulation. Similarly, freshwater exchange at the ocean-ice interface on Enceladus can establish upwelling and equatorward transport, directed towards sites of brine rejection, qualitatively matching the ocean heat flux required by the ice shell (Čadek et al., 2019). Thus, a pole-to-equator overturning can reconcile these two seemingly contradictory boundary conditions and conflicting views of Enceladus.

By setting global patterns of upwelling and lateral transport, the circulation will also impact the distribution of nutrients sourced from the seafloor. If nutrients are transported upward primarily by ocean plumes, we would expect detrainment to release nutrients in the ocean interior. In Earth's ocean, it has been shown that adiabatic mixing, or stirring along isopycnals, can be an important pathway for nutrient delivery to the surface and can modulate productivity there (Uchida et al., 2020). Thus, determining the distribution of freshwater fluxes at the ocean-ice interface may provide insights into which regions of an icy ocean world would be most amenable to supporting life.

The dynamics we describe for Enceladus are typical of geophysical fluids influenced by stratification and rotation and are therefore likely to occur in other ocean worlds. Most notably, *Cassini* observations indicate Titan's ice shell is 50-100 km thick, with possible spatial variability in thickness exceeding 10 km (Choukroun and Sotin, 2012; Durante et al., 2019), large enough to alter the global density structure of the ocean. In larger ocean worlds like Titan, lateral density gradients may also arise from interactions with the ocean bottom, where a second lithosphere of high-pressure ice resides (Vance et al., 2018). The effects of such variations on the compositional and thermal structure of the ocean might be measured by their influence on the ocean's seismic and electrical properties (Vance et al., 2018). The *Dragonfly* mission, planned to study Titan (Turtle et al., 2017), will carry a geophysical package that may yield clues to the properties of the ocean. In the Jupiter system, the *Europa Clipper* and *JUICE* missions, which will study Jupiter's moons Europa and Ganymede, respectively, in the coming decade (Grasset et al., 2013; Buffington et al., 2017), will constrain variations in ice thickness while also probing electrical properties of the subsurface oceans. Our results highlight the critical need for more detailed studies of global circulation structures in ocean worlds.

References

M. Beuthe, A. Rivoldini, and A. Trinh. Enceladus's and Dione's floating ice shells supported by minimum stress isostasy. *Geophysical Research Letters*, 43(19):10,088–10,096, 2016. doi:10.1002/2016GL070650.

B. Buffington, T. Lam, S. Campagnola, J. Ludwinski, E. Ferguson, B. Bradley, C. Scott, M. Ozimek, A. H. Chalk, and F. Siddique. Evolution of trajectory design requirements on NASA's planned Europa Clipper mission. *Proceedings of the 68th International Astronautical Congress (IAC)*, (IAC-17-C1.7.8), 2017.

O. Čadek, O. Souček, M. Běhounková, G. Choblet, G. Tobie, and J. Hron. Long-term stability of Enceladus' uneven ice shell. *Icarus*, pages 476–484, 2019. ISSN 10902643. doi:10.1016/j.icarus.2018.10.003.

G. Choblet, G. Tobie, C. Sotin, M. Běhounková, O. Čadek, F. Postberg, and O. Souček. Powering prolonged hydrothermal activity inside Enceladus. *Nature Astronomy*, pages 841–847, 2017. ISSN 2397-3366. doi:10.1038/s41550-017-0289-8.

M. Choukroun and C. Sotin. Is Titan's shape caused by its meteorology and carbon cycle? *Geophysical Research Letters*, 39(4), 2012.

G. Collins and J. Goodman. Enceladus' south polar sea. *Icarus*, pages 72–82, 2007. ISSN 0019-1035.

J. Cullum, D. P. Stevens, and M. M. Joshi. Importance of ocean salinity for climate and habitability. *Proceedings of the National Academy of Sciences of the United States of America*, 113(16):4278–4283, 2016. ISSN 10916490. doi:10.1073/pnas.1522034113.

D. Durante, D. Hemingway, P. Racioppa, L. Iess, and D. Stevenson. Titan's gravity field and interior structure after Cassini. *Icarus*, 326:123–132, Jul 2019. ISSN 0019-1035. doi:10.1016/j.icarus.2019.03.003.

R. Ferrari, M. F. Jansen, J. F. Adkins, A. Burke, A. L. Stewart, and A. F. Thompson. Antarctic sea ice control on ocean circulation in present and glacial climates. *Proceedings of the National Academy of Sciences*, 111(24): 8753–8758, 2014. ISSN 0027-8424. doi:10.1073/pnas.1323922111.

P. R. Gent and J. C. McWilliams. Isopycnal mixing in ocean circulation models. *Journal of Physical Oceanography*, pages 150–155, 1990.

C. Glein, F. Postberg, and S. Vance. *The Geochemistry of Enceladus: Composition and Controls*, pages 39–56. University of Arizona Press, 2019.

J. C. Goodman. Glacial flow of floating marine ice in "Snowball Earth". *Journal of Geophysical Research*, 108:1–12, 2003. ISSN 0148-0227. doi:10.1029/2002jc001471.

O. Grasset, M. Dougherty, A. Coustenis, E. Bunce, C. Erd, D. Titov, M. Blanc, A. Coates, P. Drossart, L. Fletcher, H. Hussmann, R. Jaumann, N. Krupp, J.-P. Lebreton, O. Prieto-Ballesteros, P. Tortora, F. Tosi, and T. V. Hoolst. JUpiter ICy moons Explorer (JUICE): An {ESA} mission to orbit Ganymede and to characterise the Jupiter system. *Planetary and Space Science*, 78(0):1 – 21, 2013. ISSN 0032-0633. doi:10.1016/j.pss.2012.12.002.

J. S. Green. Transfer properties of the large-scale eddies and the general circulation of the atmosphere. *Quarterly Journal of the Royal Meteorological Society*, 96:157–185, 1970.

S. Groeskamp, S. M. Griffies, D. Iudicone, R. Marsh, A. G. Nurser, and J. D. Zika. The water mass transformation framework for ocean physics and biogeochemistry. *Annual Review of Marine Science*, pages 271–305, 2019. ISSN 1941-1405. doi:10.1146/annurev-marine-010318-095421.

M. F. Jansen. The turbulent circulation of a snowball earth ocean. *Journal of Physical Oceanography*, 46(6):1917–1933, 2016. ISSN 15200485. doi:10.1175/JPO-D-15-0224.1.

E. L. Lewis and R. G. Perkin. Ice pumps and their rates. *Journal of Geophysical Research: Oceans*, pages 11756–11762, 1986. doi:10.1029/JC091iC10p11756.

J. Marshall and T. Radko. Residual-mean solutions for the antarctic circumpolar current and its associated overturning circulation. *Journal of Physical Oceanography*, 33(11):2341–2354, 2003. ISSN 0022-3670. doi:10.1175/1520-0485(2003)033<2341:RSFTAC>2.0.CO;2.

J. Marshall and K. Speer. Closure of the meridional overturning circulation through Southern Ocean upwelling. *Nature Geoscience*, 5(3):171–180, 2012. ISSN 1752-0908. doi:10.1038/ngeo1391.

W. B. McKinnon. Effect of Enceladus's rapid synchronous spin on interpretation of Cassini gravity. *Geophysical Research Letters*, 42(7):2137–2143, 2015.

H. J. Melosh, A. G. Ekholm, A. P. Showman, and R. D. Lorenz. The temperature of Europa's subsurface water ocean. *Icarus*, pages 498–502, 2004.

W. H. Munk. Abyssal recipes. *Deep Sea Research and Oceanographic Abstracts*, 13(4):707–730, aug 1966. ISSN 00117471. doi:10.1016/0011-7471(66)90602-4.

F. Postberg, S. Kempf, J. Schmidt, N. Brilliantov, A. Beinsen, B. Abel, U. Buck, and R. Srama. Sodium salts in E-ring ice grains from an ocean below the surface of Enceladus. *Nature*, 459(7250):1098–1101, 2009. ISSN 00280836. doi:10.1038/nature08046.

F. Postberg, N. Khawaja, B. Abel, G. Choblet, C. R. Glein, M. S. Gudipati, B. L. Henderson, H.-W. Hsu, S. Kempf, F. Klenner, and et al. Macromolecular organic compounds from the depths of Enceladus. *Nature*, 558(7711): 564–568, Jun 2018. ISSN 1476-4687. doi:10.1038/s41586-018-0246-4.

K. M. Soderlund. Ocean dynamics of outer solar system satellites. *Geophysical Research Letters*, 46(15):8700–8710, 2019. doi:10.1029/2018GL081880.

K. M. Soderlund, B. E. Schmidt, J. Wicht, and D. D. Blankenship. Ocean-driven heating of Europa's icy shell at low latitudes. *Nature Geoscience*, pages 16–19, 2014. ISSN 17520894. doi:10.1038/ngeo2021.

K. Speer, S. R. Rintoul, and B. Sloyan. The diabatic Deacon cell. *Journal of Physical Oceanography*, 30:3212–3222, 2000.

J. R. Spencer, J. C. Pearl, M. Segura, F. M. Flasar, A. Mamoutkine, P. Romani, B. J. Buratti, A. R. Hendrix, L. J. Spilker, and R. M. C. Lopes. Cassini encounters Enceladus: Background and the discovery of a south polar hot spot. *Science*, 311:1401 – 1405, 2006.

A. F. Thompson, S. K. Hines, and J. F. Adkins. A southern ocean mechanism for the interhemispheric coupling and phasing of the bipolar seesaw. *Journal of Climate*, pages 4347–4365, apr 2019. ISSN 0894-8755. doi:10.1175/JCLI-D-18-0621.1.

E. Turtle, J. Barnes, M. Trainer, R. Lorenz, K. Hibbard, D. Adams, P. Bedini, J. Langelaan, and K. Zacny. Dragonfly: In situ exploration of Titan's prebiotic organic chemistry and habitability. In *European Planetary Science Congress*, 2017.

T. Uchida, D. Balwada, R. P. Abernathey, G. A. McKinley, S. K. Smith, and M. Lévy. Vertical eddy iron fluxes support primary production in the open southern ocean. *Nature Communications*, 11:1125, 2020. ISSN 2041-1723. doi:10.1038/s41467-020-14955-0.

S. Vance and J. Goodman. Oceanography of an Ice-Covered Moon. In *Europa*, number August, pages 459–482. University of Arizona Press, 2009. doi:10.2307/j.ctt1xp3wdw.25.

S. D. Vance, M. P. Panning, S. Stähler, F. Cammarano, B. G. Bills, G. Tobie, S. Kamata, S. Kedar, C. Sotin, W. T. Pike, R. Lorenz, H. H. Huang, J. M. Jackson, and B. Banerdt. Geophysical Investigations of Habitability in Ice-Covered Ocean Worlds. *Journal of Geophysical Research: Planets*, 123(1): 180–205, 2018. ISSN 21699100. doi:10.1002/2017JE005341.

J. H. Waite, C. R. Glein, R. S. Perryman, B. D. Teolis, B. A. Magee, G. Miller, J. Grimes, M. E. Perry, K. E. Miller, A. Bouquet, et al. Cassini finds molecular hydrogen in the Enceladus plume: Evidence for hydrothermal processes. *Science*, 356(6334):155–159, 2017.

P. Zhu, G. E. Manucharyan, A. F. Thompson, J. C. Goodman, and S. D. Vance. The influence of meridional ice transport on Europa's ocean stratification and heat content. *Geophysical Research Letters*, pages 5969–5977, 2017. ISSN 19448007. doi:10.1002/2017GL072996.